



Universidade do Estado do Rio de Janeiro

Centro de Tecnologia e Ciências

Faculdade de Engenharia

Rachel Manhães de Lucena

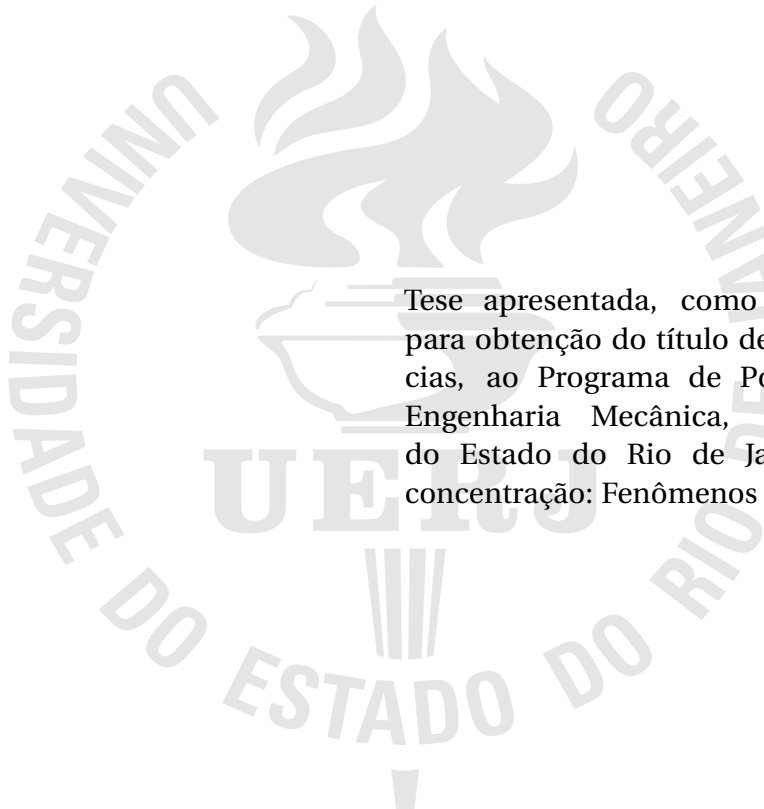
**Numerical study of CO₂ dissolution in saline aquifers with deformed
interface**

Rio de Janeiro

2016

Rachel Manhães de Lucena

Numerical study of CO₂ dissolution in saline aquifers with deformed interface



Tese apresentada, como requisito parcial para obtenção do título de Doutor em Ciências, ao Programa de Pós-Graduação em Engenharia Mecânica, da Universidade do Estado do Rio de Janeiro. Área de concentração: Fenômenos de Transporte.

Orientador: Prof. DSc. José da Rocha Miranda Pontes

Orientador: Prof. PhD. Norberto Mangiacchi

Rio de Janeiro

2016

CATALOGAÇÃO NA FONTE
UERJ / REDE SIRIUS / BIBLIOTECA CTC/B

L935	<p>Lucena, Rachel Manhães de. Numerical study of CO₂ dissolution in saline aquifers with deformed interface / Rachel Manhães de Lucena. – 2016. 135 f.</p> <p>Orientadores: José da Rocha Miranda Pontes e Norberto Mangiavacchi. Tese (Doutorado) – Universidade do Estado do Rio de Janeiro, Faculdade de Engenharia.</p> <p>1. Engenharia Mecânica – Teses. 2. Mecânica dos Fluidos – Teses. 3. Escoamento em Meios Porosos – Teses. 4. Método dos Elementos Finitos – Teses. I. Pontes, José da Rocha Miranda. II. Mangiavacchi, Norberto. III. Universidade do Estado do Rio de Janeiro. IV. Título.</p> <p style="text-align: right;">CDU 531.3</p>
------	--

Autorizo, apenas para fins acadêmicos e científicos, a reprodução total ou parcial desta dissertação, desde que citada a fonte.

Assinatura

Data

Rachel Manhães de Lucena

Numerical study of CO₂ dissolution in saline aquifers with deformed interface

Tese apresentada, como requisito parcial para obtenção do título de Doutor em Ciências, ao Programa de Pós-Graduação em Engenharia Mecânica, da Universidade do Estado do Rio de Janeiro. Área de concentração: Fenômenos de Transporte.

Aprovado em: 14 de dezembro de 2016

Banca Examinadora:

Prof. Ph.D. Norberto Mangiavacchi
Faculdade de Engenharia - UERJ

Prof. D.Sc. José da Rocha Miranda Pontes
Faculdade de Engenharia - UERJ

Prof. D.Sc. Gustavo Rabello dos Anjos
Faculdade de Engenharia - UERJ

Prof. D.Sc. Marcelo Amorim Savi
COPPE/UFRJ

Prof. D.Sc. Reinaldo Roberto Rosa
INPE

Rio de Janeiro

2016

DEDICATION

To Bruno, with love.

ACKNOWLEDGMENTS

Sem dúvida alguma este trabalho não existiria se não fosse o incentivo e o apoio de algumas pessoas especiais, aqui tento expressar um pouco da minha gratidão aos envolvidos.

Primeiramente, agradeço a minha família pelo apoio e confiança de sempre, em especial ao Bruno.

Certas vezes ouvi dizerem que sou uma pessoa de sorte, não sei dizer se é totalmente verdade ou inverdade, mas uma coisa posso dizer: sinto-me muito feliz em ter os Professores Pontes e Norberto como orientadores.

Agradeço ao Prof. Pontes pela confiança em mim e no meu trabalho, desde que ingressei no mestrado, com muita tranquilidade, discernimento e sabedoria sempre me orientou e ensinou de forma que levarei para toda minha vida.

Ao Prof. Norberto agradeço por todo incentivo e conhecimento dispensado para a realização deste trabalho, sua incansável disposição em solucionar problemas me faz despertar cada vez mais o interesse pela pesquisa.

Agradeço também a colaboração do Prof. Gustavo R. Anjos sempre disposto a me ajudar e a ser sempre um entusiasta deste trabalho.

J'adresse mes meilleurs remerciements au Professeur Anne De Wit, qui m'a très chaleureusement accueilli à l'Université Libre de Bruxelles, tout en contribuant pour le contenu de cette thèse et pour ma formation professionnelle.

Agradeço aos Professores Marcelo A. Savi e Reinaldo R. Rosa que aceitaram participar da avaliação deste trabalho, a qual rendeu excelentes ideias e propostas para trabalhos futuros.

Aos meus colegas de laboratório GESAR e dos cursos agradeço pelos momentos de estudos, discussões de ideias, conversas agradáveis e comemorações. Sem dúvidas, esses momentos são fundamentais para a formação pessoal e profissional.

Agradeço à Dona Sonia pelas agradáveis conversas, almoços, bolinhos e, principalmente, a amizade durante esse tempo.

À Coordenação de Aperfeiçoamento de Pessoal de Nível Superior (CAPES) e ao Conselho Nacional de Desenvolvimento Científico e Tecnológico (CNPq) pela bolsa de estudos de Doutorado no Brasil e para o doutorado Sanduíche, respectivamente.

The greater our knowledge increases the more our ignorance unfolds.

John F. Kennedy

RESUMO

LUCENA, Rachel Manhães de. *Estudo Numérico da dissolução do CO₂ em aquíferos salinos com interface deformada*. 135f. Tese (Doutorado em Engenharia Mecânica) - Faculdade de Engenharia, Universidade do Estado do Rio de Janeiro (UERJ), Rio de Janeiro, 2016.

Consideramos o problema de geração de *fingers* induzidos por flutuações de densidade do fluido que ocupa um meio poroso pela instabilidade de uma camada de fluido parcialmente miscível dissolvendo em uma camada fluido menos denso existente abaixo. O processo de *fingering* induz uma distribuição desigual de CO₂ dissolvido nas camadas superiores, o que afeta a distribuição da tensão superficial na interface, e desestabiliza a geometria de superfície plana. Assumimos uma interface curva para modelar os efeitos de tensão superficial. O principal objetivo é verificar se a superfície curva aumenta a taxa de dissolução CO₂ e avaliar uma curvatura que maximiza a dissolução do gás. São realizadas simulações numéricas bidimensionais e dependentes do tempo, assumindo que o fluxo é governado pela Lei de Darcy, juntamente com a aproximação de Boussinesq, para contabilizar os efeitos introduzidos pela flutuação de densidades dependente da concentração. Os resultados mostraram que a deformação da interface induz o início da formação dos *fingers*, entretanto o aumento dessa deformação diminui a quantidade de *fingers*. Tal como o fluxo de dissolução é influenciado pelas deformações idealizadas. O campo de velocidade é modelado por uma formulação vorticidade-função de corrente. As equações resultantes são resolvidos através de Taylor-Galerkin Método dos Elementos Finitos, utilizando o Método de Crank-Nicolson para a discretização temporal.

Palavras-chave: *fingering*; instabilidades hidrodinâmicas; escoamento em meios porosos; sequestro de gás carbônico; método dos elementos finitos.

ABSTRACT

LUCENA, Rachel Manhães de. *Numerical study of CO₂ dissolution in saline aquifers with deformed interface*. 135f. Tese (Doutorado em Engenharia Mecânica) - Faculdade de Engenharia, Universidade do Estado do Rio de Janeiro (UERJ), Rio de Janeiro, 2016.

We address the problem of buoyancy-driven fingering generated in porous media by the instability of a partially miscible fluid layer dissolving in a less dense fluid existing underneath. The fingering process induces an uneven distribution of dissolved CO₂ in the upper layers, which affects the surface tension distribution at the interface, and unstabilizes the geometry of the flat surface. We assume a curved interface to model surface tension effects. The main purpose is to check if the curved surface increases the CO₂ dissolution rate and to evaluate a curvature that maximizes the gas dissolution. A 2D time dependent numerical simulation is performed, assuming that the flow is governed by Darcy's law, along with the Boussinesq approximation, to account for buoyancy effects introduced by concentration dependent densities. The results show that the interface deformation induces the onset of fingering, however the number of fingers decreases as the deformation increases and the dissolution rate is influenced by the prescribed interface deformations. The velocity field is modeled by a vorticity-stream function formulation. The resulting equations are solved through the Taylor-Galerkin Finite Element Method, using a Crank-Nicolson time discretization.

Keywords: fingering; hydrodynamic instabilities; porous media flow; carbon sequestration; finite element method.

LIST OF FIGURES

Figure 1	Schematic representation of capture systems.....	24
Figure 2	Schematic diagram of possible CCS systems.....	26
Figure 3	Instability of front at the interface of CO ₂ and water.....	29
Figure 4	Sketch of porous domain, before and after upper interface deformation.....	40
Figure 5	Schematic of periodic lateral boundaries.....	41
Figure 6	Analytical solution of concentration.	42
Figure 7	Representation of the domain for the FEM.....	44
Figure 8	Representation of discretized domain	45
Figure 9	Sketch of triangular finite element.....	47
Figure 10	Triangular elements with local and global nodes.....	50
Figure 11	Example of mesh generation.	53
Figure 12	Mapping the space-time concentration.	57
Figure 13	Identification of y -coordinates of space-time maps.	58
Figure 14	Space-time maps identifying prescribed times of evolution.....	59
Figure 15	Dispersion curves of normal mode perturbations of the base state.	61
Figure 16	Two uniform meshes used in the in the experiments.	63
Figure 17	Comparison between relative error, distances Δx and Δx^2	64
Figure 18	A non-uniform grid with $N \times M = 150 \times 150$ points.	65
Figure 19	Evolution of the amplitude of Mode 4 for initial amplitudes.....	66
Figure 20	“Exact” and approximate rates of growth associated to different perturbations. 66	66
Figure 21	Comparison of concentration profiles at several times.....	67
Figure 22	Perturbation modes of ψ and associated mode profiles.....	68
Figure 23	Concentration profile of mode 3 and distribution at two times.	68
Figure 24	Amplitude of mode 3 for several amplitudes.....	69
Figure 25	Amplitude of mode 4 for several amplitudes.....	69
Figure 26	Rate of growth of mode 3 with random initial condition.	70
Figure 27	Rate of growth of mode 4 with random initial condition.	70
Figure 28	Comparison of concentration profiles with initial condition: mode 4.	71
Figure 29	Perturbation modes of ψ and associated mode profiles.....	72

Figure 30	Concentration profile of mode 4 and distribution at two times.	72
Figure 31	Amplitude of mode 4 for several amplitudes.	73
Figure 32	Rate of growth of mode 4 with the different initial amplitudes.	73
Figure 33	Evolution of the amplitude of mode 4 with frozen and no frozen base state. ..	74
Figure 34	Evolution of the rate of growth of mode 4 with frozen and no frozen base state.	74
Figure 35	Time evolution of the concentration with random initial condition.....	76
Figure 36	Long term evolution of mode 4 with random initial condition.	77
Figure 37	Time evolution of the concentration from the base state at $t = 252$ and mode 4.	78
Figure 38	Time evolution of the concentration from the base state at $t = 252$ and mode 4.	79
Figure 39	Long term evolution of mode 4 from the base state at $t = 252$ and mode 4.....	80
Figure 40	System state at $t = 1000$ of flat interface and errors.	81
Figure 41	System state at $t = 5000$ of flat interface and errors.	82
Figure 42	System state of flat interface in a small domain.	83
Figure 43	Average concentration profiles of flat interface in a small domain.	83
Figure 44	Evolution of the mixing length and area.	84
Figure 45	Space-time chart and position of the fingers.....	84
Figure 46	Average number of wavelengths.	84
Figure 47	Evolution of the mixing length of the tests with $\Delta x = 10.0$	86
Figure 48	Evolution of the mixing length of the tests with $\Delta x = 5.0$	87
Figure 49	Evolution of the mixing length of the tests with $\Delta x = 2.5$	88
Figure 50	Comparison between average mixing lengths,with values of Δx and Δt	88
Figure 51	Time evolution frames of flat interface - 1^{st} domain.....	89
Figure 52	Average concentration profiles of flat interface - 1^{st} domain.	90
Figure 53	Mixing length and finger area of flat interface - 1^{st} domain.	90
Figure 54	Space-time map and position of fingers of flat interface - 1^{st} domain.	90
Figure 55	Average wavelength of flat interface - 1^{st} domain.....	91
Figure 56	Time evolution frames of flat interface - 2^{nd} domain.	91
Figure 57	Average concentration profiles of flat interface - 2^{nd} domain.	92
Figure 58	Mixing length and finger area of flat interface - 2^{nd} domain.....	92
Figure 59	Space-time map and position of fingers of flat interface - 2^{nd} domain.	92
Figure 60	Average wavelength of flat interface - 2^{nd} domain.....	93
Figure 61	Time evolution frames of deformed interface - 1^{st} domain.....	94

Figure 62	Average concentration profiles of deformed interface - 1 st domain.	94
Figure 63	Mixing length and finger area of deformed interface - 1 st domain.	94
Figure 64	Space-time map and position of fingers of deformed interface - 1 st domain. .	95
Figure 65	Average of number of fingers of deformed interface - 1 st domain.	95
Figure 66	Time evolution frames of deformed interface - 2 nd domain.	96
Figure 67	Average concentration profiles of deformed interface - 2 nd domain.	96
Figure 68	Mixing length and finger area of deformed interface - 2 nd domain.	96
Figure 69	Space-time map and position of fingers of deformed interface - 2 nd domain.	97
Figure 70	Average of number of fingers of deformed interface - 2 nd domain.	97
Figure 71	Time evolution and space-time map of flat interface.	99
Figure 72	Time evolution and space-time map of deformed interface with $A = 300$	99
Figure 73	Time evolution and space-time map of deformed interface with $A = 600$	99
Figure 74	Time evolution and space-time map of deformed interface with $A = 900$	100
Figure 75	Time evolution and space-time map of deformed interface with $A = 1200$	100
Figure 76	Average longitudinal and transverse profiles for flat interface.	101
Figure 77	Average longitudinal and transverse profiles for $A = 300$	102
Figure 78	Average longitudinal and transverse profiles for $A = 600$	102
Figure 79	Average longitudinal and transverse profiles for $A = 900$	103
Figure 80	Average longitudinal and transverse profiles for $A = 1200$	103
Figure 81	Mixing length as a function of time.	104
Figure 82	Diffusive layer panel in the case with $A = 0$	105
Figure 83	Diffusive layer panel in the case with $A = 600$	105
Figure 84	Diffusive layer panel in the case with $A = 1200$	106
Figure 85	Area of the averaged transverse profile as a function of time.	106
Figure 86	Averaged number of fingers as function of time.	107
Figure 87	Relationship between average number of fingers and deformations.	108
Figure 88	Space-time maps of the evolution of five interfaces.	110
Figure 89	Time evolution of the average flux.	111
Figure 90	Sketch of domain with inclined surface.	121
Figure 91	Dispersion curves (real part) - Inclined surface.	124
Figure 92	Dispersion curves (imaginary part) - Inclined surface.	124
Figure 93	Dispersion curves (real part) obtained for several inclination angles.	125

Figure 94	Dispersion curves (imaginary part) obtained for several inclination angles....	125
Figure 95	Dispersion curves (real part) obtained for several inclination angles.	126
Figure 96	Dispersion curves (imaginary part) obtained for several inclination angles....	126
Figure 97	Time evolution of the case with $\theta = \pi/32$	127
Figure 98	Time evolution of the case with $\theta = \pi/16$	127
Figure 99	Time evolution of the case with $\theta = \pi/8$	127
Figure 100	Time evolution of the case with $\theta = \pi/6$	127
Figure 101	Space-time maps with $\theta = \pi/32$ and $\theta = \pi/16$	128
Figure 102	Space-time maps with $\theta = \pi/8$ and $\theta = \pi/6$	128

LIST OF TABLES

Table 1	Profile of worldwide large stationary CO ₂ sources.....	23
Table 2	Approximate rate of growth and associated error for 10 meshes.	63
Table 3	Effect of time steps and number of fingers - $\Delta x = 10$	85
Table 4	Effect of time steps and number of fingers - $\Delta x = 5.0$	86
Table 5	Effect of time steps and number of fingers - $\Delta x = 2.5$	87

LIST OF SYMBOLS

Acronyms

CCS Carbon dioxide Capture and Storage

FEM Finite Element Method

GHG Greenhouse Gases

LSA Linear Stability Analysis

Operators

∇ gradient operator

$\nabla \times$ curl operator

∇^2 laplacian operator

D^n differential operator

Symbols

ψ stream function

ω vorticity

ρ fluid specific mass

ρ_0 initial fluid specific mass

$\Delta\rho$ fluid specific mass variation

p pressure

p' initial pressure

μ fluid viscosity

g gravity constant

c mass concentration

c_{average}	average mass concentration
\mathcal{B}	Brinkman's pre-factor
\mathcal{B}_r	mass concentration
\mathcal{D}	diffusion coefficient
erf	error function
t	time
Δt	discrete time interval
Γ_i	part of boundary with $i = 1, \dots, 4$
Γ	boundary of domain
Ω	domain
\mathcal{A}	area of e -element
ξ	element natural coordinates for triangles
$\phi(\xi_1, \xi_2, \xi_3)$	area of e -element
det	determinant of matrix
\bar{c}	base state of concentration
\tilde{c}	perturbed base state of concentration
$\tilde{\psi}$	perturbed of stream function
k	wavenumber of the perturbation
σ	growth rate
a	amplitude of perturbation of initial condition
λ	wavelength associated to perturbations
ε_{rel}	relative error
$\langle c(x, t) \rangle$	average concentration longitudinal profile

$\langle c(y, t) \rangle$ average concentration transverse profile

L mixing length

$L_{\text{diffusive}}$ mixing length of diffusive regime

S area of the average concentration transverse profile

$\langle n \rangle$ average number of fingers

F dissolution flux

$\Delta y'$ distance from the upper interface

A amplitude of deformation of interface

t time

Δt discrete time interval

Vectors and Matrices

\mathbf{u} velocity vector field

\mathbf{g} gravity acceleration vector

\mathbf{n} normal vector

\mathbf{M} global mass matrix

\mathbf{D}_x matrix containing the gradient along the x -direction

$\mathbf{K}^e, \mathbf{M}^e$ stiffness and mass matrices of the e^{th} -element

\mathbf{K}, \mathbf{K}_c global stiffness matrices

Sets

\mathcal{V} space of functions v

\mathcal{H}^1 Hilbert space

\mathcal{L}^2 Lebesgue space

η set of node number

η_g set of number at conditions are specified

Various Integers

rand aleatory number (random)

e finite element

n_{eq} number of equations to solve

a, b local nodes numbers

A, b global nodes numbers

n_{el} number of elements

n_{np} number of nodal points

CONTENTS

	INTRODUCTION	19
1	BIBLIOGRAPHIC REVIEW	22
2	MATHEMATICAL MODEL	32
2.1	The vorticity equation	32
2.2	The vorticity transport equation	33
2.2.1	Boussinesq approximation	33
2.2.2	Parabolic velocity profile	34
2.2.3	Reduction of the problem dimensionality.....	35
2.2.4	Brinkman number approach	36
2.2.5	Non-dimensionalization process	36
2.2.6	Vorticity-stream function approach	38
2.3	Concentration equation	39
2.4	Boundary conditions	39
2.4.1	Initial condition	41
2.5	Analytical solution	41
3	METHODOLOGY	43
3.1	The Finite Element Method (FEM)	43
3.1.1	The Variational or Weak Formulation	43
3.1.2	The Galerkin Formulation	45
3.1.3	Triangular element and natural coordinates	46
3.1.4	Global stiffness and mass matrices	49
3.1.5	Assembly of the global stiffness and mass matrices	49
3.1.6	Element stiffness and mass matrices	51
3.2	Mesh definition.....	53
3.3	The Crank-Nicolson Method	54
3.4	Computational implementation of the numerical method	54
3.5	Characterization of the fingering structure.....	55

4	LINEAR STABILITY ANALYSIS ON A FLAT INTERFACE	60
4.1	Code validation – perturbation growth with frozen base state	61
4.1.1	Mesh spacing	62
4.1.2	The rate of growth of perturbations with frozen base state	64
4.2	Deployment of instabilities with variable base state	67
4.2.1	Random initial conditions	67
4.2.2	Initial condition: mode 4.....	70
4.3	The nonlinear regime	75
4.3.1	Random initial condition	76
4.3.2	Initial condition: mode 4.....	77
5	CODE VERIFICATION AND GRID CONVERGENCE	81
5.1	Code verification	81
5.2	Results with flat interface	82
5.3	Grid convergence	85
5.4	Choosing the integration domain.....	89
5.4.1	Flat interface	89
5.4.2	Deformed interface	93
6	NUMERICAL RESULTS	98
	CONCLUSIONS AND FUTURE WORKS	112
	REFERENCES	114
	APPENDIX A - ANALYTICAL SOLUTIONS	118
	APPENDIX B - LINEAR STABILITY AND NONLINEAR SIMULATION ON IN- CLINED INTERFACE	120
	APPENDIX C - CCIS 2016	129
	APPENDIX D - CCIS 2014	131

INTRODUCTION

Motivation

Carbon dioxide (CO₂) capture and geological storage is an enabling technology proposed to mitigate consequences of the continued use of fossil fuels, well into this century [1]. The main relevance for the geological storage of CO₂ is reducing anthropogenic emissions into the atmosphere. Currently we know that the power and industry sectors combined dominate current global CO₂ emissions, accounting for about 60% of total CO₂ emissions [2] [3].

Storage of carbon dioxide into deep saline aquifers has shown to be highly effective and has been addressed by many researchers ([4], [2], [5], [6], [7], [8]). When CO₂ is injected into the brine, the transport of the dissolved gas can occur by diffusion, advection, and convection, depending on the stage of sequestration process and geophysical properties of aquifer [9], [10].

The dissolution process results in a density gradient pointing upwards, that triggers a buoyancy-driven instability which, in turn, leads to a convective motion of the aquifer, and to the onset of a structure of fingers [11]. Experimentally, CO₂ dissolution process has been performed by a model developed in a very small thickness Hele-Shaw cell to reproduce a two-dimensional experiment [12], [13], [12], [14].

Justification

The present work is a numerical study and leads to a better evaluation of the carbon dioxide dissolution rate in the brine and in a classification of the associated phenomena related to the development of a structure of fingers.

The onset of the fingering structure induces an uneven distribution of dissolved CO₂ in the upper layers of the aquifer, which affects the surface tension distribution at the interface, and unstabilizes the geometry of the flat surface. The emerging deformed interface affects the fingering process, and may enhance CO₂ sequestration.

Nevertheless, most of the existing studies consider a flat interface, neglecting deformations resulting of the nonuniform distribution of the surface tension.

Main proposal

The present study addresses the effect of the curvature of the CO₂/brine interface on the onset and development of a structure of fingers, and how is the rate of gas dissolution affected by the enhanced aquifer motion induced by the interface curvature. The main motivation is to check if the curved surface increases the dissolution rate and evaluate an undulation amplitude that maximizes CO₂ dissolution.

Methodology

A 2D time dependent numerical simulation is performed, assuming that the flow is governed by Darcy's law, along with the Boussinesq approximation, to account for buoyancy effects introduced by concentration dependent densities. The velocity field is modeled by a vorticity-stream function formulation. The resulting equations are solved through the Taylor-Galerkin Finite Element Method, using a Crank-Nicolson time discretization.

Organization of this thesis

This thesis is organized in six chapters as described below:

1. **Chapter 1 - Bibliographic Review:** This chapter comprises the motivation of the work and review of the existing literature on the subject.
2. **Chapter 2 - Mathematical Model:** We present the assumed hypothesis and we derive the mathematical equations that model the proposed problem.
3. **Chapter 3 - Methodology:** We discuss the methodologies followed to solve the model equations, namely, the Finite Element Method for solving the linear systems of equations and the post-processing procedure for characterization of the emerging fingering structure.
4. **Chapter 4 - Linear Stability Analysis on a Flat Interface:** In this chapter, we performed the linear stability analysis of the problem assuming flat interface in order to validate the numerical schemes.
5. **Chapter 5 - Code Verification and Grid Convergence:** We present the procedures adopted for verification of the main numerical code written in the C language.

6. **Chapter 6 - Numerical Results:** The results obtained with the procedures described in Chapter 3 are presented and discussed in this chapter.

The thesis comprises a conclusive chapter where we suggest future works on the problem and also four appendices complementing the work.

1 BIBLIOGRAPHIC REVIEW

Notably, and regrettably, several indicators currently point to an increase in the Earth's temperature. Since the beginning of industrial age, an average increase of 0.6°C and an increase of 10cm to 20cm in the sea level has been recorded. Nowadays, we are suffering the first negative effects: disorganized climate, floods, heat waves, droughts, melting glaciers, rising sea levels, changes in flora and fauna. The experts on the planet identify the gases called Greenhouse Gases (GHG), mainly the carbon gas or carbon dioxide (CO_2), which generates about 55% of the anthropogenic greenhouse effect, as the responsible for these climate changes. Produced in large quantities by human activities (transport, habitat and industry), GHG escape mainly during the combustion of fossil fuels (coal, oil or gas). In a century, concentrations of these gases in the atmosphere increased by 50% and that of CO_2 by 31% [3, 15].

Surely, the amount of carbon dioxide emitted by humans are a small part of the total annual carbon cycle, but the natural carbon sinks in the biosphere and the oceans absorb only half of them. The surplus accumulates year after year in the Earth's atmosphere by disrupting the delicate mechanisms of the climate. If nothing is done or not enough to reduce CO_2 emissions and better manage consumption of fossil fuels, experts predict for 2100 an average temperature increase of 2 to 6°C and an increase of 9 to 88cm of sea level, with all the negative consequences thereof [3]. The current rate of anthropogenic emissions of CO_2 demand technological solutions on a large scale [7].

Unfortunately, most scenarios project that the supply of primary energy will continue to be dominated by fossil fuels until at least the middle of the century [16]. But, most models also indicate that known technological options¹ could achieve a broad range of atmospheric stabilization levels but that implementation would require socio-economic and institutional changes. In this context, the availability of carbon dioxide capture and storage (CCS) in the portfolio of options could facilitate achieving stabilization goals [7].

Despite the wide range alternatives measures proposed for combating the greenhouse effect (energy savings, clean transportation, renewable energy sources, nuclear power, among others), the feature of carbon dioxide capture and storage is an indispensable supplementary measure to limit the global warming. CCS is a process consisting of the separation of CO_2

¹"Known technological options" refer to technologies that exist in operation or in the pilot plant stage at the present time.

from industrial and energy-related sources, transport to a storage location and long-term isolation from the atmosphere [2, 3]. CCS has the potential to reduce overall mitigation costs and increase flexibility in achieving greenhouse gas emission reductions.

As its name suggests, this technique offers capture and storage of CO₂. The capture can be applied to large point sources. The large point sources of CO₂ include large fossil fuel or biomass energy facilities, major CO₂-emitting industries, natural gas production, synthetic fuel plants and fossil fuel-based hydrogen production plants (see Table 1) [2].

Table 1: Profile of worldwide large stationary CO₂ sources with emissions of more than 0.1 million tonnes of CO₂ (MtCO₂) per year [2].

Process	Number of sources	Emissions (MtCO ₂ yr ⁻¹)
Fossil fuels		
Power	4,942	10,539
Cement production	1,175	932
Refineries	638	798
Iron and steel industry	269	646
Petrochemical industry	470	379
Oil and gas processing	Not available	50
Other sources	90	33
Biomass		
Bioethanol and bioenergy	303	91
Total	7,887	13,466

Within the technical storage methods, we can indicate: geological storage (in geological formations, such as oil and gas fields, unminable coal beds and deep saline formations), which constitute the largest potential storage volumes, ocean storage (direct release into the ocean water column or onto the deep seafloor) and industrial fixation of CO₂ into inorganic carbonates [2, 5]. Among proposed CCS options, geological formations such as oil and gas reservoirs and deep saline aquifers appear to be the most promising [17].

Table 1 shows the main concentrated sources of pollution and for this cases there are directly interested in the capture of carbon dioxide. The main difficulty is to distinguish it from other constituents (for examples: water vapour and nitrogen). The techniques used today are relatively expensive. There are different types of CO₂ capture systems: capture from

industrial process streams, post-combustion, pre-combustion and oxyfuel combustion, as shown in Figure 1. Some factors are important in the selection the capture system, such as: concentration of CO₂, in the gas stream, the pressure of the gas and the fuel type (solid or gas) [2,3].

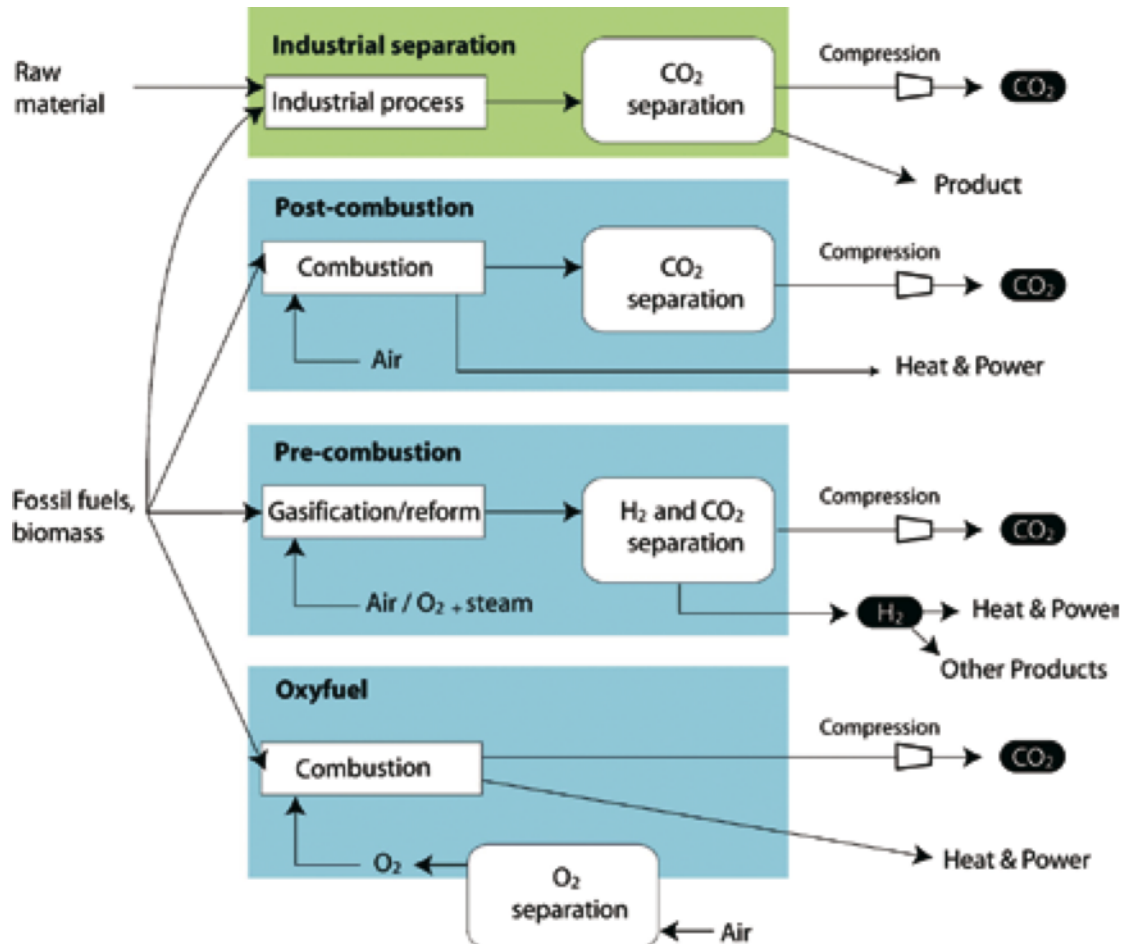


Figure 1: Schematic representation of capture systems. Fuels and products are indicated for oxyfuel combustion, pre-combustion, post-combustion and industrial sources of CO₂ [2].

CO₂ has been captured from industrial process streams for 80 years, although most of the CO₂ that is captured is vented to the atmosphere due to lack of incentive or legal requirement to store it. Current examples of CO₂ capture from process streams are purification of natural gas and production of hydrogen-containing synthesis gas for the manufacture of ammonia, alcohols and synthetic liquid fuels. Most of the techniques employed for CO₂ capture in the examples mentioned are also similar to those used in pre-combustion capture. Other industrial process streams which are a source of CO₂ that is not captured include cement and steel production, and fermentation processes for food and drink production [2].

Post-combustion systems separate CO₂ from the flue gases produced by the combus-

tion of the primary fuel in air. Instead of being discharged directly to the atmosphere, flue gas is passed through equipment which separates most of the CO₂. These systems normally use a liquid solvent to capture the small fraction of CO₂ (typically 3–15% by volume) present in a flue gas stream in which the main constituent is nitrogen (from air) [2, 3].

Pre-combustion systems process the primary fuel in a reactor with steam and air or oxygen to produce a mixture consisting mainly of carbon monoxide and hydrogen (“synthesis gas”). Additional hydrogen, together with CO₂, is produced by reacting the carbon monoxide with steam in a second reactor. The resulting mixture of hydrogen and CO₂ can then be separated into a CO₂ gas stream, and a stream of hydrogen. CO₂ is then separated, usually by a physical or chemical absorption process, resulting in a hydrogen-rich fuel which can be used in many applications, such as boilers, furnaces, gas turbines, engines and fuel cells [2, 3].

Although the initial fuel conversion steps are more elaborated and costly than in post combustion systems, the high concentrations of CO₂ produced by the shift reactor (typically 15 to 60% by volume on a dry basis) and the high pressures often encountered in these applications are more favourable for CO₂ separation [2].

Oxyfuel combustion systems use oxygen instead of air for combustion of the primary fuel to produce a flue gas that is mainly water vapour and CO₂, resulting in a flue gas with high CO₂ concentrations (greater than 80% by volume). The water vapour is then removed by cooling and compressing the gas stream. Oxyfuel combustion requires the upstream separation of oxygen from air, with a purity of 95–99% oxygen assumed in most current designs. Further treatment of the flue gas may be needed to remove air pollutants and noncondensed gases (such as nitrogen) from the flue gas before the CO₂ is sent to storage. The power plant systems of reference for oxyfuel combustion capture systems are the same as those noted for post-combustion capture systems [2,3].

After capture, the CO₂ would then be compressed and transported for storage in geological formations, in the ocean, in mineral carbonates, or for use in industrial processes for long durations that can cover several centuries, and this in any case security (see Figure 2) [2,3]. The options envisaged for geological storage are:

- storage in deep aquifers, the first channel in terms of capacity and geographical distribution; Experts estimate storage capacity in aquifers at several thousand billion tons;
- storage in depleted oil and gas deposits, an option all the more interesting as CO₂

injection can help to better recover additional oil;

- storage in the deposit coal seams not yet exploited, the injection may be accompanied by the production of methane (natural gas) commercially valuable;
- storage in basic rocks (basalts, peridotites, etc) ensuring at the same time the mineralization of CO₂ by carbonation of silicates.

Although the ocean storage removes the injected CO₂ from the atmosphere for several hundred years, this option has been abandoned due to the great uncertainties both on the long-term impact of an increase in CO₂ on the marine ecosystem and also on the residence time of CO₂ in the ocean [1,3].

Carbon dioxide must be directed after capture to the storage site. There are several techniques to transport it. However, volume data such as solutions based on a large scale only involve the use of pipelines and ships (see Figure 2) [3].

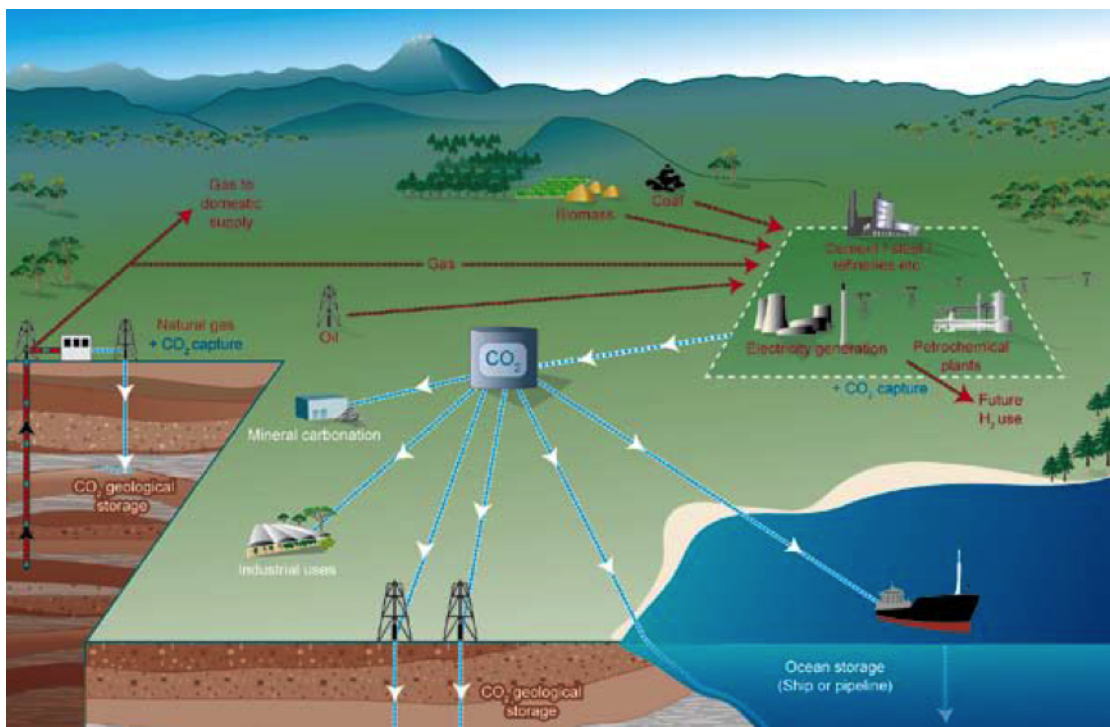


Figure 2: Schematic diagram of possible CCS systems showing the sources for which CCS might be relevant, transport of CO₂ and storage options [2].

Bachu [1] suggests that although various climate change mitigation options have different spatial and temporal ranges of applicability, the reduction of anthropogenic CO₂ emissions into the atmosphere can be achieved only through the broad and deep application, in developed and developing countries alike, of a portfolio of measures that includes

significant technological breakthroughs to increase energy efficiency, increasing as much as possible the share of non-fossil forms of energy production, and increasing the size and intake rate of CO₂ sinks, particularly carbon capture and storage in geological media [4–6].

In geological formations, carbon dioxide can be trapped by three mechanisms [18]:

1. trapped as a residual phase, commonly referred to as residual phase trapping;
2. dissolved into the formations brine, a process known as solubility trapping;
3. dissolved and dissociated into ionic species and react with minerals in the geologic formation, leading to the precipitation of secondary carbonate minerals, also called mineral trapping.

Solubility trapping has been studied in last years ([1, 9, 10, 19–23]) and has shown that the interface separating the supercritical free phase CO₂ and brine is destabilised by dissolving CO₂ into the brine. In fact, the dissolution of CO₂ increases the density of the liquid, resulting in a gravity inversion and instability. The primary benefit of solubility trapping is that once CO₂ is dissolved, it no longer exists as a separate phase, thereby eliminating the buoyant forces that drive it upwards. Subsequently, it will form ionic species as the rock dissolves, accompanied by a rise in the pH. Finally, some fraction may be converted to stable carbonate minerals (mineral trapping), the most permanent form of geological storage reducing the risk of CO₂ return to the atmosphere over the long-term [2, 18].

There are many works involving the study of carbon sequestration, we can mention: [7, 8, 10, 18, 21–28], however, some of these authors use in their study different mechanisms of trapping. Motivated by the CCS, Neufeld and Huppert [24] presented a theoretical-numerical study the propagation of gravity currents in a porous medium bounded by a thin layer of much lower permeability, which provides the basis for addressing the role of viscosity differences between CO₂ and the ambient fluid, residual trapping of the injected CO₂ and flow in tilted formations on the propagation of injected CO₂ through layered strata.

On the other hand, Pau *et al.* [25] performed high-resolution simulations to accurately characterize the dissolution-diffusion-convection process and concluded that although details of the convection process are chaotic in nature, the onset time of convection, and the long-term CO₂ mass flux associated with the convective activity, are robust and insensitive to modest problem variations. They also concluded that, at long time, the CO₂ mass flux reaches a stabilized state that approaches a constant value at space time scales of interest for

geological storage of CO₂, in particular, the long-term behavior is convection-dominated and depends only on the mean value of the permeability.

Dissolution and transport of CO₂ during geological storage occur through different transport mechanisms, including diffusion, dispersion, advection, and natural convection. Regardless of the transportation mode, the dissolution process is favourable since it mitigates the risk of leakage from the storage formation to shallower formations. This is because brine dissolved with CO₂ is slightly denser than ambient formation brine, resulting in CO₂ sinking rather than rising through a leakage pathway [10]. It is an important remark that the dissolution trapping occurs when CO₂ dissolves into the brine under ambient temperature and pressure conditions in a typical aquifer [25].

In this work, we focus on the carbon dioxide sequestration in deep saline formations with solubility trapping approach. CO₂ storage in deep saline aquifers is a mature technology that can be applied immediately. These formations are believed to have by far the largest capacity for CO₂ storage and are much more widespread than other options. While there are uncertainties, the global capacity to store CO₂ deep underground is large. Depleted oil and gas reservoirs are estimated to have a storage capacity of 675–900GtCO₂. Deep saline formations are very likely to have a storage capacity of at least 1000GtCO₂ and some studies suggest it may be an order of magnitude greater than this, but quantification of the upper range is difficult until additional studies are undertaken [1,2].

When the CO₂ is injected in a saline aquifer, it is essential that trapping be permanent to minimize the risk of leakage into shallower formations. Leakage is a primary concern because the plume of injected CO₂ is buoyant relative to the ambient groundwater at representative aquifer conditions, and will rise toward the top of the aquifer after injection and spread laterally as a buoyant gravity current [29].

One mechanism that acts to trap the buoyant CO₂ is the dissolution of free-phase CO₂ into the groundwater. Dissolved CO₂ is securely stored within the subsurface because it is no longer buoyant: the density of water increases with dissolved CO₂ concentration, so groundwater containing dissolved CO₂ will sink toward the bottom of the aquifer. As this mixture sinks in dense, CO₂-rich fingers, the resulting convective flow sweeps fresh groundwater upward. This convective dissolution process greatly enhances the rate at which the CO₂ dissolves into the groundwater [29]. The dissolution process results in a density gradient pointing upwards, that triggers a buoyancy-driven instability which, in turn, leads to

a convective motion of the aquifer, and to the onset of a structure of fingers (see Figure 3), which plays a crucial role in the CCS projects in aquifers due to its direct effects on increasing CO_2 dissolution rate [13].

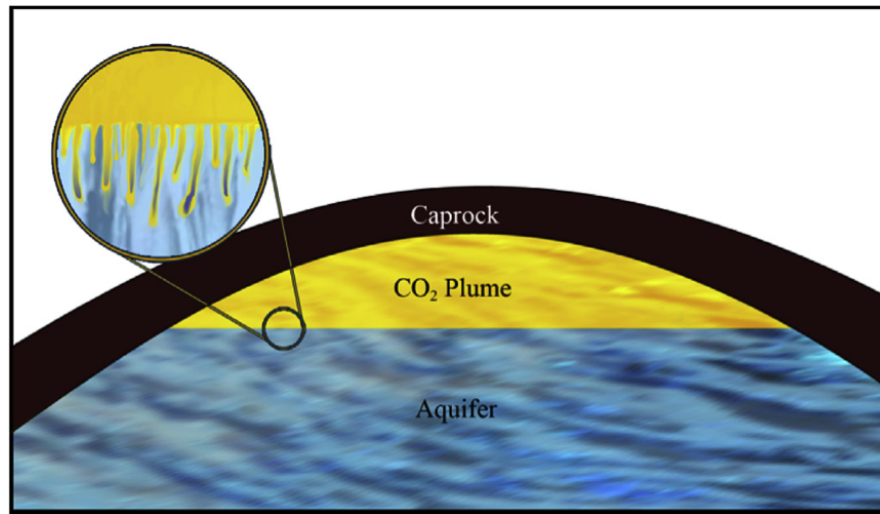


Figure 3: Instability of front at the interface of CO_2 and water causes natural mixing in the aquifer [13].

Fingering refers to hydrodynamic instabilities of deforming interfaces into fingers during the displacement of fluids in porous media. These instabilities are closely linked to changes in viscosity or density between the different layers or within a single phase containing a solute invariable concentration that affects the fluid density or viscosity [11].

Fingering occurs in a wide variety of applications, including secondary and tertiary oil recovery, fixed bed regeneration in chemical processing, hydrology, and filtration. Indeed, the phenomena are expected to occur in many of the myriad of fields of science and technology in which fluids flow through porous materials, and thus the literature is a diverse one [11]. We stress that our focus is in geologic carbon dioxide sequestration which involves injecting CO_2 into saline aquifers.

The onset of the fingering structure induces an uneven distribution of dissolved CO_2 in the upper layers of the aquifer, which affects the surface tension distribution at the interface, and unstabilizes the geometry of the at surface. The emerging deformed interface affects the fingering process, and may enhance CO_2 sequestration. Nevertheless, most of the existing studies consider a flat interface, neglecting deformations resulting of the nonuniform distribution of the surface tension.

The present study addresses the effect of the curvature of the CO_2 /brine interface on the onset and development of a structure of fingers, and how is the rate of gas dissolution

affected by the enhanced aquifer motion induced by the interface curvature. The main motivation is to check if the curved surface increases the dissolution rate and evaluate an undulation amplitude that maximizes CO₂ dissolution.

Linear stability analysis (LSA) is a widely used technique in which one finds numerically the earliest time at which linearized perturbations to the basic profile begin to grow. The first drawback of LSA is that due to linearization, the magnitude of the disturbance at later times is always proportional to the initial perturbation, so there is no natural criterion for when instability occurs. The second drawback of LSA is that the evolution of the perturbation depends on the Fourier spectrum of the initial disturbance [30].

Due to the importance of this technique, there are many works that perform the LSA with the convective dissolution of the carbon dioxide, it being the main subject of this analysis [20, 22, 25, 30–33]. In this work we also perform a linear stability analysis with the flat and deformed interface (the latter only presents preliminary results). LSA supports us to validate the results in the validation of the numerical code.

Experimental study of the CO₂ dissolution process has been done by a model developed in a vertically-oriented Hele-Shaw cell, to reproduce a two-dimensional experiment. The experiment is performed in a transparent Hele-Shaw cell containing brine overlain by CO₂ gas is presented. In the Hele-Shaw cell fluid flows in the narrow space between two parallel plates in a manner that is mathematically analogous (Darcy's law) to flow in porous media. This experiment provides visual observations of convective instabilities that would be useful in conceptual understanding of the effects density-driven convection on enhancing the mass transfer rate of CO₂ in brine [13]. Few studies have attempted to measure convective mixing quantities such as widths, lengths, and wavelengths of convective fingers, the timescale of the finger advancement, dissolution flux, average concentration, and horizontally averaged concentration profiles from experiments conducted in Hele-Shaw cells [10], we can cite: [12–14, 28, 34].

Slim [8] presents a summary of the distinct regimes of the rich dynamics of the convective dissolution based in some authors mentioned previously, as follow:

1. Initially, there is a *diffusive regime* in which the concentration profile is close to a onedimensional diffusive error function. The flux decays proportionally $1/\sqrt{t}$.
2. Eventually, sufficient dense fluid accumulates beneath the upper boundary for perturbations to amplify in a *linear-growth regime*.

3. Once convective fingers are macroscopic, they accelerate downwards with little lateral motion, stripping dense fluid from the interface and sharpening the concentration gradient at the upper boundary. This augments the dissolution flux, causing it to deviate from $t = 1/\sqrt{t}$ decay and grow to a local maximum, in a *flux-growth regime*.
4. Once fingers are sufficiently long, they begin interacting with their neighbors in a *merging regime*. Pairs of fingers zip together from the root downwards and stunted fingers retreat. Several generations of such coarsening occur to form complex downwelling plumes.
5. As a result of this coarsening, the upper horizontal boundary layer between the remaining primary plumes becomes sufficiently thick to be unstable. New plumes form, only to be swept back into and be subsumed by the primary plumes. In the Hele-Shaw cell experimental study of Slim *et al.* [35], this was hypothesized to be a separate *reinitiation regime*. During it, mergers had ceased.
6. Finally plumes impact the lower boundary and the entire layer progressively saturates with dissolved solute in a vertical size-dependent shut-down regime. The horizontally averaged concentration field has a vertically well-mixed bulk with a gradually expanding upper horizontal boundary layer.

According to Slim [8] in diffusive regime, the dissolution flux rate decays as $F(t) = 1/\sqrt{\pi t}$ and in the flux-growth regime, the key characteristic is that the flux is statistically constant throughout $F = 0.017$ (nondimensional). In our work we performed and analyze the simulations into the six regimes mentioned previously.

Hewitt *et al.* [27] performed simulations in miscible system. They proposed to relax the flat-interface assumption, thus, the interface is free to 'deform', and solute can be entrained across it. The extent of the deformation decreases with increasing of concentration in the upper boundary. The dominant wavelength of the deformed interface appears to be set by the lateral spacing of the descending megaplumes. The results suggest that the total solute flux $F(t)$ is initially much greater than with a flat interface, i.e., interfacial deformation can dramatically enhance the convective flux.

In this work, we calculate and analyze the dissolution flux across the upper interface, assuming both flat and deformed surfaces. Our analysis comprised the evolution of concentration profiles and mixing length, among others.

2 MATHEMATICAL MODEL

We address the problem of the onset and development of fingers, originated by the instability of the upper layers of a fluid media placed in a porous media. Over this first fluid layer, another one is placed, of a fluid with higher density than the density of the lower one. In addition of being denser than the underneath fluid, the upper one is assumed to be partially soluble in the lower fluid. Dissolution a single chemical species of the denser fluid, placed over the one filling the porous media, leads to a buoyancy instability at the top of this layer, and to the onset of a convective motion that can affect the rate of dissolution of the upper fluid.

We perform a time dependent numerical two-dimensional simulation of the instability of a denser layer on the top of the fluid occupying the porous media. The simulations are performed on rectangular domains, with the horizontal and vertical coordinate axes denoted, respectively, by x and y , and the vertical axis oriented downwards (see Figure 4). Accordingly, the gravitational acceleration is oriented on the opposite sense of the y axis.

The convective motion is assumed to obey Darcy's law, with the Boussinesq approximation to capture the instability induced by the concentration dependent density of the fluid filling the porous media. The fluid viscosity is assumed to be constant, and we choose a vorticity-stream function formulation to represent the system hydrodynamics, among the existing formulations for solving the Navier-Stokes equations, to which the hydrodynamic field obeys [14]. By so doing we eliminate the variable pressure, reducing thus, the number of variables and of equations to be solved in each element.

2.1 The vorticity equation

We consider a incompressible two-dimensional flow with flow velocity \mathbf{u} . The stream function satisfies the equations:

$$\mathbf{u} = \mathbf{u}(u, v) \quad \text{where} \quad u = \frac{\partial \psi}{\partial y} \quad \text{and} \quad v = -\frac{\partial \psi}{\partial x}, \quad (2.1)$$

where ψ represents the stream function. The flow vorticity is equal to the curl of velocity field, namely:

$$\boldsymbol{\omega} = \nabla \times \mathbf{u}. \quad (2.2)$$

By replacing the components of the velocity vector, expressed in terms of the stream function we obtain the following equation for the flow vorticity:

$$\frac{\partial^2 \psi}{\partial y^2} + \frac{\partial^2 \psi}{\partial x^2} = -\omega_z.$$

The flow vorticity, along with the stream function formulation, is given, thus, by:

$$\nabla^2 \psi = -\omega_z, \quad (2.3)$$

where $\nabla^2 \psi$ stands for the laplacian of ψ .

2.2 The vorticity transport equation

This section describes the steps accomplished for derivation of the non dimensional vorticity transport equation, assuming the Boussinesq approximation, a parabolic velocity profile in a two-dimensional Hele-Shaw cell, along with the Brinkman correction.

2.2.1 Boussinesq approximation

The first step of the procedure towards the derivation of the governing vorticity-stream function equations of the problem consists in introducing the constitutive equation for the specific mass and an expression for the perturbed pressure in the Navier-Stokes equations [36].

The Navier-Stokes read, in vector form:

$$\rho \frac{D\mathbf{u}}{Dt} = -\nabla p + \mu \nabla^2 \mathbf{u} + \rho \mathbf{g},$$

where \mathbf{u} is the velocity vector, p stems for the pressure, ρ , for the fluid specific mass, μ , for the

fluid viscosity and \mathbf{g} , for the gravity acceleration:

$$\begin{aligned}\rho &= \rho_0 + \Delta\rho \\ p &= p' - \rho_0 g y \\ \mathbf{g} &= -g \nabla y,\end{aligned}$$

with ρ_0 and g constants.

Developing the terms of the Navier-Stokes equation:

$$\begin{aligned}\rho \frac{D\mathbf{u}}{Dt} &= -\nabla(p' - \rho_0 g y) + \mu \nabla^2 \mathbf{u} - \rho g \nabla y; \\ \rho \frac{D\mathbf{u}}{Dt} &= -\nabla p' + \rho_0 g \nabla y - \rho g \nabla y + \mu \nabla^2 \mathbf{u}; \\ \rho \frac{D\mathbf{u}}{Dt} &= -\nabla p' - (\rho - \rho_0) g \nabla y + \mu \nabla^2 \mathbf{u}; \\ \rho \frac{D\mathbf{u}}{Dt} &= -\nabla p' - \Delta\rho g \nabla y + \mu \nabla^2 \mathbf{u},\end{aligned}$$

where ∇y defines the direction of \mathbf{g} . Assuming $\Delta\rho = \rho_0 \beta c$, where c is the mass concentration and β is an arbitrary constant, we have:

$$\rho \frac{D\mathbf{u}}{Dt} = -\nabla p' + \mu \nabla^2 \mathbf{u} + \rho_0 \beta c \mathbf{g}. \quad (2.4)$$

The Boussinesq approximation neglects specific mass variations in the inertia terms ($\rho = \rho_0$), so we have:

$$\rho_0 \frac{D\mathbf{u}}{Dt} = -\nabla p' + \mu \nabla^2 \mathbf{u} + \rho_0 \beta c \mathbf{g}.$$

Finally, we assume that the fluid acceleration is small, namely, $(D\mathbf{u}/Dt \approx 0)$, what leads to:

$$\nabla p' = \mu \nabla^2 \mathbf{u} + \rho_0 \beta c \mathbf{g}. \quad (2.5)$$

2.2.2 Parabolic velocity profile

This step consists in evaluating the parabolic velocity profile in the Hele-Shaw cell [37].

We assume that the fluid velocity is given by:

$$\mathbf{u} = z(\delta - z)\mathbf{k},$$

where δ is the distance between the parallel plates of the cell. The average velocity is given by:

$$\bar{\mathbf{u}} = \frac{1}{\delta} \mathbf{k} \int_0^\delta z(\delta - z) dz,$$

what leads to:

$$k = \frac{\delta \bar{\mathbf{u}}}{\int_0^\delta z(\delta - z) dz} \implies k = \frac{6\bar{\mathbf{u}}}{\delta^2}.$$

By replacing k in the velocity equation we obtain the derivative in the z direction:

$$\mathbf{u} = \frac{6\bar{\mathbf{u}}}{\delta^2} z(\delta - z) \implies \left. \frac{\partial \mathbf{u}}{\partial z} \right|_{z=0} = \frac{6\bar{\mathbf{u}}}{\delta^2} (\delta - 2z) \Big|_{z=0} = \frac{6\bar{\mathbf{u}}}{\delta}.$$

So, we can also write:

$$\frac{\partial \mathbf{u}}{\partial z} = \frac{6\bar{\mathbf{u}}}{\delta}. \quad (2.6)$$

2.2.3 Reduction of the problem dimensionality

In this step we eliminate one of the spatial directions, reducing the original problem in dimensionless form, governed by Eq. 2.5, to a two-dimensional one.

Assuming that the average velocity, the pressure and the concentration are given by:

$$\bar{\mathbf{u}} = \frac{1}{\delta} \int_0^\delta \mathbf{u} dz; \quad \bar{p} = \frac{1}{\delta} \int_0^\delta p dz; \quad \bar{c} = \frac{1}{\delta} \int_0^\delta c dz, \quad (2.7)$$

and integrating Eq. 2.5 along the z direction, we obtain

$$\frac{1}{\delta} \int_0^\delta \frac{\partial p}{\partial x} dz = \frac{1}{\delta} \int_0^\delta \mu \frac{\partial^2 \mathbf{u}}{\partial z^2} dz + \frac{1}{\delta} \int_0^\delta \mu \left(\frac{\partial^2 \mathbf{u}}{\partial x^2} + \frac{\partial^2 \mathbf{u}}{\partial y^2} \right) dz - \frac{1}{\delta} \int_0^\delta \rho_0 \beta c g \frac{\partial y}{\partial x} dz, \quad (2.8)$$

using Eqs. 2.6 and 2.7:

$$\frac{\partial \bar{p}}{\partial x} = -\frac{12\mu}{\delta^2} \bar{\mathbf{u}} + \mu \left(\frac{\partial^2 \bar{\mathbf{u}}}{\partial x^2} + \frac{\partial^2 \bar{\mathbf{u}}}{\partial y^2} \right) - \rho_0 \beta \bar{c} g \frac{\partial y}{\partial x}. \quad (2.9)$$

The form given by Eq. 2.9 is the sought two-dimensional equation. In vector form:

$$\nabla \bar{p} = -\frac{12\mu}{\delta^2} \bar{\mathbf{u}} + \mu \nabla^2 \bar{\mathbf{u}} - \rho_0 \beta \bar{c} g \nabla y, \quad (2.10)$$

with non zero ∇p and ∇y in the x direction only.

2.2.4 Brinkman number approach

The Brinkman's pre-factor (\mathcal{B}) consists of a constant correction factor that modifies the original Brinkman number ($\mathcal{B}r$) [38], and changes Eq. 2.10 to a form closer to Darcy's law. We mention that an approximation is made when we assume a parabolic velocity profile in the Hele-Shaw cell, and a correction in the Brinkman number is introduced, with the above defined pre-factor [39].

Accordingly, the term containing the laplacian operator appearing in Eq. 2.10 refers to the corrected Brinkman number. Eq. 2.10 takes, thus, the form:

$$\nabla \bar{p} = -\frac{12\mu}{\delta^2} \bar{\mathbf{u}} + \mathcal{B} \mu \nabla^2 \bar{\mathbf{u}} - \rho_0 \beta \bar{c} g \nabla y, \quad (2.11)$$

where \mathcal{B} refers to the Brinkman's pre-factor, which is given by $12/\pi^2$.

2.2.5 Non-dimensionalization process

This step comprises the non-dimensionalization process of Eq. 2.11, made with introduction of the following non-dimensional variables:

$$\mathbf{u}^* = \frac{\bar{\mathbf{u}}}{u_c}; \quad \rho^* = \frac{\rho}{\Delta\rho_0} = \frac{\rho}{\rho_A - \rho_0}; \quad \ell^* = \frac{\ell}{\ell_c}; \quad p^* = \frac{\bar{p}\kappa}{\mu D}; \quad \nabla^* = \ell_c \nabla; \quad \mathbf{g}^* = \frac{\mathbf{g}}{g}, \quad (2.12)$$

where: $u_c = \rho_0 g \kappa \alpha a_0 / \mu$ stands for the characteristic velocity, a_0 , for the initial concentration, $\kappa = \delta^2/12$ for the medium permeability, δ , for the distance between the plates of the Hele-Shaw cell, $\ell_c = D/u_c$ for the characteristic length, α and D , for the expansion and the diffusion coefficients. g stands for the gravitational acceleration magnitude, ρ_0 for the specific mass of the fluid, μ , for the fluid viscosity, and ρ_A for the undisturbed specific mass.

Introducing the non dimensional variables - Eqs. 2.12 - in Eq. 2.11, we obtain:

$$\frac{1}{\ell_c} \nabla^* \mu \frac{D}{\kappa} p^* = -\frac{\mu}{\kappa} u_c \mathbf{u}^* + \mu \frac{\mathcal{B}}{\ell_c^2} \nabla^{*2} u_c \mathbf{u} + \Delta \rho_0 \rho^* \mathbf{g}.$$

Next, we multiply this equation by $\frac{\ell_c \kappa}{\mu D}$, to obtain:

$$\nabla^* p^* = -\frac{\ell_c}{D} u_c \mathbf{u}^* + \frac{\kappa \mathcal{B}}{\ell_c^2} \nabla^{*2} \mathbf{u}^* + \frac{\ell_c \kappa g \Delta \rho_0}{\mu D} \rho^* \mathbf{g}^*.$$

By replacing the medium permeability κ , and the pre-factor \mathcal{B} in the Brinkman term we arrive to:

$$\mathcal{B}r = \frac{\delta^2}{\pi^2 \ell_c^2}.$$

In what concerns to the gravitational term, we have:

$$\frac{\ell_c \kappa g \Delta \rho_0}{\mu D} \rho^* \mathbf{g}^* = \frac{\kappa g \Delta \rho_0}{\mu} \frac{1}{u_c} \rho^* \mathbf{g}^*,$$

having in mind that $\ell_c = D/u_c$.

Assuming that $\rho = \rho_0(1 + \alpha a)$ we have $\rho_A = \rho_0(1 + \alpha a_0)$ and $\Delta \rho_0 = \rho_A - \rho_0 = \rho_0(1 + \alpha) a_0 - \rho_0 = \rho_0 \alpha a_0$. Taking also into account the definition of u_c , we simplify the gravitational term, to obtain:

$$\frac{\kappa g \rho_0 \alpha a_0}{\mu} \frac{1}{u_c} \rho^* \mathbf{g}^* = \frac{\kappa g \rho_0 \alpha a_0}{\mu} \frac{\mu}{\rho_0 g \kappa \alpha a_0} \rho^* \mathbf{g}^* = \rho^* \mathbf{g}^*.$$

We have, thus, the non-dimensional form of Eq. 2.11, given by:

$$\nabla p = -\mathbf{u} + \mathcal{B}r \nabla^2 \mathbf{u} + \rho \mathbf{g}, \quad (2.13)$$

where the asterisks were removed.

Eq. 2.13 can be used in two different approaches of the problem:

1. By assuming Darcy's law, we obtain:

$$\nabla p = -\mathbf{u} + \rho \mathbf{g}, \quad (2.14)$$

with $\mathcal{B}r \rightarrow 0$.

2. By assuming the Darcy-Brinkman's equation, we have:

$$\nabla p = \mathcal{B}r \nabla^2 \mathbf{u} + \rho \mathbf{g}, \quad (2.15)$$

with $Br \rightarrow \infty$.

2.2.6 Vorticity-stream function approach

Here, we take the curl of Eq. 2.14, to obtain the governing equations in the framework of the vorticity-stream function formulation.

Upon assuming $\rho = \beta c$ and $\mathbf{g}^T = [0 \quad -g \quad 0]$, we take the curl of $\beta c \mathbf{g}$, to successively obtain:

$$[\nabla \times \beta c \mathbf{g}] = \begin{vmatrix} e_1 & e_2 & e_3 \\ \partial/\partial x & \partial/\partial y & \partial/\partial z \\ 0 & -\beta c g & 0 \end{vmatrix} = \begin{bmatrix} 0 \\ 0 \\ -\frac{\partial}{\partial x} \beta c g \end{bmatrix},$$

thus:

$$[\nabla \times \beta c \mathbf{g}] = -\beta g_z \frac{\partial c}{\partial x}.$$

It is well known, from vector analysis, that $\nabla \times (\nabla F) = 0$, i.e., the curl of the gradient of scalar field vanishes [36]. In consequence, we have $\nabla \times (\nabla p) = 0$.

By taking the curl of Eq. (2.14), we obtain:

$$0 = -\omega_z - \beta g_z \frac{\partial c}{\partial x}, \quad (2.16)$$

where g_z denotes the gravitational acceleration along the z direction.

The vorticity transport equation, assuming Darcy's law, is then obtained from Eqs. 2.3 and 2.16:

$$\nabla^2 \psi = \beta g_z \frac{\partial c}{\partial x}. \quad (2.17)$$

2.3 Concentration equation

The mass transport equation of a chemical species, and assuming that diffusion follows the First Fick's law, and denoting the species concentration by c reads [36]:

$$\frac{\partial c}{\partial t} + \mathbf{u} \cdot \nabla c = \nabla \cdot (\mathcal{D} \nabla c),$$

where \mathcal{D} stands for the diffusion coefficient.

Assuming a constant diffusion coefficient, we have:

$$\frac{\partial c}{\partial t} + \mathbf{u} \cdot \nabla c = \mathcal{D} \nabla^2 c,$$

where the left hand side of this equation stands for the material derivative of c .

The transport equation of the concentration c may thus, be written in shorter form:

$$\frac{Dc}{Dt} = \mathcal{D} \nabla^2 c, \tag{2.18}$$

where D/Dt denotes the material derivative.

As shown in Secs. 2.2 and 2.3 the model equations governing the system evolution are given by:

$$\nabla^2 \psi = R \frac{\partial c}{\partial x}. \tag{2.19}$$

$$\frac{Dc}{Dt} = \mathcal{D} \nabla^2 c, \tag{2.20}$$

where $R = \beta g_z$ and g_z associates the z direction as the one of the gravitational acceleration.

2.4 Boundary conditions

This work addresses the effect of the curvature of the interface between two fluids, on the rate of dissolution the upper one, denser and partially miscible with the second one, placed underneath. The geometrical domain configurations, with a flat horizontal upper interface, and with deformed upper interface, where dissolution occurs, is schematically shown in Figure 4.

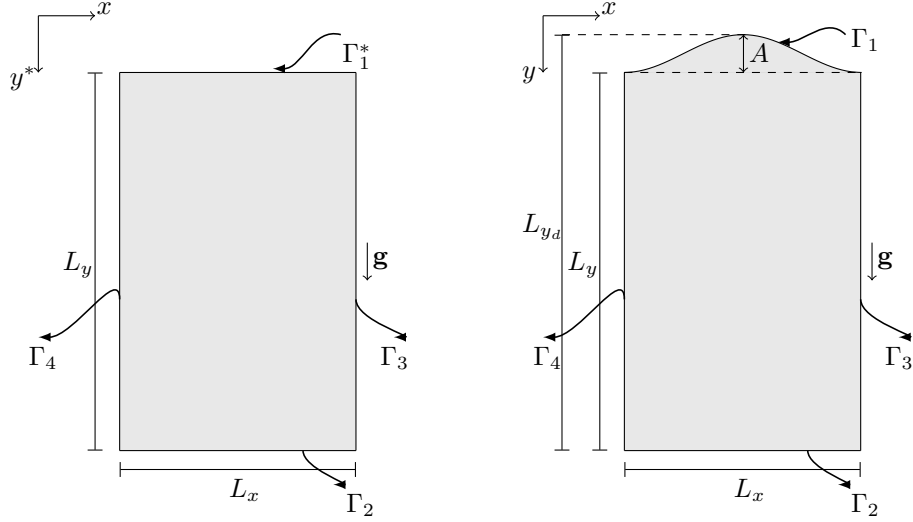


Figure 4: Left: A porous domain, with flat upper interface. At right: a domain with deformed interface. We denote the flat domain horizontal length by L_x , and the vertical length by L_y . The deformed vertical domain length is denoted by L_{y_d} . The coordinate system defined on the domain deforms, as the upper interface so does. We denote the undeformed coordinate system by (x, y^*) , and the deformed one, by (x, y) . A is the amplitude of the interface deformation.

Points of the undeformed domain are mapped into the points of the deformed one, according to the following formula:

$$y = y^* + \frac{A}{2} \left(1 - \frac{y^*}{L_y} \right) \left[1 - \cos \left(\frac{2\pi x}{L_x} \right) \right], \quad (2.21)$$

The boundary of the flat domain is defined by: $\Gamma^* = \Gamma_1^* \cup \Gamma_2 \cup \Gamma_3 \cup \Gamma_4$, whereas the deformed domain boundary is given by: $\Gamma = \Gamma_1 \cup \Gamma_2 \cup \Gamma_3 \cup \Gamma_4$.

Boundary conditions for the velocity field are prescribed as non-slip at the upper (Γ_1) and lower (Γ_2) boundaries, and periodic, along the lateral ones. In what concerns to the concentration field, we prescribe null flux at Γ_2 , periodic conditions at the side boundaries (Γ_3 and Γ_4) and $c = 1$ at the upper interface. Formally stating, we prescribe:

$$\mathbf{u} \cdot \mathbf{n} = 0 \quad \text{at } \Gamma_1 \quad \text{and } \Gamma_2 \quad (2.22)$$

$$\mathbf{n} \cdot \nabla c = 0 \quad \text{at } \Gamma_2 \quad (2.23)$$

$$c = 1 \quad \text{at } \Gamma_1. \quad (2.24)$$

Periodic boundary conditions were implemented to mimic the infinite domain, where the system state is repeated at the lateral sides with prescribed period. Figure 5 illustrates this

condition.

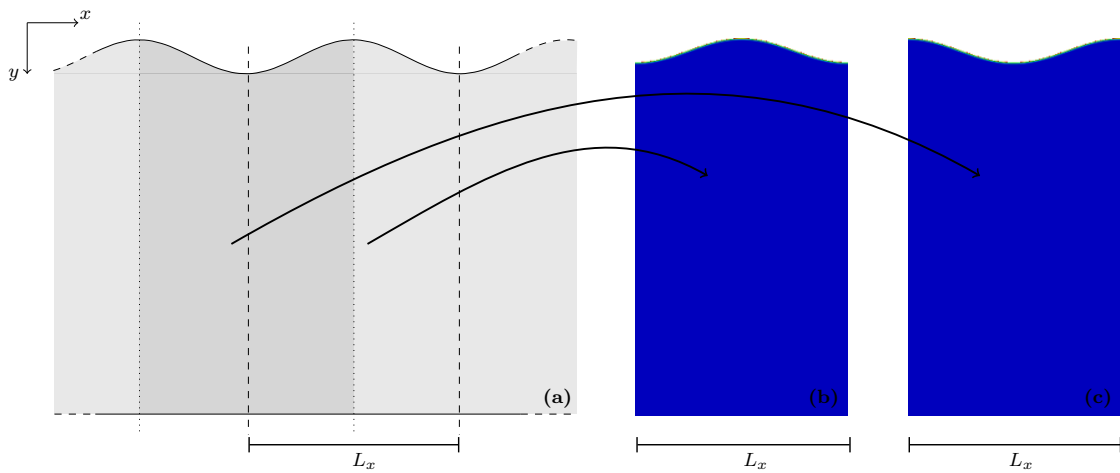


Figure 5: Schematic of periodic lateral boundaries.

Figure 5(b) represents the same configuration shown in Figure 4 and Figure 5(c) shows another configuration of the domain. Chapter 5 shows the first results configured according to Figure 5(b). However in Chapter 6 we show the results configured according to Figure 5(c), where the fingers better appears for larger amplitudes of deformation.

2.4.1 Initial condition

The dissolution process is initially dominated by a diffusion mechanism. The change to the convective regime results of an instability of the interface, which can be anticipated by the forcing of a deformed interface. A small perturbation is imposed to the concentration at the upper interface, in $t = 0$. The imposed perturbation takes the form:

$$c(x, y, t) = 1 + 2 \left(\text{rand} - \frac{1}{2} \right) \times 10^{-3}, \quad (2.25)$$

at $t = 0$, for $(x, y) \in \Gamma_1$, where rand stands for a random number between 0 and 1. For the remaining points of the domain, $\Omega - \Gamma_1$ we prescribe $c(x, y, t) = 0$ at $t = 0$.

2.5 Analytical solution

When the velocity field vanishes, namely, when $\nabla^2 \psi = 0$, the concentration field, evolving in compliance with Eqs. 2.19 and 2.20, becomes purely diffusive, with the concentration

distribution given by [40]:

$$c(y, t) = 1 - \operatorname{erf}\left(\frac{y}{2\sqrt{t}}\right). \quad (2.26)$$

Figure 6 presents a plot of analytical solution of concentration given by the Eq. 2.26. In this case, $L_y = 400$ and time of plot $t = 100$.

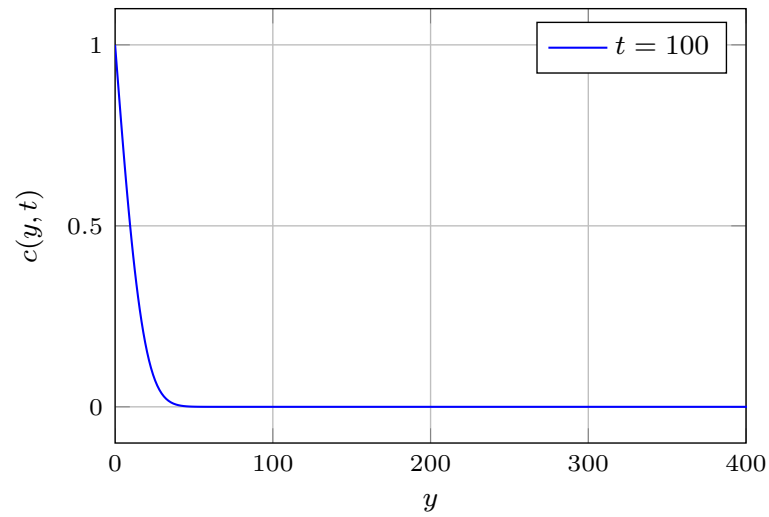


Figure 6: Concentration profile in absence of any flow at time $t = 100$.

3 METHODOLOGY

In this chapter we present the methodology adopted to solve numerically the governing equations and to analyse the numerical results of the subject problem of this thesis. The numerical method basically encompasses the Finite Element Method (FEM).

3.1 The Finite Element Method (FEM)

The Finite Element Method is widely used for solving boundary value problems. Continuous problems are replaced by a discrete approximated one with the following characteristics:

- (a) the continuous media is divided in a finite collection of parts (denoted as *elements*), with the behaviour of the elements characterized by the values assumed by a finite number of associated parameters;
- (b) the solution of the complete set of equations governing the behaviour of the discrete problem strictly follows the rules applicable to originally discrete problems [41] [42].

3.1.1 The Variational or Weak Formulation

Equations 2.19 and 2.20 are written in the strong form of the boundary value problem. Though some methods directly employ the strong formulation of the problem, the Finite Element Method assumes a different approach, where the governing equations are written in the weak or variational form of the problem.

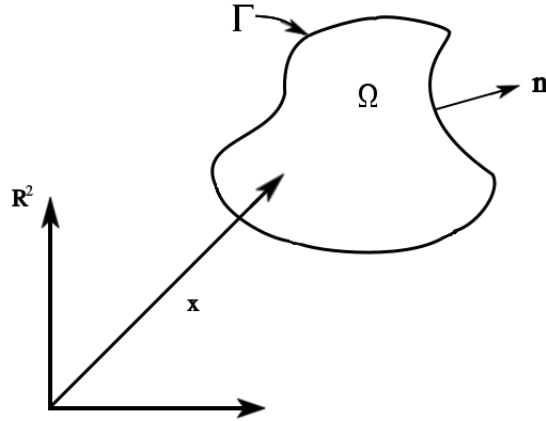


Figure 7: Representation of the domain for the finite element method.

The variational or weak form is obtained by weighing the governing differential equations with a suitable weighing function satisfying the condition $v \in \mathcal{V}$ and $v = 0$ in Γ_g , where Γ_g stands for the geometric boundary of the problem, and \mathcal{V} is the space of functions defined by:

$$\mathcal{V} := \{v \in \mathcal{H}^1(\Omega) \mid v = 0 \text{ in } \Gamma_c\},$$

with Γ_c being a possible contour of the domain Ω and \mathcal{H}^1 being the space defined by:

$$\mathcal{H}^1(\Omega) := \left\{ v \in \mathcal{L}^2(\Omega) \mid \frac{\partial v}{\partial x_i} \in \mathcal{L}^2(\Omega), i = 1, \dots, n \right\},$$

where $\mathcal{L}^2(\Omega)$ is the Lebesgue space, namely, the space of all square integrable functions, defined by:

$$\mathcal{L}^2(\Omega) := \left\{ v \mid \int_0^1 v^2 dx < \infty \right\}.$$

in this framework, the functional space \mathcal{H}^1 comprises all square-integrable functions also having square-integrable first derivatives.

By so weighting and subsequently integrating Eqs. 2.19 and 2.20 we obtain the weak

form of governing equations, in the form:

$$\int_{\Omega} \nabla \psi^T \nabla q \, d\Omega + R \int_{\Omega} c_x q \, d\Omega = 0 \quad (3.1)$$

$$\int_{\Omega} \frac{Dc}{Dt} r \, d\Omega + \int_{\Omega} \nabla c^T \nabla r \, d\Omega = 0, \quad (3.2)$$

where q and $r \in \mathcal{V}$.

The abstract and bilinear form of the set of Eqs. 3.1-3.2 are given by:

$$K(q, \psi) + \left(q, R; \frac{\partial c}{\partial x} \right) = 0, \quad (3.3)$$

$$M\left(r, \frac{Dc}{Dt} \right) + K_c(r, c) = 0, \quad (3.4)$$

where:

$$\begin{aligned} K(q, \psi) &= \int_{\Omega} \nabla \psi^T \nabla q \, d\Omega, \\ \left(q, R; \frac{\partial c}{\partial x} \right) &= R \int_{\Omega} c_x q \, d\Omega, \\ M\left(r, \frac{Dc}{Dt} \right) &= \int_{\Omega} \frac{Dc}{Dt} r \, d\Omega, \\ K_c(r, c) &= \int_{\Omega} \nabla c^T \nabla r \, d\Omega. \end{aligned}$$

3.1.2 The Galerkin Formulation

Let $\mathcal{U}^h \subset \mathcal{U}$ and $\mathcal{V}^h \subset \mathcal{V}$ be finite dimension spaces. We assume that for all $\mathbf{w}^h \in \mathcal{V}^h$, $\mathbf{w}^h = 0$ exactly or approximately, at least, in Γ_g .

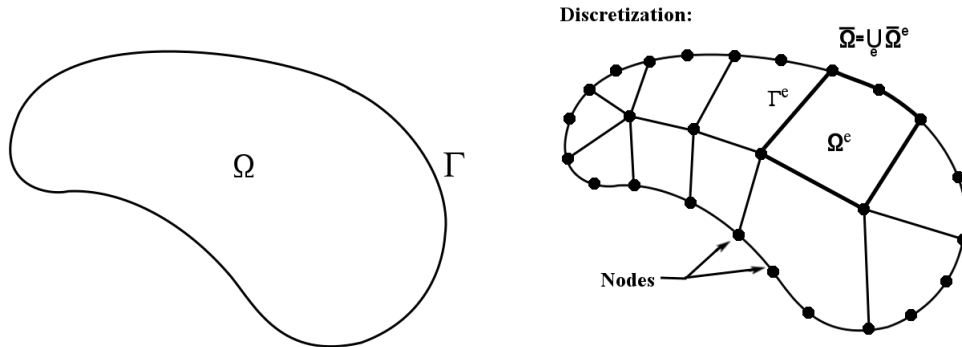


Figure 8: Representation of discretized domain. Left: domain before discretization and right: domain after discretization with nodes.

The domain discretization leads to subdomains Ω^e -elements, with $1 \leq e \leq n_{el}$, where n_{el} is the number of elements. The e elements can be, in bidimensional cases, either triangles or quadrilaterals.

The set of global number of nodes is defined by: $\eta = \{1, 2, \dots, n_{np}\}$, where n_{np} is the number of nodal points. We define $\eta_g \subset \eta$ as the set of the “g-nodes”, representing the set of nodes assigned to the domain boundary, which are prescribed. So, we address ourselves to evaluate the value of prescribed boundary variables. In other words, we iteratively solve $n_{eq} = \#(\eta - \eta_g)$ equations.

A typical member of \mathcal{V}^h holds the form:

$$q^h = \sum_{A \in \eta - \eta_g} N_A c_A, \quad (3.5)$$

where N_A is the shape function associated to the global node A and c_A stands for a constant.

Similarly,

$$r^h = \sum_{A \in \eta - \eta_g} N_A d_A, \quad (3.6)$$

where d_A is the unknown at the global node A .

Equations 3.3 and 3.4 can be written, in the vectorial form, as:

$$\mathbf{K}\psi + \mathbf{D}_x c = 0, \quad (3.7)$$

$$\mathbf{M} \frac{Dc}{Dt} + \mathbf{K}_c c = 0, \quad (3.8)$$

where \mathbf{K} and \mathbf{K}_c are stiffness matrices, \mathbf{M} is a mass matrix and \mathbf{D}_x is the matrix containing the gradient along the x direction.

3.1.3 Triangular element and natural coordinates

In this work we adopt triangular finite elements with straight edges, an approach that enables the use of natural coordinates (also denoted by area coordinates) to evaluate the shape functions.

Following this approach, we consider a triangle with vertices 1, 2 and 3 (in the counter clockwise sense) with area \mathcal{A} , divided in three areas $\mathcal{A}_1, \mathcal{A}_2$ and \mathcal{A}_3 , i.e., $\mathcal{A} = \mathcal{A}_1 + \mathcal{A}_2 + \mathcal{A}_3$.

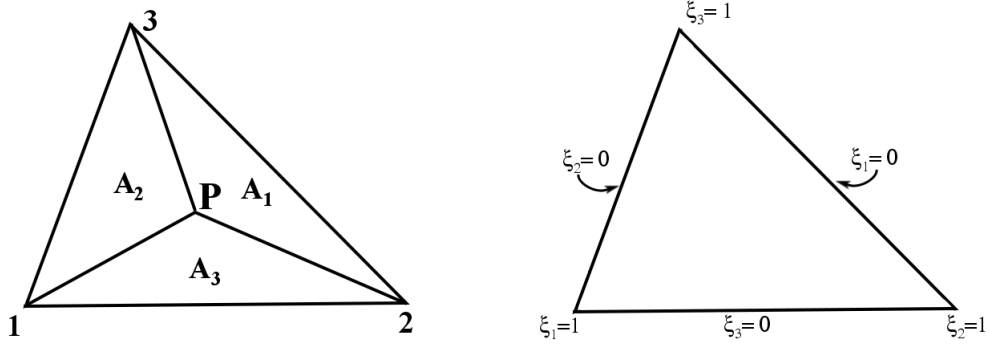


Figure 9: Sketch of triangular finite element. Left: areas \mathcal{A}_i of triangle and right: interpolation function ξ .

We can assume coordinates:

$$\xi_1 = \frac{\mathcal{A}_1}{\mathcal{A}}, \quad \xi_2 = \frac{\mathcal{A}_2}{\mathcal{A}}, \quad \xi_3 = \frac{\mathcal{A}_3}{\mathcal{A}},$$

having thus: $\xi_1 + \xi_2 + \xi_3 = 1$.

By considering next, the following interpolation function: $\phi(\xi_1, \xi_2, \xi_3) = \phi_1 \xi_1 + \phi_2 \xi_2 + \phi_3 \xi_3$, we have:

$$\begin{aligned} \xi_1 &= \frac{\mathcal{A}_1}{\mathcal{A}} = a_0^{(1)} + a_1^{(1)} x + a_2^{(1)} y \\ \xi_2 &= \frac{\mathcal{A}_2}{\mathcal{A}} = a_0^{(2)} + a_1^{(2)} x + a_2^{(2)} y \\ \xi_3 &= \frac{\mathcal{A}_3}{\mathcal{A}} = a_0^{(3)} + a_1^{(3)} x + a_2^{(3)} y \quad . \end{aligned}$$

We can also write the following system of equations, in order to perform the change of coordinates:

$$\begin{bmatrix} 1 \\ x \\ y \end{bmatrix} = \begin{bmatrix} 1 & 1 & 1 \\ x_1 & x_2 & x_3 \\ y_1 & y_2 & y_3 \end{bmatrix} \begin{bmatrix} \xi_1 \\ \xi_2 \\ \xi_3 \end{bmatrix} \Rightarrow \begin{bmatrix} 1 \\ x \\ y \end{bmatrix} = \mathbf{A} \begin{bmatrix} \xi_1 \\ \xi_2 \\ \xi_3 \end{bmatrix}$$

The coordinate system (ξ_1, ξ_2, ξ_3) , is obtained thus, by solving the following system of

equations:

$$\begin{bmatrix} \xi_1 \\ \xi_2 \\ \xi_3 \end{bmatrix} = \mathbf{A}^{-1} \begin{bmatrix} 1 \\ x \\ y \end{bmatrix},$$

By replacing $x_{ij} = x_i - x_j$, $y_{ij} = y_i - y_j$ with i and $j = 1, 2, 3$ and $2\mathcal{A} = \det(\mathbf{A}) = x_{21}y_{31} - x_{31}y_{21}$, we obtain the inverse matrix \mathbf{A}^{-1} :

$$\mathbf{A}^{-1} = \frac{1}{2\mathcal{A}} \begin{bmatrix} x_2y_3 - x_3y_2 & y_{23} & x_{32} \\ x_3y_1 - x_1y_3 & y_{31} & x_{13} \\ x_1y_2 - x_2y_1 & y_{12} & x_{21} \end{bmatrix}.$$

Writing the matrices associated to each element requires the use of differentiable interpolation functions, with respect to the cartesian coordinates. We consider thus:

$$N_a = N_a(\xi_1, \xi_2, \xi_3),$$

By deriving N_a with respect to the cartesian coordinates x e y , we obtain:

$$\begin{aligned} \frac{\partial N_a}{\partial x} &= \frac{\partial N_a}{\partial \xi_1} \frac{\partial \xi_1}{\partial x} + \frac{\partial N_a}{\partial \xi_2} \frac{\partial \xi_2}{\partial x} + \frac{\partial N_a}{\partial \xi_3} \frac{\partial \xi_3}{\partial x} \\ \frac{\partial N_a}{\partial y} &= \frac{\partial N_a}{\partial \xi_1} \frac{\partial \xi_1}{\partial y} + \frac{\partial N_a}{\partial \xi_2} \frac{\partial \xi_2}{\partial y} + \frac{\partial N_a}{\partial \xi_3} \frac{\partial \xi_3}{\partial y}. \end{aligned}$$

From the relationship between coordinates ξ_i e x, y , we have the following relations:

$$\begin{aligned} \frac{\partial N_1}{\partial x} &= \frac{y_{23}}{2\mathcal{A}}, & \frac{\partial N_2}{\partial x} &= \frac{y_{31}}{2\mathcal{A}}, & \frac{\partial N_3}{\partial x} &= \frac{y_{12}}{2\mathcal{A}} \\ \frac{\partial N_1}{\partial y} &= \frac{x_{32}}{2\mathcal{A}}, & \frac{\partial N_2}{\partial y} &= \frac{x_{13}}{2\mathcal{A}}, & \frac{\partial N_3}{\partial y} &= \frac{x_{21}}{2\mathcal{A}}. \end{aligned}$$

Integration of polynomials in ξ_1, ξ_2 e ξ_3 within the triangles area is given by:

$$\int_{\mathcal{A}} \xi_1^k \xi_2^l \xi_3^m d\mathcal{A} = 2\mathcal{A} \frac{k! l! m!}{(2+k+l+m)!}. \quad (3.9)$$

The gradient of the shape function N_a is given, for triangular elements in two dimen-

sions, by:

$$\nabla N_a = \begin{bmatrix} \frac{\partial N_1}{\partial x} & \frac{\partial N_2}{\partial x} & \frac{\partial N_3}{\partial x} \\ \frac{\partial N_1}{\partial y} & \frac{\partial N_2}{\partial y} & \frac{\partial N_3}{\partial y} \end{bmatrix} = \frac{1}{2\mathcal{A}} \begin{bmatrix} y_{23} & y_{31} & y_{12} \\ x_{32} & x_{13} & x_{21} \end{bmatrix}.$$

3.1.4 Global stiffness and mass matrices

Matrices \mathbf{K} and \mathbf{M} , obtained in eqs. 3.7 and 3.8 are denoted as stiffness and mass matrices, respectively. As shown before, these matrices are, in general, given by:

$$\mathbf{K} = \int_{\Omega} \nabla \psi^T \nabla q \, d\Omega = a(q, \psi) \quad (3.10)$$

$$\mathbf{M} = \int_{\Omega} \frac{Dc}{Dt} r \, d\Omega = (r, Dc/Dt). \quad (3.11)$$

Upon replacing the Galerkin form (Eqs. 3.5-3.6) in Eqs. 3.10 and 3.11, we obtain:

$$\mathbf{K} = \int_{\Omega} \nabla N_A^T \nabla N_B \, d\Omega = a(N_A, N_B) \quad (3.12)$$

$$\mathbf{M} = \int_{\Omega} N_A N_B \, d\Omega = (N_A, N_B), \quad (3.13)$$

where indices A and B refer to global element nodes.

The stiffness and mass matrices are in the global form, these matrices can be assembled by finite elements, thus:

$$\mathbf{K} = \sum_{e=1}^{n_{el}} \mathbf{K}^e \quad \text{and} \quad \mathbf{M} = \sum_{e=1}^{n_{el}} \mathbf{M}^e, \quad (3.14)$$

where $\mathbf{K}^e = [K_{AB}^e]$ and $\mathbf{M}^e = [M_{AB}^e]$, with global nodes A and B .

3.1.5 Assembly of the global stiffness and mass matrices

The assembly of global matrices is systematically made, through the data arrays which provides necessary informations about nodes and elements localization of a matrix. The LM array, *location matrix*, store these informations according to:

$$\text{LM}(a, e) = P, \quad (3.15)$$

where e is the element, a is the local node and P is the global equation number.

The nodal data is stored in the IEN array, the *element nodes array*, which systematically relates local node numbers to global node numbers:

$$\text{IEN}(a, e) = A, \quad (3.16)$$

where a is the local node number, e is the element number and A is the global node number.

To specify the global ordering of equations we define the ID array, also called the *destination array*, which relates the global nodes numbers and global equation numbers:

$$\text{ID}(A) = P, \quad (3.17)$$

where A is the global node number and P is the global equation number. Thus, we construct the relationship:

$$\text{LM}(a, e) = \text{ID}(\text{IEN}(a, e)). \quad (3.18)$$

For the global nodes A and B , if $A \neq 0$ and $B \neq 0$, we arrive to:

$$\mathbf{K}_{AB} = \mathbf{K}_{AB} + \mathbf{k}_{ab}^e, \quad (3.19)$$

where \mathbf{K} is the global matrix, \mathbf{k}_{ab}^e is the element matrix with a and b local nodes.

Let e_n and e_m be triangular elements. For each one we have the local and global nodes, according to Figure 10:

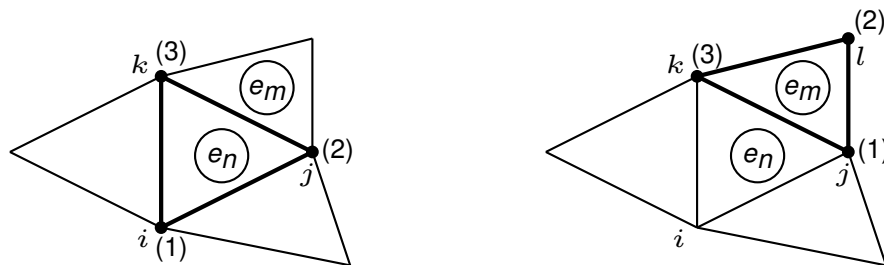


Figure 10: Triangular elements with local and global nodes.

In Figure 10, the subscripts (1), (2) and (3) are the local nodes and i , j , k and l are the

following simple form:

$$\mathbf{k}_{ab}^e = (\nabla N_a)^T \nabla N_b,$$

namely,

$$\mathbf{k}_{ab}^e = \frac{1}{4\mathcal{A}} \begin{bmatrix} y_{23} & x_{32} \\ y_{31} & x_{13} \\ y_{12} & x_{21} \end{bmatrix} \begin{bmatrix} y_{23} & y_{31} & y_{12} \\ x_{32} & x_{13} & x_{21} \end{bmatrix}.$$

We can thus, represent the stiffness matrix in a simplified form given by:

$$\mathbf{k}_{ab}^e = \frac{1}{4\mathcal{A}} \begin{bmatrix} y_{23}^2 + x_{32}^2 & y_{23}y_{31} + x_{32}x_{13} & y_{23}y_{12} + x_{32}x_{21} \\ y_{31}y_{23} + x_{13}x_{32} & y_{31}^2 + x_{13}^2 & y_{31}y_{12} + x_{13}x_{21} \\ y_{12}y_{23} + x_{21}x_{32} & y_{12}y_{31} + x_{21}x_{13} & y_{12}^2 + x_{21}^2 \end{bmatrix}.$$

The mass matrix associated to local nodes a and b is given by:

$$\mathbf{m}_{ab}^e = \int_{\Omega}^e N_a N_b d\Omega^e = \int_{\Omega}^e \xi_a \xi_b d\Omega^e.$$

By the Eq. 3.9 it is possible to calculate the entries of the element mass matrix, thus we obtain:

1. If $a = b$:

$$\mathbf{m}_{aa}^e = \int_{\Omega}^e \xi_a^2 d\Omega^e = 2\mathcal{A} \frac{2!}{4!} = \frac{\mathcal{A}}{6}.$$

2. If $a \neq b$:

$$\mathbf{m}_{ab}^e = \int_{\Omega}^e \xi_a \xi_b d\Omega^e = 2\mathcal{A} \frac{1!}{4!} = \frac{\mathcal{A}}{12}.$$

The element mass matrix is given thus, by:

$$\mathbf{M}^e = \frac{\mathcal{A}}{12} \begin{bmatrix} 2 & 1 & 1 \\ 1 & 2 & 1 \\ 1 & 1 & 2 \end{bmatrix}.$$

3.2 Mesh definition

As discussed in Sec. 2.4 of Chapter 2, we are concerned with a domain limited in the upper boundary by a deformed interface, which can be conveniently mapped to a rectangular domain using Eq. 2.21.

Thus, the mesh nodes are suitably generated in the rectangular domain, using a cartesian structured grid. The mesh is then generated from the cartesian grid nodes using either Delaunay triangulation or dividing each rectangular cell into two triangles in a fixed local topology.

Once the mesh on the rectangular domain is generated, it is mapped to the curvilinear domain employing Eq. 2.21. Note that the mapping given by Eq. 2.21 is employed only for the generation of the mesh. The solution of the linear system of equations is performed in cartesian coordinates on the deformed mesh, The Finite Element Method being responsible for the metrics due to the deformation of the elements in the final mesh.

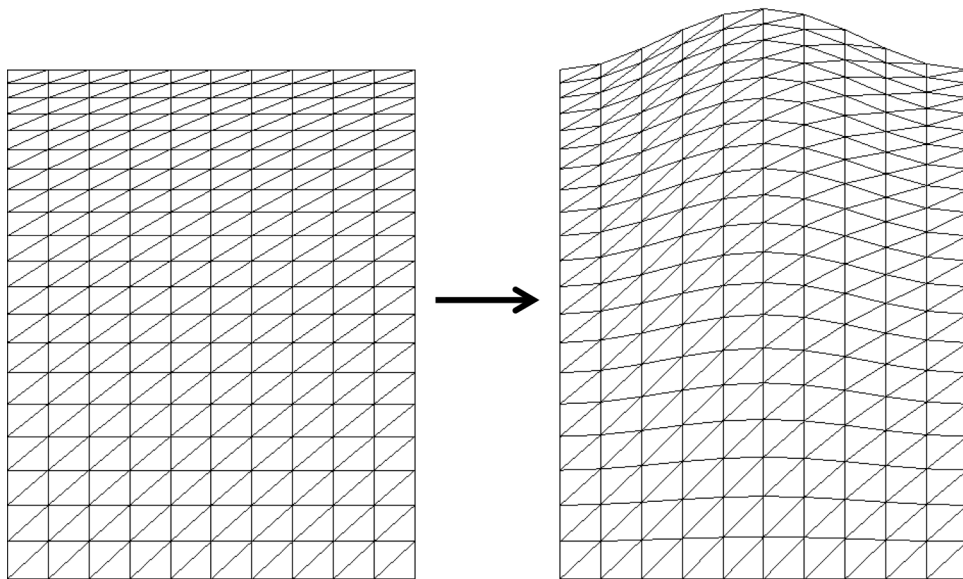


Figure 11: Example of mesh generation. Left: before mapping and at right: after mapping with deformed upper boundary.

3.3 The Crank-Nicolson Method

The mass transport equation comprises a material derivative term, which we discretize in time by using the second order in time Crank-Nicolson [43] method, which is numerically stable.

We look thus, for functions ψ and c satisfying the global form of equations:

$$\mathbf{K}\psi + \mathbf{D}_x c = 0, \quad (3.20)$$

$$\left(\frac{1}{\Delta t} \mathbf{M} - \frac{\alpha}{2} \mathbf{K} \right) c^{n+1} = \left(\frac{1}{\Delta t} \mathbf{M} + \frac{1-\alpha}{ReSc} \mathbf{K} \right) c^n - (\mathbf{u} \cdot \mathbf{D}_x + \mathbf{v} \cdot \mathbf{D}_y) c^n \quad (3.21)$$

where \mathbf{u} and \mathbf{v} are the diagonal matrices which represent the velocity. Indeed, we can use this form for the convective term in Eq. 3.21, due to use of the lumped mass matrix, that it is possible to approximate: $\mathbf{M}_L \cdot \mathbf{u} \cdot \mathbf{M}_L^{-1} \mathbf{D}_x$ to $\mathbf{u} \cdot \mathbf{D}_x$. The lumped mass matrix (\mathbf{M}_L) is a diagonal matrix that has in each element of its diagonal the sum of the elements of the respective row.

3.4 Computational implementation of the numerical method

Numerically solving algebraic linear systems of the form $Ax = b$ by direct methods usually results in numerically expensive implementations in terms of CPU time, for matrices of order 10^4 or higher. Alternatively, iterative methods are faster, and more suitable for solving linear system comprising large and sparse matrices. An approximate solution is obtained after a finite number of iterative steps.

The system of equations is solved in two steps. In the first one we obtain the stream function. Velocity components are then obtained and introduced in the transport equation, which is subsequently solved. An LU factorization is applied as a preconditioner to the matrices and the linear systems and the velocity field from the stream function solutions are then solved with the use of GMRES (Generalized Minimal Residual) solver. LU factorization as well as GMRES routines from the PETSc library are utilized [44].

Algorithm 1 describes the procedure employed in the numerical implementation.

Define: physical domain, number of triangular elements, amplitude of deformation, and time interval.

Create: nodal coordinates vectors and mesh connectivity matrix.

Apply: nonlinear vertical stretching to nodal coordinates vectors.

Define: boundary conditions vectors. *%Using the mesh*

Create: linear system matrices.

Apply: deformation in the upper boundary.

Assemble: finite element matrices (stiffness and mass).

Apply: boundary conditions in the matrices.

Impose: initial condition in the concentration vector.

Define: solvers for each unknown variable.

For each iteration:

Compute: concentration vector.

Apply: boundary conditions.

Compute: Darcy vector and applies the boundary conditions.

Solve: Darcy equation linear system.

Solve: concentration equation.

Post-process: save profiles, mixing length, space time maps, and other data.

Stop: when the prescribed final time is reached.

Algorithm 1: Algorithm employed in the numerical implementation

3.5 Characterization of the fingering structure

In this section, we present the characterization procedure of the nonlinear dynamics of the concentration and velocity fields [45], [8].

Given the bidimensional concentration field, we obtain the averaged profiles in each direction at successive times. The transverse average profile (x -direction) is defined as:

$$\langle c(y, t) \rangle = \frac{1}{L_x} \int_0^{L_x} c(x, y, t) dx. \quad (3.22)$$

$\langle c(x, t) \rangle$ gathers information about the total amount of CO_2 stored in a layer located at a distance y . In the diffusive regime it coincides with the analytical solution and in the convective regime indicates which position in the y -direction the finger has reached in a

given time. The longitudinal averaged profile is given by:

$$\langle c(x, t) \rangle = \frac{1}{L_y} \int_0^{L_y} c(x, y, t) dy. \quad (3.23)$$

$\langle c(x, t) \rangle$ gathers information about the level of interaction between fingers.

The transverse profile allows to define the mixing length and the area under the curve of the profile. The mixing length ($L(t)$) represents the distance between the upper interface and the tip of the finger with larger length. It is evaluated from the transverse average profile, and is given by the minimum y coordinate such that $\langle c(y, t) \rangle \geq 0.01$, as a function of time. In the diffusive regime, $L(t) = 2\sqrt{t} \operatorname{erf}^{-1}(0.99)$, where t is time (see Appendix A).

The area under the curve of the transverse profile represents the amount of solute dissolved in the brine as a function of the time:

$$S(t) = \int_0^{L_y} \langle c(y, t) \rangle dy. \quad (3.24)$$

An important figure is the dissolution flux, defined as the rate at which solute dissolves through of the upper boundary [8], [27]. This figure is given by:

$$F(t) = \frac{1}{L_x} \int_0^{L_x} \mathbf{n} \cdot \nabla c \Big|_{y=0} dl, \quad (3.25)$$

where $dl = dx/n_y$, and n_y is the y component of the unit normal vector.

The dynamics of the system may be captured by mapping the maximum and minimum points of the longitudinal average profile at successive times. This mapping also captures the number of fingers over time.

We also built a space-time map of concentration of the solute at a fixed distance $\Delta y'$ from the upper boundary and saved the concentration along the horizontal direction in the time. $\Delta y'$ was chosen sufficiently small to capture the onset of the fingers.

Figure 12 exemplify the space-time map constructed with $\Delta y' = 0$, namely, on the top of some domain.

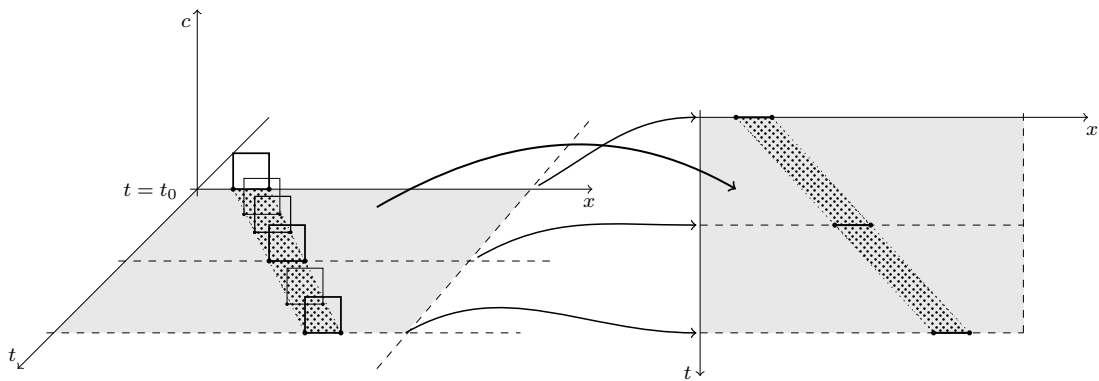


Figure 12: Mapping the space-time concentration.

Figure 13 shows the system state at four time moments of the evolution, where we identify four y -coordinates at which we construct space-time charts (see Figure 14). Flat interface was assumed and runs were performed with domain length $L_x = 600$ and $L_y = 800$ and final time 25000. Figure 14 shows space-time charts with the distance from the top $\Delta y' = 5\%, 10\%, 30\%$ and 50% , i.e., $\Delta y' = 40, 80, 120$ and 400 , respectively.

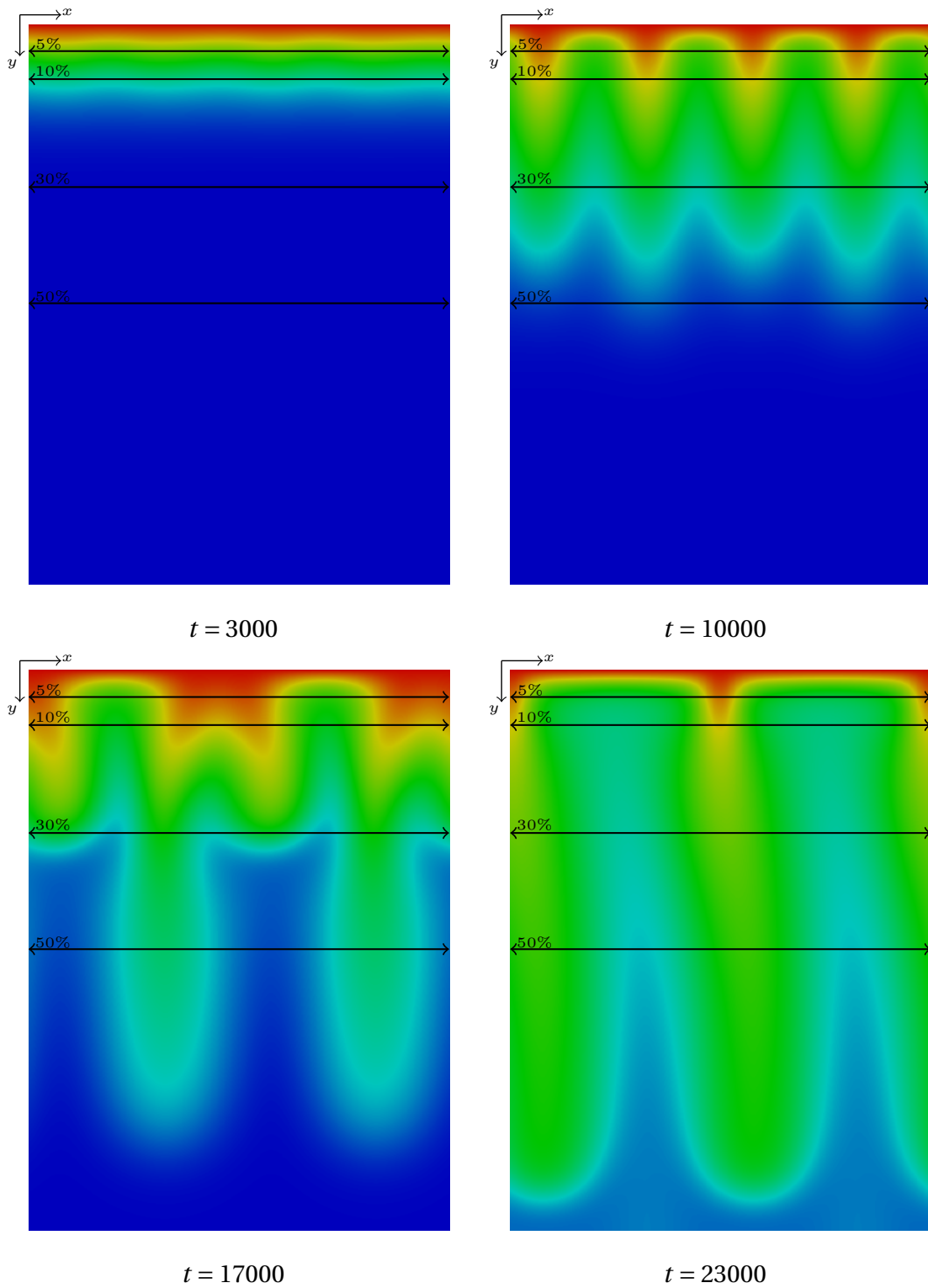


Figure 13: Time evolution of simulation with flat interface and identifying the y -coordinates at which we construct the space-time charts.

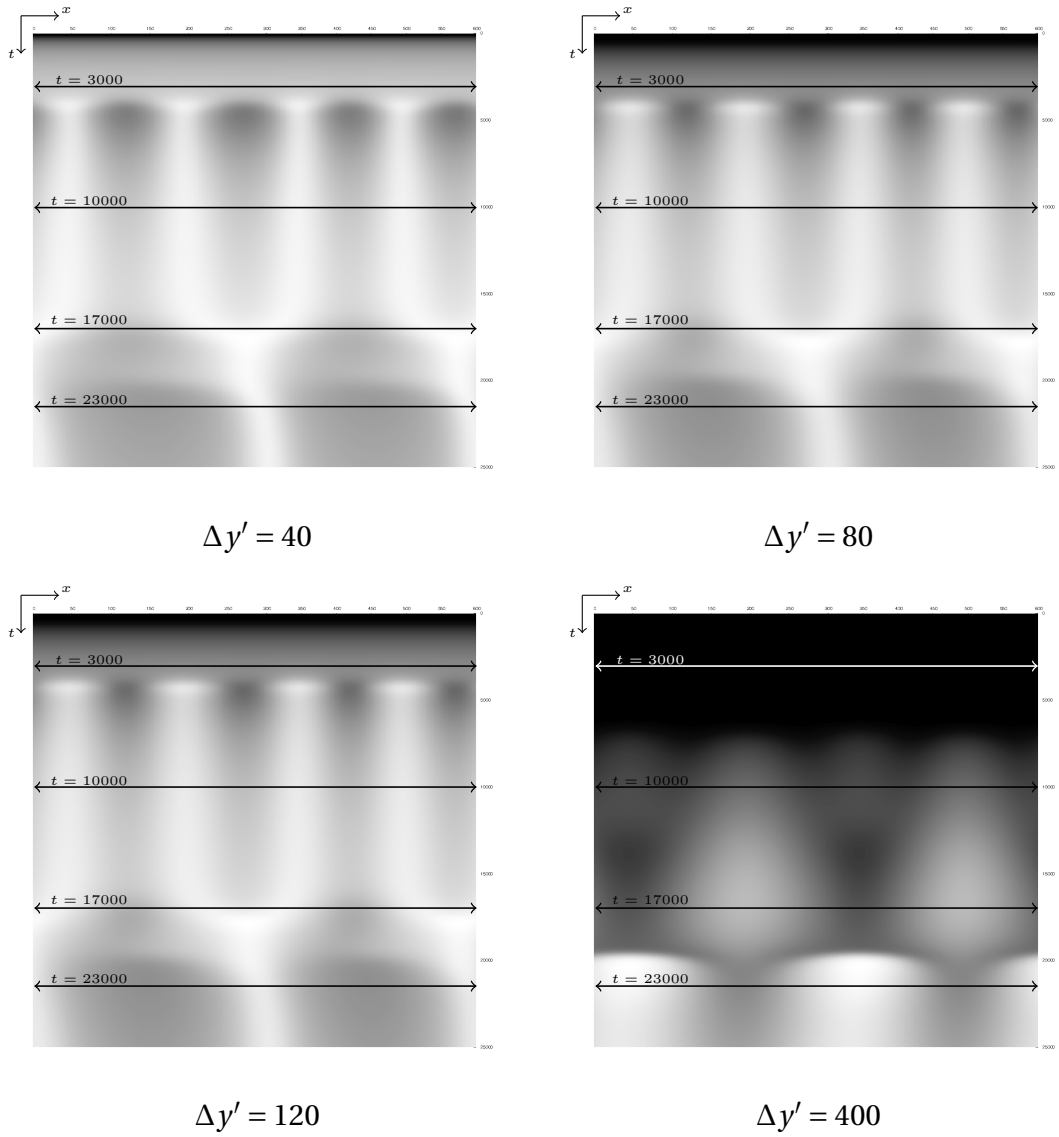


Figure 14: Space-time maps identifying prescribed times of evolution.

4 LINEAR STABILITY ANALYSIS ON A FLAT INTERFACE

In this chapter we consider the linear stability of perturbations near a flat interface. Accordingly, we address the base state with perturbations to obtain the linear analysis equations which lead to a eigenvalue-eigenfunction problem.

The base state of the problem is the time dependent solution of Eq. 2.20 of the concentration field in absence of any flow ([40]):

$$\bar{c}(y, t) = 1 - \operatorname{erf}\left(\frac{y}{2\sqrt{t}}\right). \quad (4.1)$$

The Linear Stability Analysis (LSA) consists in adding perturbations to the base state solution characterized by the concentration profile (4.1) and

$$\begin{pmatrix} c \\ \psi \end{pmatrix} = \begin{pmatrix} \bar{c}(y, t) \\ 0 \end{pmatrix} + \begin{pmatrix} \bar{c}(y) \\ \frac{i}{k}\tilde{\psi}(y) \end{pmatrix} \exp(\sigma t + ikx), \quad (4.2)$$

where $i^2 = -1$, k is the wavenumber of the perturbation and σ is the growth rate. The linearised evolution equations for the disturbances \tilde{c} and $\tilde{\psi}$ are thus:

$$\tilde{\psi}_{yy} - k^2\tilde{\psi} = k^2\tilde{c} \quad (4.3)$$

$$\sigma\tilde{c} + \tilde{\psi}\bar{c}_y = \tilde{c}_{yy} - k^2\tilde{c}, \quad (4.4)$$

where the subscripts denote partial derivatives.

Boundary conditions for the concentration and stream function perturbations \tilde{c} and $\tilde{\psi}$ are thus:

$$\begin{aligned} y = 0: & \quad \tilde{c} = 0, \quad \tilde{\psi} = 0 \\ y \rightarrow \infty: & \quad \tilde{c} \rightarrow 0, \quad \tilde{\psi} \rightarrow 0. \end{aligned}$$

Upon defining the differential operator $D^n = d^n/dy^n$ with $n = 1, 2$, a we rewrite Eq. 4.3:

$$(D^2 - k^2)\tilde{\psi} = k^2\tilde{c}, \quad (4.5)$$

and inversely:

$$\tilde{\psi} = (D^2 - k^2)^{-1} k^2 \tilde{c}. \quad (4.6)$$

Upon replacing $\tilde{\psi}$ in Eq. 4.4 and rearranging terms we arrive at an eigenvalue-eigenfunction equation for the rate of growth σ and associated vertical concentration profile in the form:

$$\left[(D^2 - k^2) - (D^2 - k^2)^{-1} k^2 D \bar{c} \right] \tilde{c} = \sigma \tilde{c}.$$

On the basis of Eqs. 2.19- 2.20, a LSA can be performed to obtain dispersion curves giving the growth rate of the perturbations as a function of the wavenumber (see Figure 15). We can see that all perturbations are damped for $t < 55.59$ and a bifurcation occurs at $t = 55.59$ when the first perturbation becomes marginally stable with a wavenumber $k = 0.06192$.

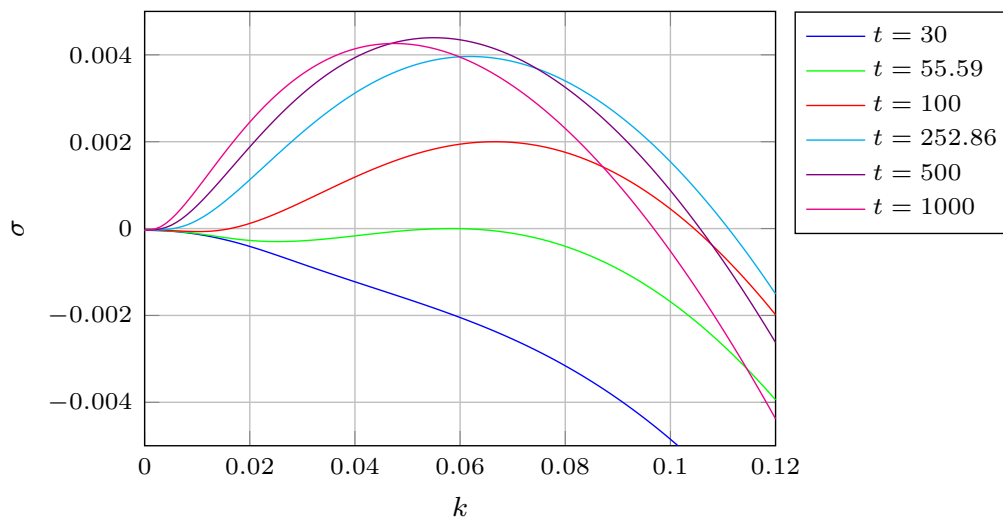


Figure 15: Dispersion curves of normal mode perturbations of the base state, numerically obtained for several times. All perturbations are damped for $t < 55.59$. A bifurcation occurs at $t = 55.59$ when the first perturbation becomes marginally stable with a wavenumber $k = 0.06192$.

4.1 Code validation – perturbation growth with frozen base state

This section describes the procedure adopted to validate the Finite Elements code developed in Matlab®, used to solve Eqs. 2.19-2.20. Section 4.1.1 addresses the effect of the mesh spacing on the rate of growth of perturbations σ . Section 4.1.2 compares values of σ given by the linear stability analysis with the ones of a specific mode ($k_0 = 0.06192$), as

extracted from the numerical integration of the governing equations with frozen base state at $t_0 = 252$. This condition is expressed by $\psi = 0$ and a concentration distribution according to:

$$c = \left(1 - \operatorname{erf}\left(\frac{y}{2\sqrt{t_0}}\right)\right) + a \tilde{c}(t_0, y) \cos(k_0 x). \quad (4.7)$$

Here $\tilde{c}(t_0, y)$ is the eigenfunction associated to k_0 , as obtained from the linear stability analysis at $t_0 = 252$ and a is the amplitude of the perturbation at $t = 0$.

4.1.1 Mesh spacing

In order to evaluate the effect of the mesh refinement we performed a series of 10 experiments where we measured the rate of growth of a perturbation as above (Eq. 4.7). The experiments were performed with the following conditions:

1. Domain dimensions: $\lambda \times 4\lambda$, along the x and y directions, respectively. Here λ is the wavelength associated with perturbations with $k_0 = 0.06192$;
2. Freezing the base state: at the end of each time step we subtracted the base state at $t = 252 + \Delta t$ from the numerical solution and added the base state at $t_0 = 252$. Δt is the time step used in the integration procedure;
3. Mesh construction: for each of the 10 experiments we set a grid of $N \times M$ points equally spaced along the x and y directions respectively, as given in Table 2. After setting the grid points we proceeded with a Delaunay triangulation by the Matlab function (see Figure 16);
4. Error evaluation was made by comparing the rate of growth of the perturbation with $k_0 = 0.06192$, evaluated at 31st time step of each run with the “exact” value obtained from the linear stability analysis ($\sigma_{\text{exact}} = 3.9581 \times 10^{-3}$ at $t = 252$), according to following formula:

$$\varepsilon_{rel} = \frac{|\sigma_{\text{approx}} - \sigma_{\text{exact}}|}{\sigma_{\text{exact}}} \times 100. \quad (4.8)$$

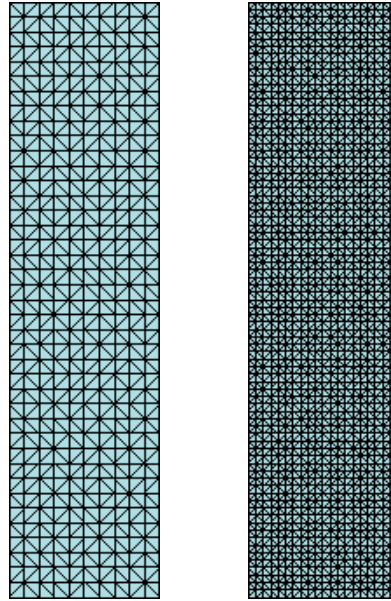


Figure 16: Two uniform meshes used in the in the experiments conducted to evaluate the effect of the mesh refinement on the results of the numerical integration of Eqs. 2.19 - 2.20. N and M are the number of points along the x and y directions, respectively. Left: $N = 11$ and $M = 41$. Right: $N = 21$ and $M = 81$.

Table 2 summarizes the information about the 10 experiments: number of points of the mesh along directions x e y , distance Δx between successive points in both directions, rate of growth σ_{approx} obtained from each experiments and error, according to Eq. 4.8.

Table 2: σ_{approx} and error in the rate of growth, evaluated at the 31st time step according to Eq. 4.8 for 10 mesh refinements.

N	M	Δx	σ_{approx}	ε_{rel} (%)
11	41	10.14726	$2.5512 \cdot 10^{-3}$	35.5451
21	81	5.07363	$3.55812 \cdot 10^{-3}$	10.1056
31	121	3.38242	$3.76779 \cdot 10^{-3}$	4.8085
41	161	2.53682	$3.83377 \cdot 10^{-3}$	3.1416
51	201	2.02945	$3.86949 \cdot 10^{-3}$	2.2392
61	241	1.69121	$3.88869 \cdot 10^{-3}$	1.7541
71	281	1.44961	$3.90002 \cdot 10^{-3}$	1.4677
81	321	1.26841	$3.90789 \cdot 10^{-3}$	1.2688
91	361	1.12747	$3.9134 \cdot 10^{-3}$	1.1298
101	401	1.01473	$3.91775 \cdot 10^{-3}$	1.0199

Figure 17 shows that the error is proportional to Δx^2 for coarse meshes and proportional to Δx for fine meshes.

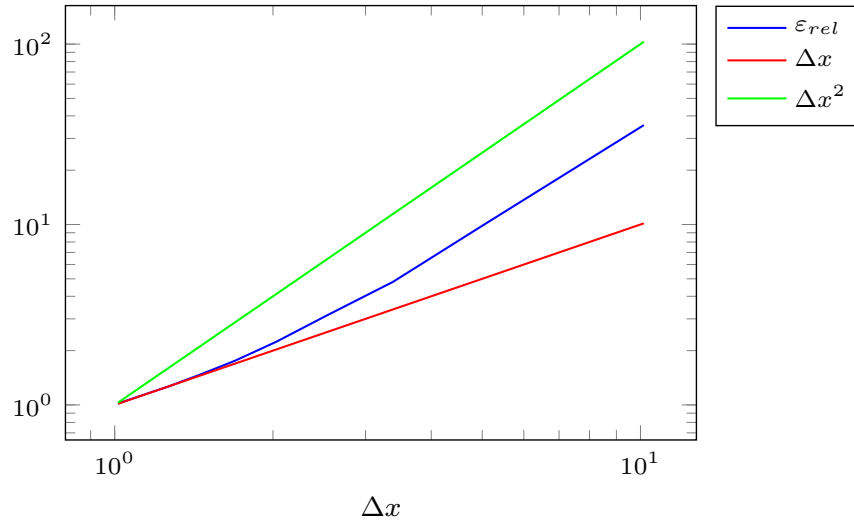


Figure 17: Comparison between relative error, distance Δx and distance Δx^2 . This figure shows that the error is proportional to Δx^2 for coarse meshes and proportional to Δx for fine meshes.

4.1.2 The rate of growth of perturbations with frozen base state

This section reports the experiments conducted to evaluate the rate of growth of modes with the wavelength λ associated to $k_0 = 0.06192$. We denote this mode as “mode 4”. Initial condition used in the experiments consisted of the base state at $t = 252$ plus perturbation with this wavenumber.

Having in mind that meshes with 161 points distributed along a domain with a length of 4λ in the y direction result in errors of order of 3% in the rate of growth we adopted a domain with dimensions $4\lambda \times 4\lambda$ in all simulations and a grid with 150 points evenly spaced along the x direction and 150 points along the y direction, with a quadratically increasing distance between successive points (see Figure 18).

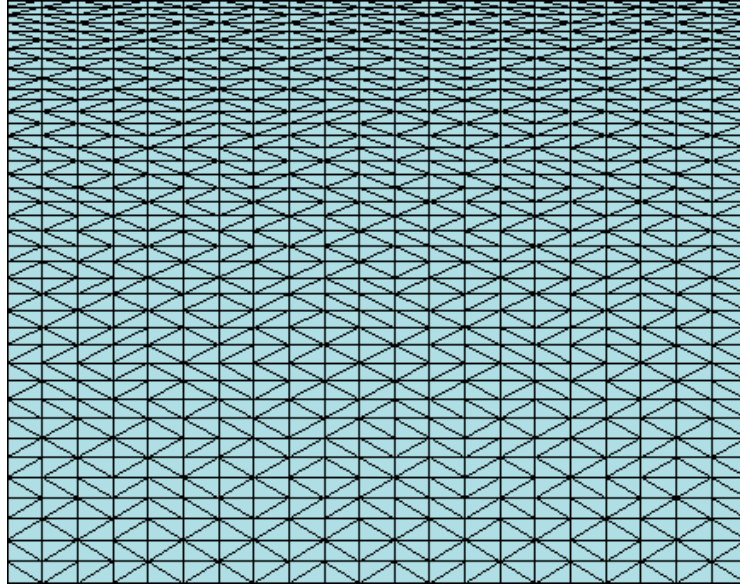


Figure 18: A non-uniform grid with $N \times M = 150 \times 150$ points.

Figure 19 shows a plot of the square of the amplitude of mode 4 as a function of time. Six experiments were run with different initial amplitude of the perturbations a (see Eq. 4.7) as indicated in Figure 19. The figure shows that perturbations with higher initial amplitude attain saturation earlier than perturbations with smaller initial amplitude. The growth is exponential, except at the first moments of evolution of a perturbation with the smaller initial amplitude, probably due to interference with other modes introduced by the numerical grid. We also included a curve (in black) of the growth of a perturbation as given by the linear stability analysis at $t = 252$. We observe that this curve shows a slope identical to the slope obtained from integration of the complete evolution equations, a result that validates the code.

In order to extract the amplitude of mode 4 we adopted the following procedure:

1. The base state is subtracted from result of the numerical result of integration, both at the same time;
2. The result is integrated along the y direction, followed by evaluation of the Fourier transform of the result, giving the sought amplitude.

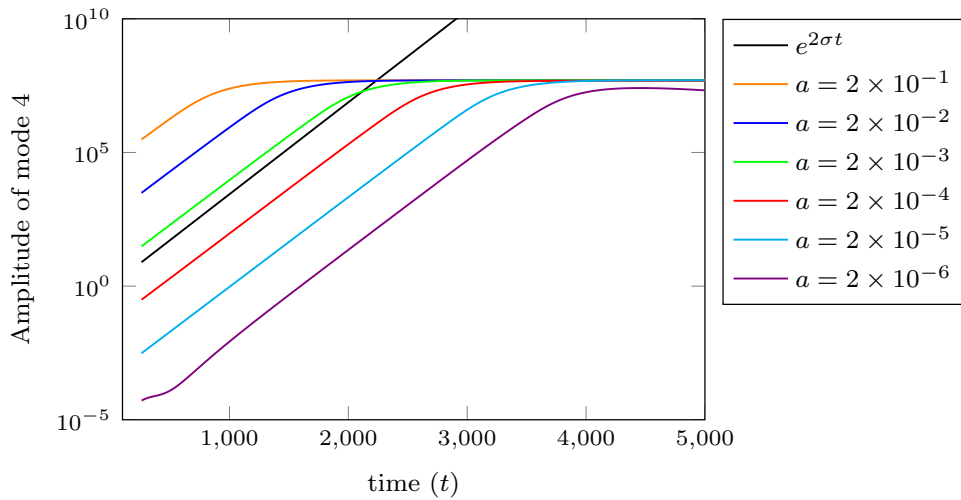


Figure 19: Evolution of the amplitude of Mode 4 for initial amplitudes as given in the figure.

Figure 20 presents a plot of the rate of growth σ as a function of time. This figure confirms that the the rate of growth obtained from the numerical integration of the evolution equations matches the “exact” value from the linear stability analysis during the stages of linear growth, except for the case where we started from a perturbation with very small initial amplitude and the mode is affected by the grid noise.

This figure also shows the horizontal line, in black, corresponding to σ as given by the linear stability analysis. As above mentioned, the curve associated with the smaller initial amplitude $a = 2 \times 10^{-6}$ shows an irregular behaviour at first instants, due to grid noise.

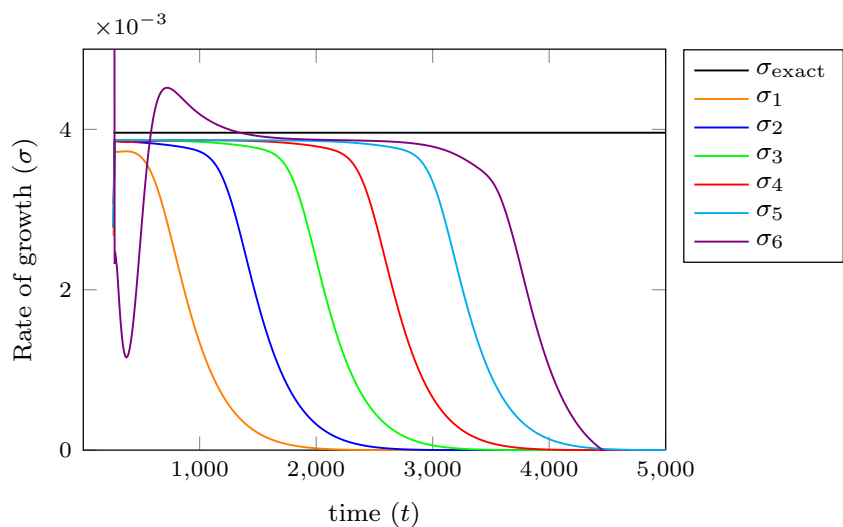


Figure 20: The “exact” rate of growth and rates of growth $\sigma_1, \sigma_2, \sigma_3, \sigma_4, \sigma_5$ and σ_6 associated to perturbations with initial amplitudes $a = 2 \times 10^{-1}, a = 2 \times 10^{-2}, a = 2 \times 10^{-3}, a = 2 \times 10^{-4}, a = 2 \times 10^{-5}$ e $a = 2 \times 10^{-6}$, respectively.

4.2 Deployment of instabilities with variable base state

In this section we investigate the deployment of instabilities with a time dependent base state by numerically integrating Eqs. 2.19-2.20 from random initial conditions (Sec. 4.2.1) and from initial conditions consisting of mode 4 (Sec. 4.2.2). In both cases we run the experiments with different amplitudes of the initial condition.

4.2.1 Random initial conditions

Figure 21 presents a plot of the concentration profile of the base state at various times, as given by Eq. 4.1 (lines with marks) and the profiles obtained by numerical integration of Eqs. 2.19-2.20 (lines without marks). The curves are averaged along the x direction. The figure shows the base state and deviation of the base state due to the onset of instabilities at the first stages of evolution, starting from random initial conditions. This figure shows adherence of the concentration profile to the base state up to $t = 1000$ at least. Deviation from the base state solution after $t = 3000$ evidences the onset of instabilities.

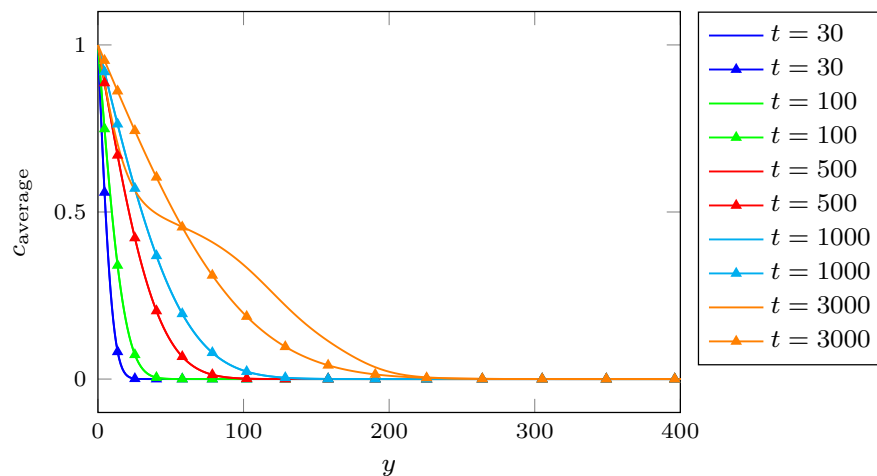


Figure 21: Comparison of concentration profiles at several times, as given by the solution of Eq. 4.1 (lines with marks) and obtained by numerical integration of Eqs. 2.19-2.20 (lines without marks). Base state and deviation of the base state due to the onset of instabilities at the first stages of evolution, starting from random initial conditions. Deviation from the base state solution at $t = 3000$ evidences the growth of unstable modes.

Figure 22 shows the amplitude of perturbation modes of concentration and stream function obtained from the solution of the governing equations using Fourier analysis, at $t = 1500$. The figure presents the vertical eigenmodes associated perturbations with 2, 3, 4 and 5 fingers (modes 2, 3, 4 and 5) at $t = 1500$. The modes were obtained by subtracting the base

state at $t = 1500$ from the result of the integration at that time, followed by the extraction of the modes by applying fast Fourier transform. This figure shows that the modes are identified by the corresponding number of fingers.

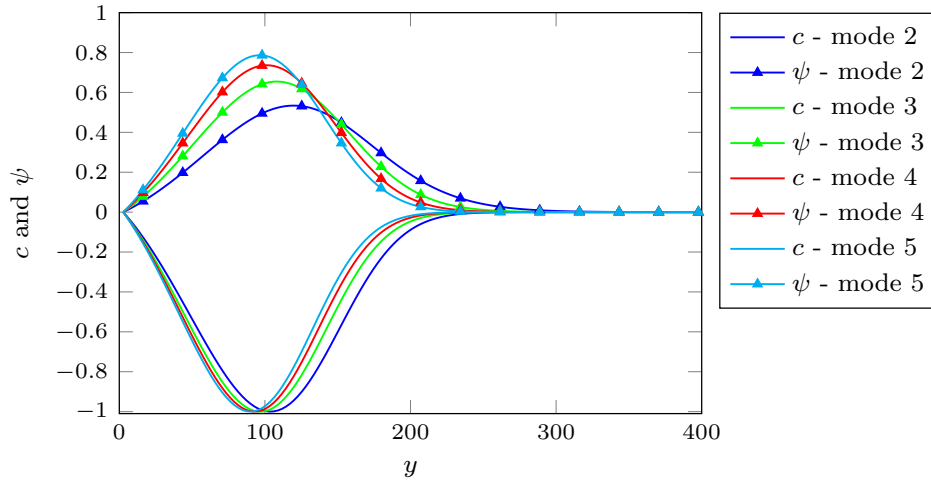


Figure 22: Perturbation eigenfunctions at $t = 1500$. Perturbation modes of ψ are represented by lines with marks and concentration, by lines without marks. Mode profiles were obtained by subtraction of the base state from the result of the numerical integration of Eqs. 2.19-2.20, followed by averaging along the x direction and by decomposition in Fourier modes. Modes are identified by the corresponding number of fingers.

Figure 23 shows the result of a simulation with random initial condition, where we can see that mode 3, containing three fingers, prevails in domains with dimensions $4\lambda \times 4\lambda$.

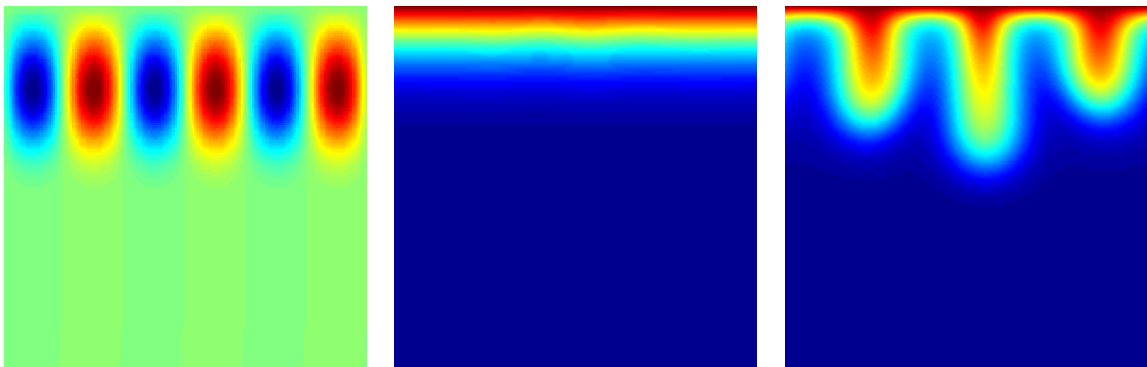


Figure 23: Left: concentration profile of mode 3 at $t = 1500$. Center and right: concentration distribution at times $t = 1500$ and $t = 3000$.

Figure 24 and Figure 25 present the amplitude of modes 3 and 4 for different random initial conditions. A comparison between Figure 24 and Figure 25 shows that the growth of mode 3 persists for times $t = 3000$ and longer.

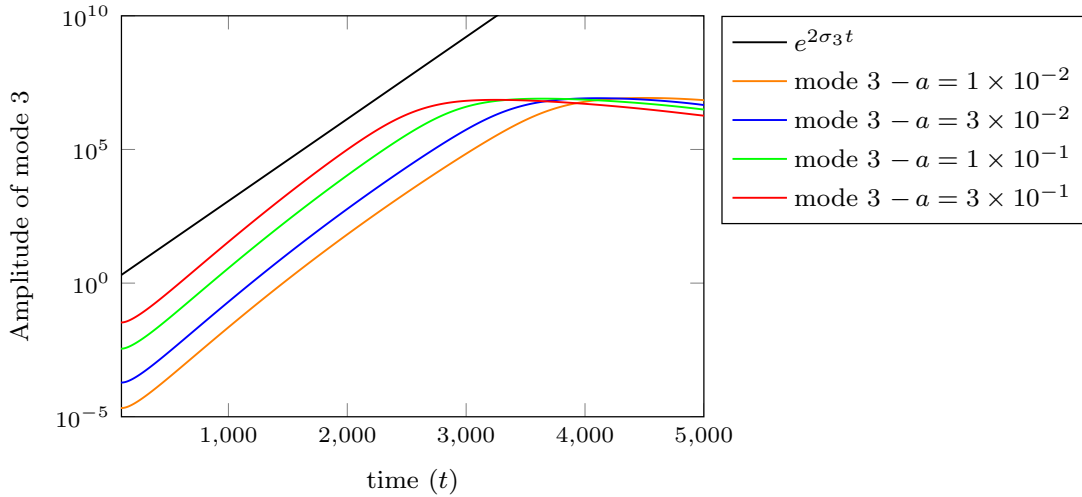


Figure 24: Amplitude of mode 3 for several amplitudes a of the random initial condition and evolving base state. In black: growth of the amplitude of mode 3, as given by the linear stability analysis at $t = 252$.

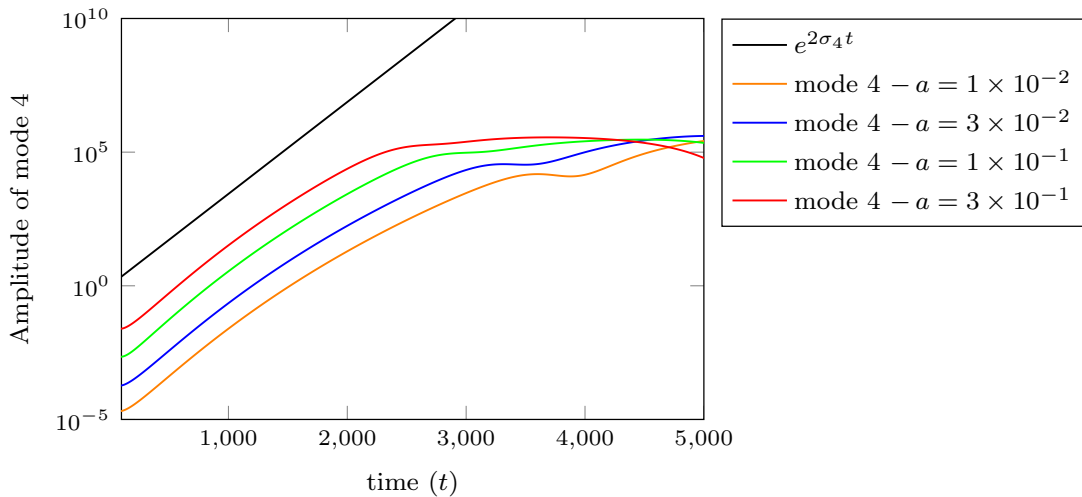


Figure 25: Amplitude of mode 4 for several amplitudes a of the random initial condition and evolving base state. In black: growth of the amplitude of mode 4, as given by the linear stability analysis at $t = 252$.

Figure 26 and Figure 27 present the rate of growth of modes 3 and 4 for four different initial amplitudes of the random initial condition. These figures show that the rate of growth changes significantly in time due to the deployment of the base state.

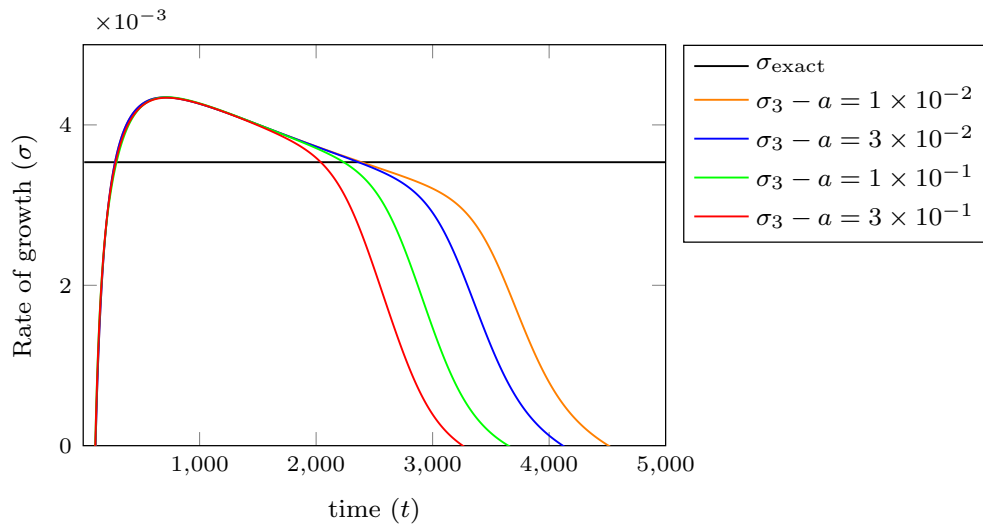


Figure 26: Rate of growth of mode 3 with four different initial amplitudes of the random initial condition. This figure shows that the rate of growth changes significantly in time due to the deployment of the base state.

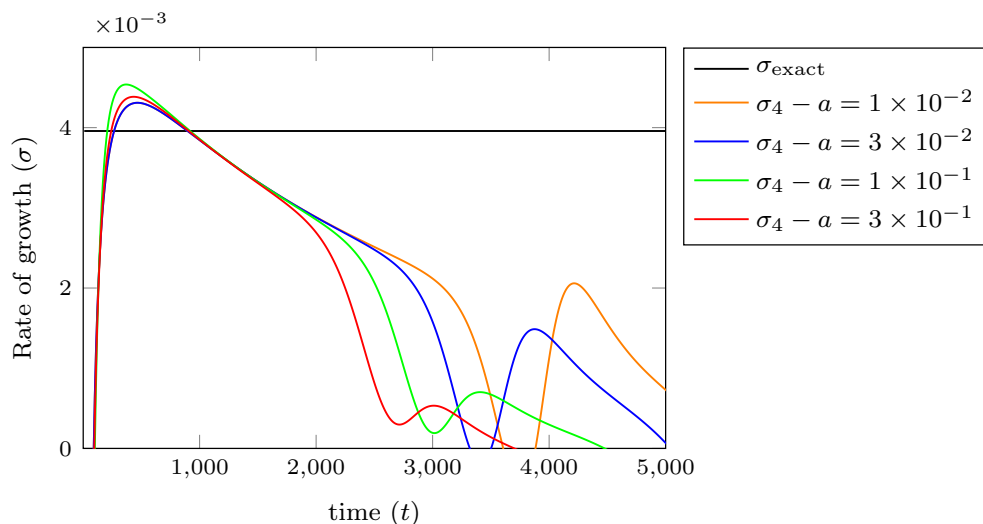


Figure 27: Rate of growth of mode 4 with four initial amplitudes of the random initial condition. In black: rate of growth of mode 4 as given by the linear stability analysis at $t = 252$. In addition to showing the decrease of the rate of growth the figure also shows the long term behavior of the mode as strongly nonlinear effects become dominant.

4.2.2 Initial condition: mode 4

This section reports the simulations starting from the base state at $t_0 = 252$ plus mode 4 with different amplitudes a of the initial condition, according to Eq. 4.7.

Figure 28 presents a plot of the concentration profile of the base state at various times, as given by Eq. 4.1 (lines with marks) and the profiles obtained by numerical integration of

Eqs. 2.19-2.20 (lines without marks). The curves are averaged along the x direction. Similarly to the case with random initial conditions. This figure shows adherence of the concentration profile to the base state up to $t = 1000$ at least. Deviation from the base state solution after $t = 3000$ evidences the onset of instabilities.

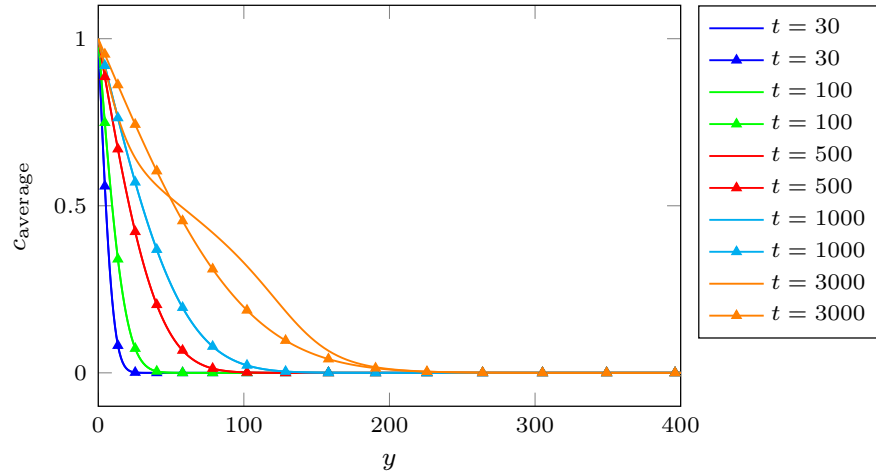


Figure 28: Base state and deviation of the base state due to the onset of instabilities at the first stages of evolution, starting from the base state at $t_0 = 252$ plus mode 4 with different amplitudes a of the initial condition. This figure presents a comparison of concentration profiles at several times, as given by the solution of Eq. 4.1 (lines with marks) and obtained by numerical integration of Eqs. 2.19-2.20 (lines without marks). Deviation from the base state solution at $t = 3000$ evidences the growth of unstable modes. Initial condition consisting of mode 4 (the most stable mode at $t = 252$ with initial amplitude $a = 2 \times 10^{-4}$).

Figure 29 presents the perturbation modes of ψ and the concentration c obtained by subtraction of the base state from the result of the numerical integration of Eqs. 2.19-2.20, followed by averaging along the x direction and by decomposition in Fourier modes. Modes are identified by the corresponding number of fingers. In this simulation the initial condition consists of mode 4, ie, the most stable mode at $t = 252$ with initial amplitude $a = 2 \times 10^{-4}$.

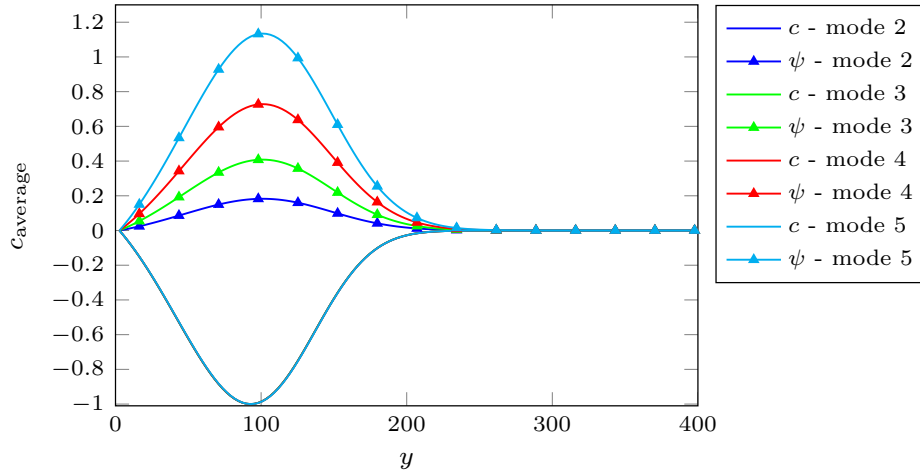


Figure 29: Perturbation eigenfunctions at $t = 1500$. Perturbation modes of ψ are represented by lines with marks and concentration modes, by lines without marks. Modes were obtained by subtraction of the base state from the result of the numerical integration of Eqs. 2.19-2.20, followed by averaging along the x direction and by decomposition in Fourier modes. Modes are identified by the corresponding number of fingers. Initial condition consisting of mode 4 (the most stable mode at $t = 252$ with initial amplitude $a = 2 \times 10^{-4}$).

Figure 30 shows the result of a simulation with initial condition mode 4, where we can see that the initial condition induces the development of four fingers.

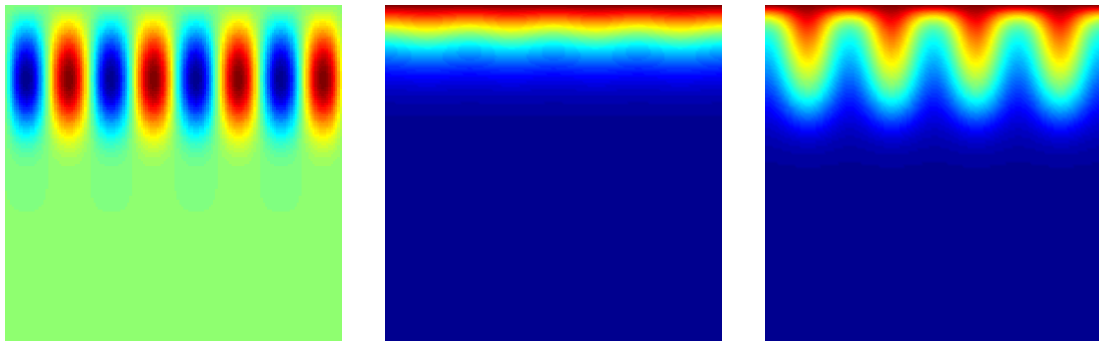


Figure 30: Left: concentration profile of mode 4 at $t = 1500$. Center and right: concentration distribution at times $t = 1500$ and $t = 3000$.

Figure 31 and Figure 32 show the amplitude and rates of growth of mode 4 with the different initial amplitudes a of the perturbation.

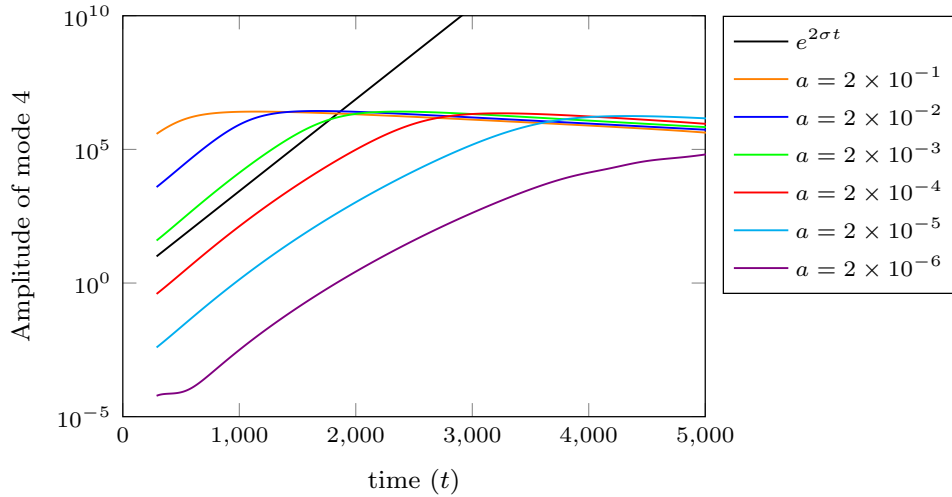


Figure 31: Amplitude of mode 4 for several amplitudes a of the initial condition and evolving base state. In black: growth of the amplitude of mode 4, as given by the linear stability analysis at $t = 252$.

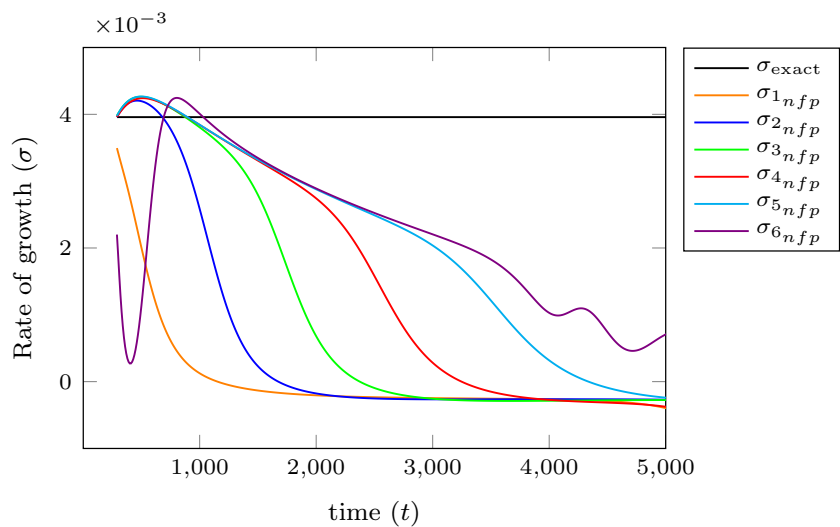


Figure 32: Rate of growth of mode 4 with the different initial amplitudes a of the perturbation (mode 4). In black: rate of growth of mode 4, as given by the linear stability analysis at $t = 252$.

Simulations made with an initial condition consisting of the concentration distribution of mode 4 are compared with results obtained by freezing the base state and the ones obtained by integration of the full evolution equations, where the base state evolves (see Figure 33 and Figure 34).

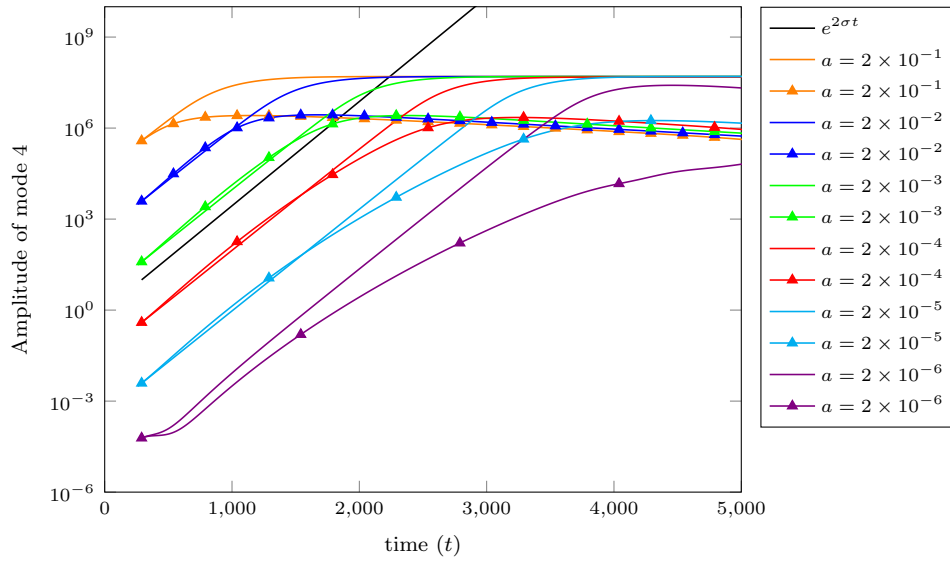


Figure 33: A comparison between the evolution of the amplitude of mode 4 with frozen base state (curves without marks) and evolving base state (curves with marks).

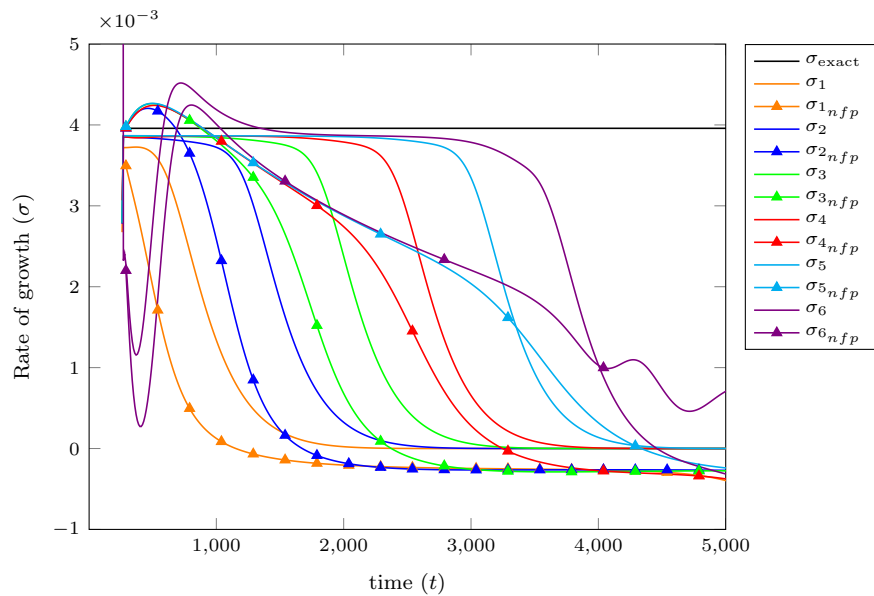


Figure 34: A comparison between the evolution of the rate of growth of mode 4 with frozen base state (curves without marks) and evolving base state (curves with marks).

In conclusion, freezing the base state profile does not qualitatively change the pattern of fingers developed and, at the same time, renders easier the analysis of the developed pattern.

4.3 The nonlinear regime

Figure 35, Figure 37 and Figure 38 show the evolution from earlier stages of mode selection, linear growth to saturation and strongly nonlinear regime for initial conditions consisting of the base state at $t = 252$ and random initial conditions and for same base state plus mode 4. In both cases we performed simulations with different amplitudes of the perturbation added to the base state at $t = 0$.

4.3.1 Random initial condition

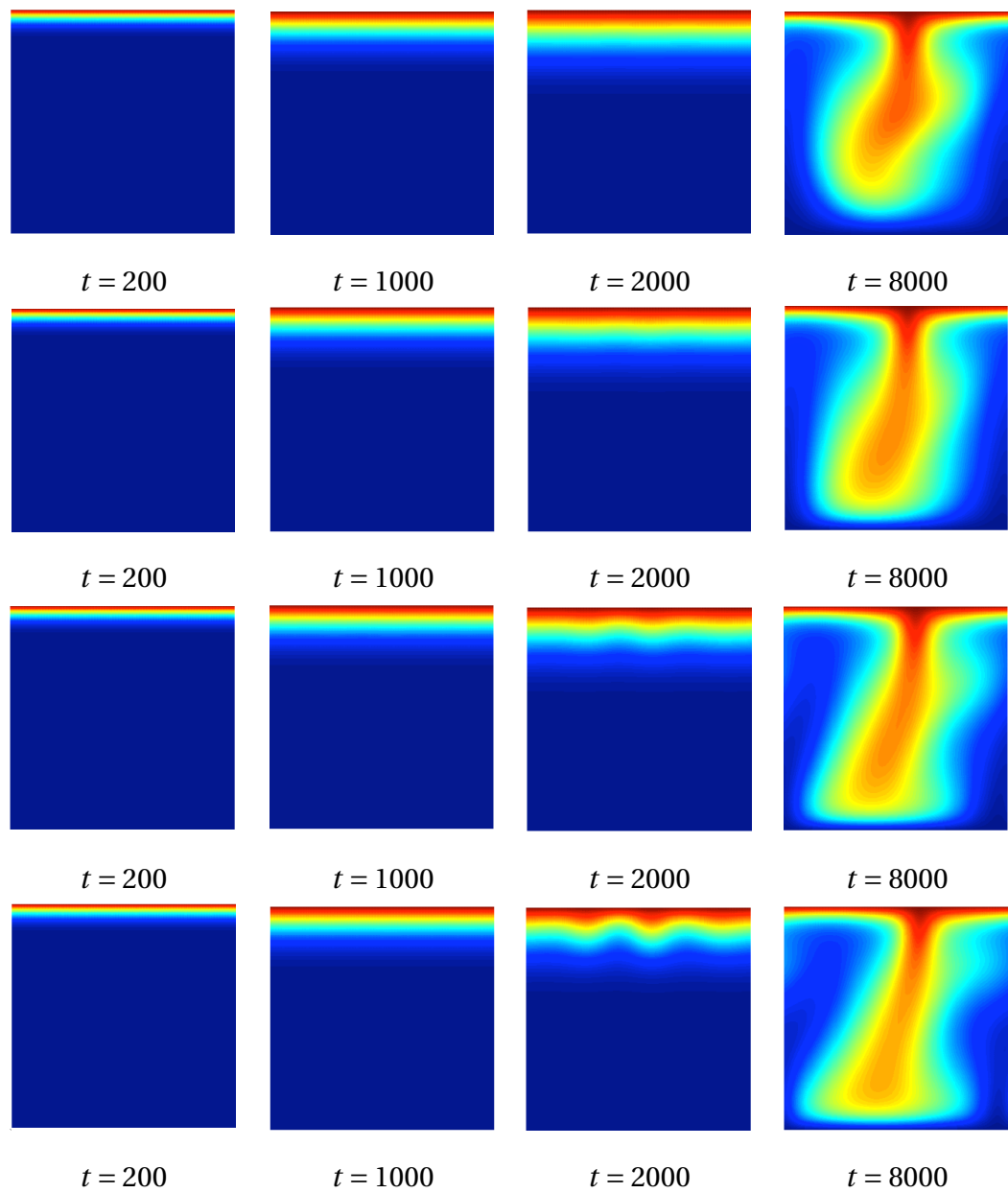


Figure 35: Time evolution of the concentration consisting of the base state at $t = 252$ and random initial conditions with initial amplitudes $a = 1 \times 10^{-2}$, $a = 3 \times 10^{-2}$, $a = 1 \times 10^{-1}$ and $a = 3 \times 10^{-1}$. The frames cover the stages of modes selection, linear growth, saturation of growth and strongly nonlinear regime.

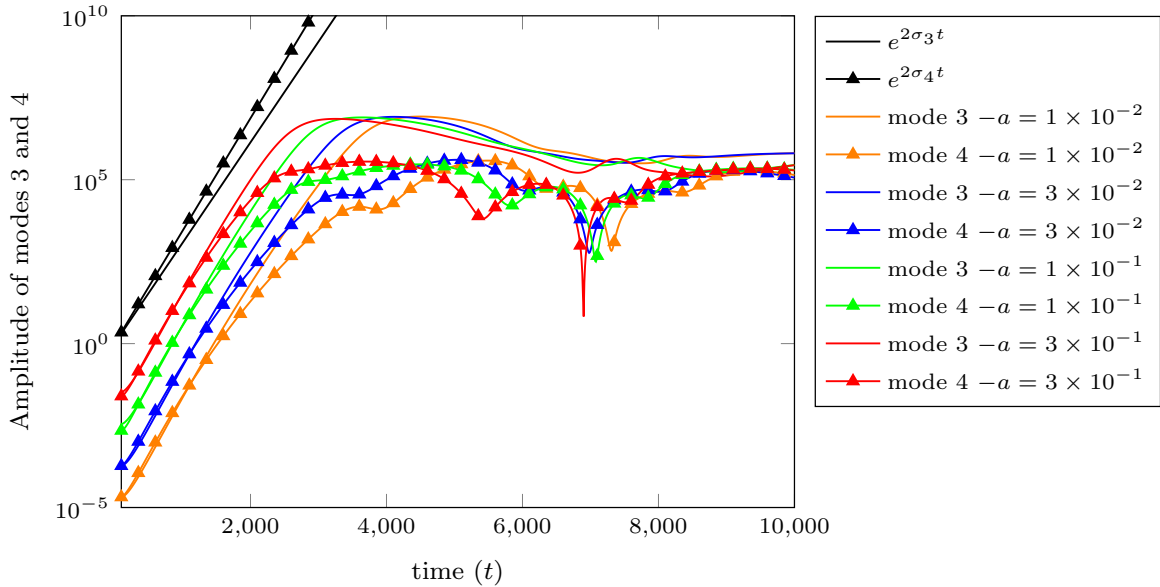


Figure 36: Long term evolution of modes 3 and 4 starting from initial conditions consisting of the base state at $t_0 = 252$ plus a random distribution with four initial amplitudes a (see Eq. 4.7). Black lines show the rate of growth from LSA. Curves of mode 3 a constructed without marks; curves of mode 4 a constructed with marks.

Figure 35 shows the effect of the amplitude of the initial condition in the number of fingers of the structure at $t = 2000$. The point becomes clear by observing the evolution of the amplitude of the modes (see also Figure 36). A numerical simulation performed with $a = 3 \times 10^{-1}$ shows that an instability appears at $t = 2000$, resulting in structures with larger number of fingers. Figure 36 also shows that the amplitude of mode 3 dominates (same a and t) over other modes.

For times $t = 2000$ to $t = 8000$, we observe the development of instabilities, containing initially a large number of modes close to the concentration boundary layer, though a single mode eventually survives for longer times. The result confirms the ones obtained by Figure 36.

4.3.2 Initial condition: mode 4

Figure 37 and Figure 38 present the system evolution starting with mode 4 as the initial condition, and different amplitudes. Prescription of this initial condition and larger amplitudes result in patterns with four fingers since early stages of evolution. For instance, assuming $a = 2 \times 10^{-1}$ a structure with four fingers already exists at $t = 260$. As the structure grows and nonlinear effects appear the number of surviving fingers is reduced to 1-3 ($t = 8000$).

These instabilities are also shown in Figure 39 at times $t = 6000$ and $t = 10000$.

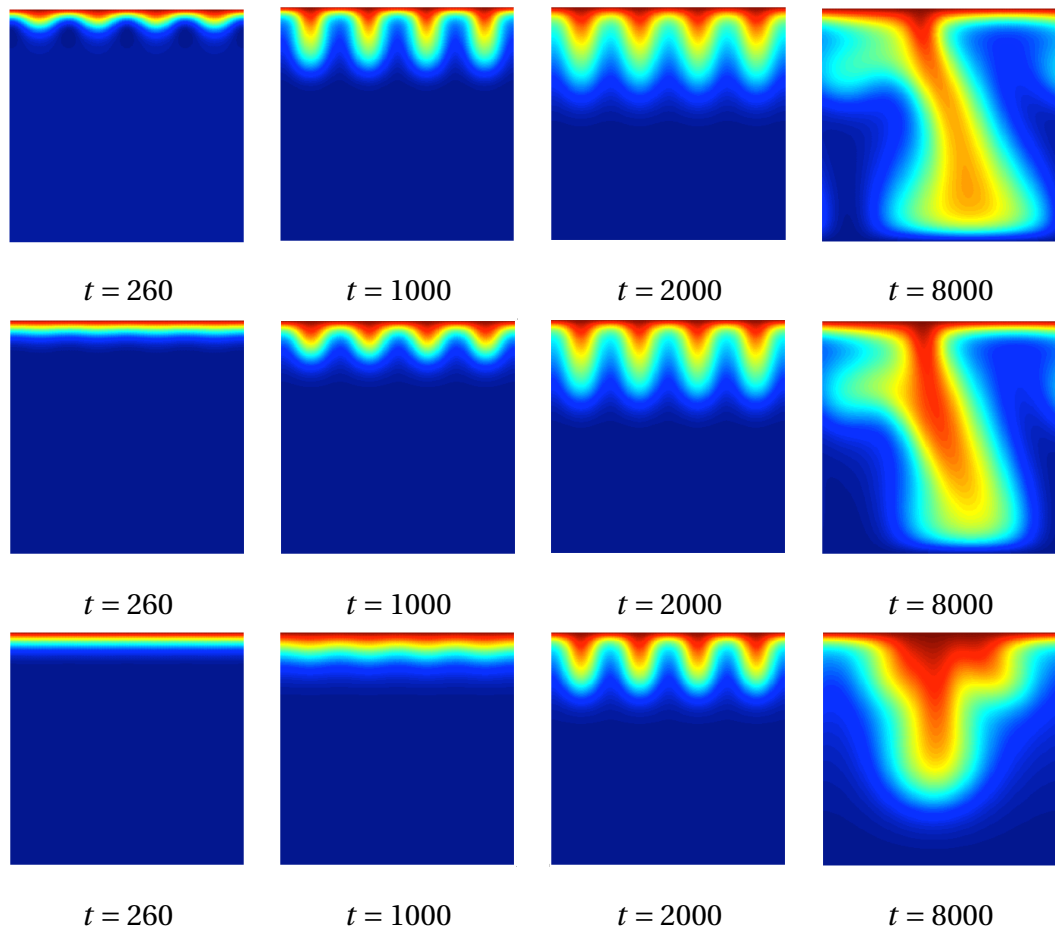


Figure 37: Time evolution of the concentration from the base state at $t = 252$ and mode 4 with initial amplitudes $a = 2 \times 10^{-1}$, $a = 2 \times 10^{-2}$ and $a = 2 \times 10^{-3}$ (see Eq. 4.7).

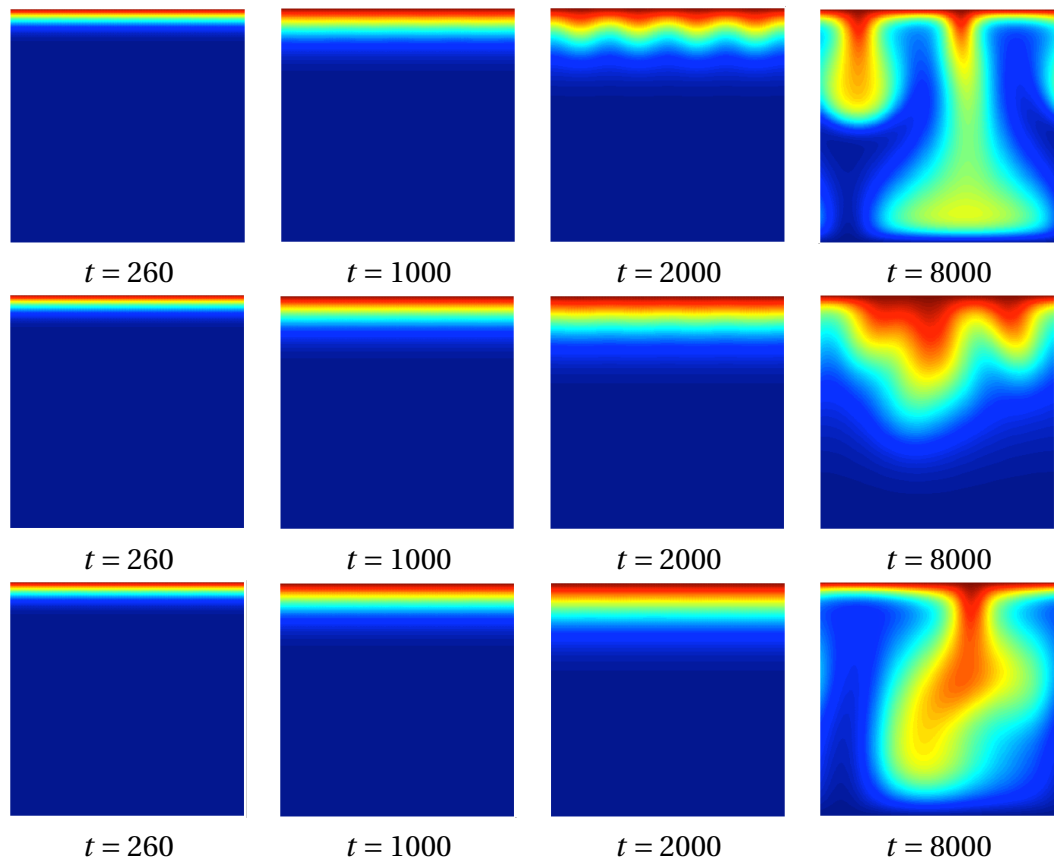


Figure 38: Time evolution of the concentration from the base state at $t = 252$ and mode 4 with initial amplitudes $a = 2 \times 10^{-4}$, $a = 2 \times 10^{-5}$ and $a = 2 \times 10^{-6}$ (see Eq. 4.7).

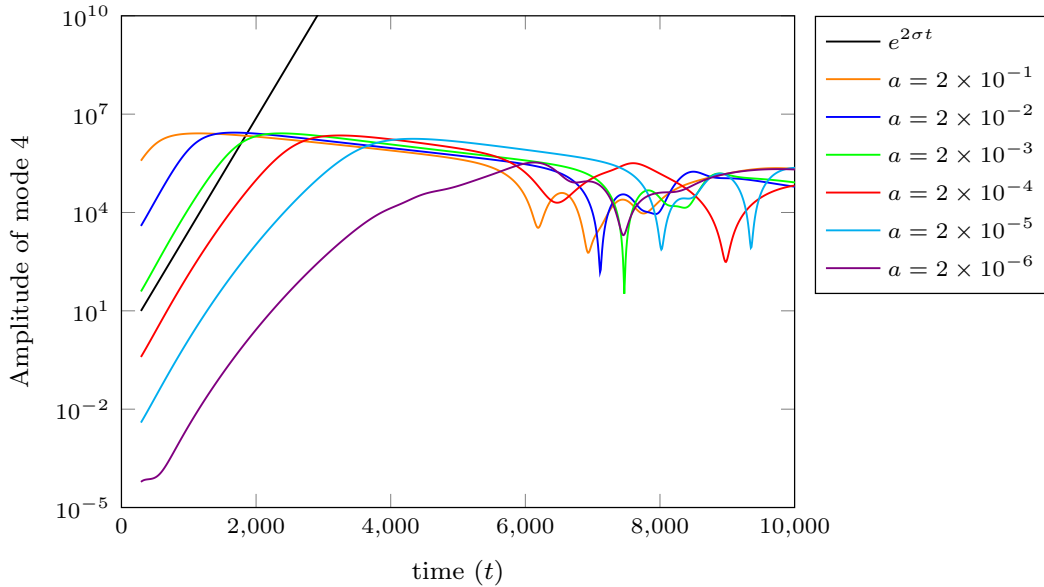


Figure 39: Long term evolution of mode 4 starting from initial conditions consisting of the base state at $t_0 = 252$ plus mode 4 with six initial amplitudes a (see Eq. 4.7). In black: growth of the amplitude of mode 4 as given by the LSA at $t_0 = 252$.

Eqs. 2.19 - 2.20 were solved numerically using Finite Element code with the material derivative represented by a semi-Lagrangian scheme. Tests conducted with different grid refinements showed that error in the evaluation of σ decreases with Δx for finer meshes and with $(\Delta x)^2$ for coarser ones. Upon freezing the base state we recover the same rate of growth obtained with the linear stability analysis, giving us a certain degree of confidence in the code.

We observed that when integrating the evolution equation starting from the base state plus a perturbation a minimum initial level of this one is required to obtain the linear growth of the linear stability analysis in the first stages of evolution. If this minimum is not included in the initial condition a deviation occurs at the first stages of the linear growth, due to noise introduced by the grid.

As we allow the base state to evolve we observe a certain deviation in the rate of growth of the amplitude of modes when comparing with σ obtained from the linear analysis, due to nonlinear effects.

5 CODE VERIFICATION AND GRID CONVERGENCE

Chapter 4 presents the results of the LSA performed as part of the validation process of the numerical code, written in Matlab. The numerical algorithms developed for this code were, subsequently, translated to the C programming language and included in a more robust code, written in this language.

This chapter presents the results of the tests performed to verify the behavior of the C numerical code developed as part of this thesis, and also, the procedure followed to select the numerical grid and the time step adopted in the numerical simulations.

5.1 Code verification

The code verification procedure consisted in solving the governing equations in the purely diffusive state, namely, for the case where Eq. 2.19 becomes $\nabla^2 \psi = 0$ at the upper flat interface, with boundary conditions $e = 1$ at the upper boundary, $\mathbf{n} \cdot \nabla c = 0$ at the bottom and periodic at the sidewalls. Figure 40 and Figure 41 show the system evolution in two different times, obtained by numerical integration of the governing equations, the analytical solution, and the absolute error, defined as the absolute difference between the two solutions.

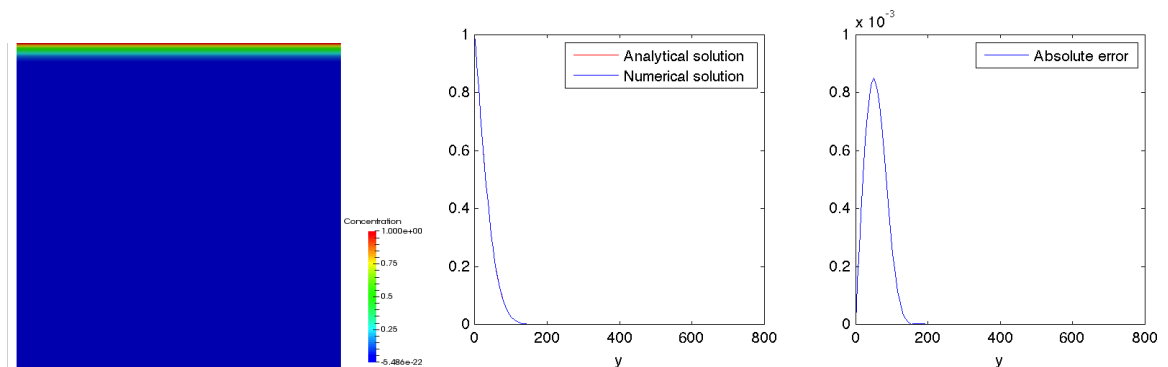


Figure 40: Left: the system state at $t = 1000$. At the center: the analytical solution. At right: the absolute error, defined as the difference between both solutions at $t = 1000$.

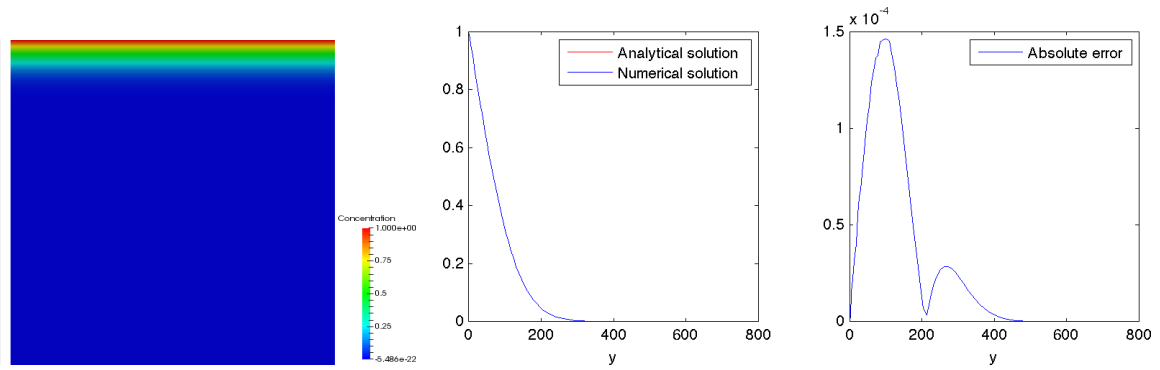


Figure 41: Left: the system state at $t = 5000$. At the center: the analytical solution. At right: the absolute error, defined as the difference between both solutions at $t = 5000$.

The system and numerical parameters adopted in the runs performed for the verifications leading to the results presented in Figure 40 and Figure 41 are:

- Domain dimensions: $L_x = 1600$ and $L_y = 1600$.
- Numerical grid: 150×120 grid points.
- Time step: $dt = 5.0$.

The results confirm the consistence of implementation of the boundary conditions, verifying thus the consistence of the code written in C, with functions of the PETSc library.

5.2 Results with flat interface

Following the code verification process we applied the characterization figures defined in Section 3.5 to the results of a simulation (see Figure 42 to Figure 46) run in a small domain with the following parameters:

Domain dimensions: $L_x = 2000$ and $L_y = 2000$.

Numerical grid: 401×401 grid points.

Initial and final times: $t_0 = 0$ and $t_f = 20000$, respectively.

CPU run time: *1h20min*.

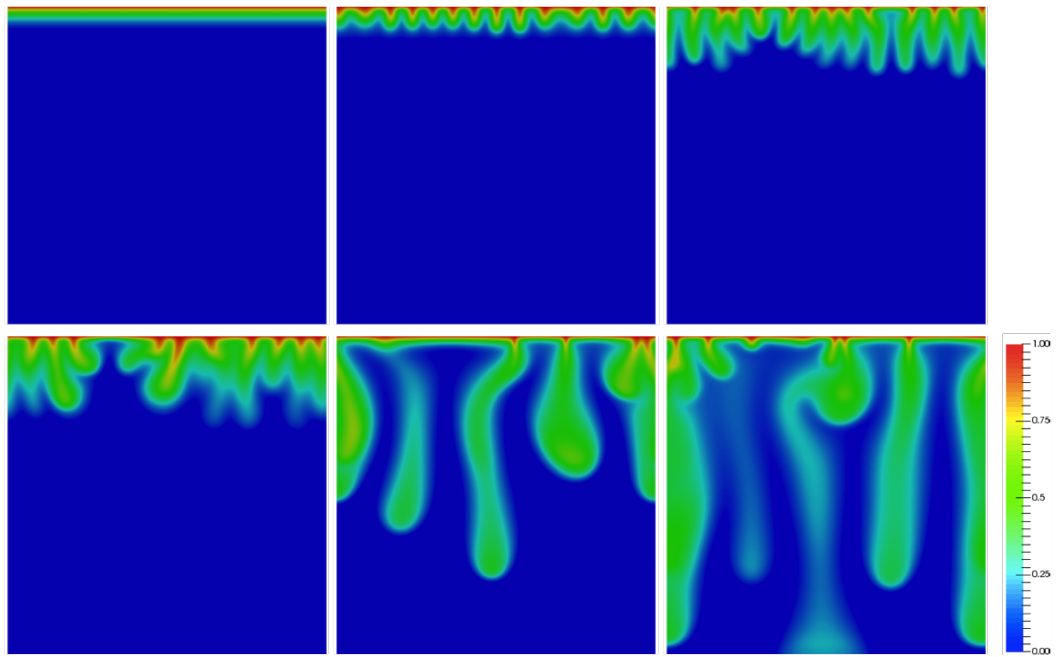


Figure 42: System state at $t = 2500, 5000, 7500, 10000, 15000$ and 20000 , respectively.

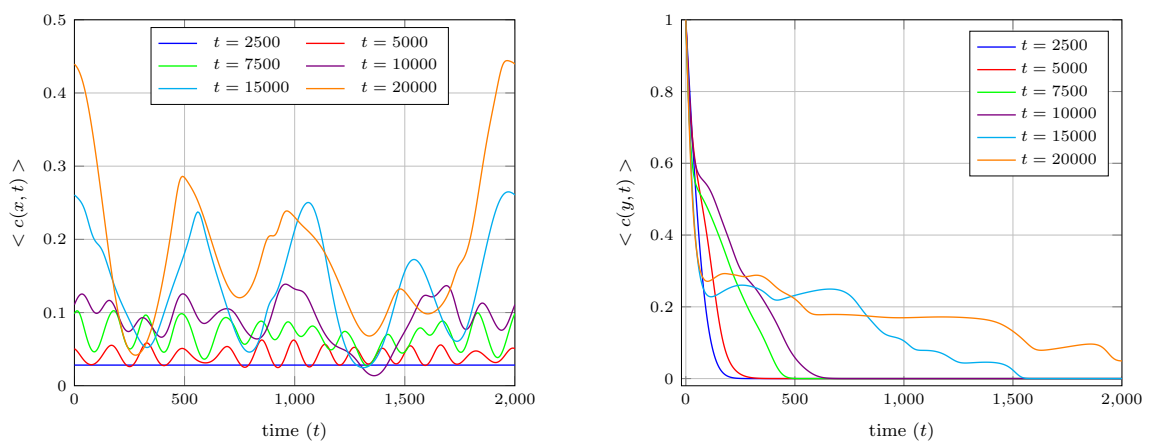


Figure 43: Left: average concentration longitudinal profile: $\langle c(x, t) \rangle$. Right: average concentration transverse profile: $\langle c(y, t) \rangle$.

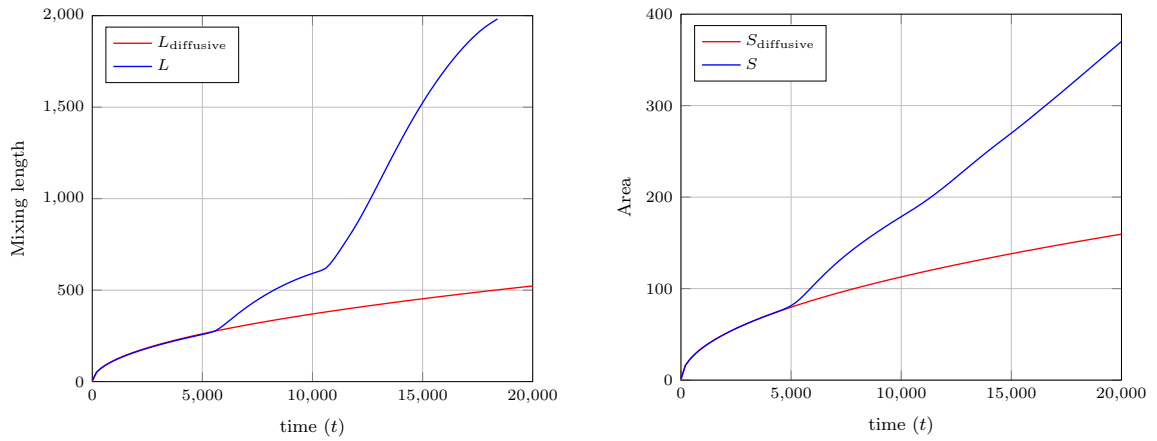


Figure 44: Left: evolution of the fingers length. Right: evolution of fingers area.

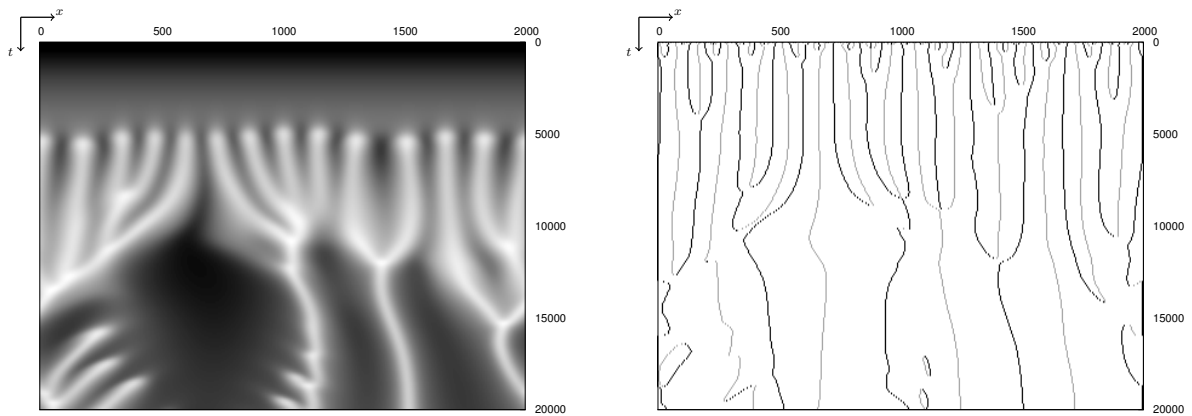


Figure 45: Left: space-time chart at a prescribed distance of the interface - $\Delta y' = 100$. Right: position of the fingers maximum and minimum.

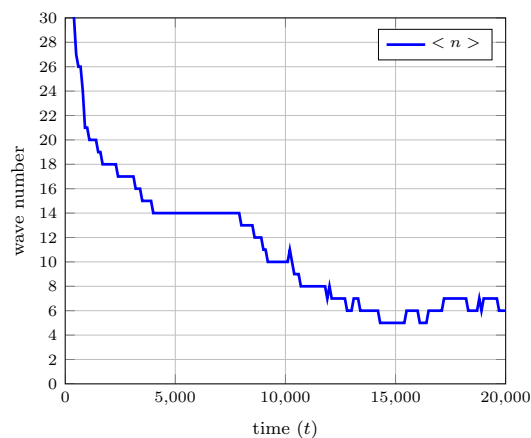


Figure 46: Average number of wavelengths.

The above results qualitatively match the existing results found in the literature [45] and contribute for the validation of the code developed in the framework of this thesis.

5.3 Grid convergence

Following the code validation process, as above described, we proceeded addressing the grid spacing Δx and Δy , along the two directions, and also, the optimum time step Δt , for the simulations performed. It is worth to mention that the thin boundary layer at the interface between the two fluids recommends the use of variable Δy in order to better capture the dynamics within the boundary layer. We adopted an exponentially growing Δy .

Five computational runs were made with different values of Δx , Δt and random initial conditions. The domain dimensions were defined as $L_x = 1000$ and $L_y = 2000$, and the integration was made in the time interval $t_0 = 0$ to $t_f = 20.000$.

Tests performed with $\Delta x = 10.0$:

We adopted a computational grid with 101×201 points in this series of runs. Table 3 presents the average number of fingers and the associated times, of each group comprising five simulations.

Table 3: Effect of the selected time step Δt and of the time of evolution on the number of fingers in the domain.

Δt	fingers (\approx)	CPU time
5.00	7	6min
2.50	7	11min
1.25	7	20min

Figure 47 shows the mixing length for the 15 runs with $\Delta t = 5.0$, 2.5 and 1.25 and random initial conditions. Blue curves refer to tests with $\Delta t = 5.0$, red curves, to $\Delta t = 2.5$, green curves, to $\Delta t = 1.25$. Dashed curves refer to the average of runs performed with each of the above Δt .

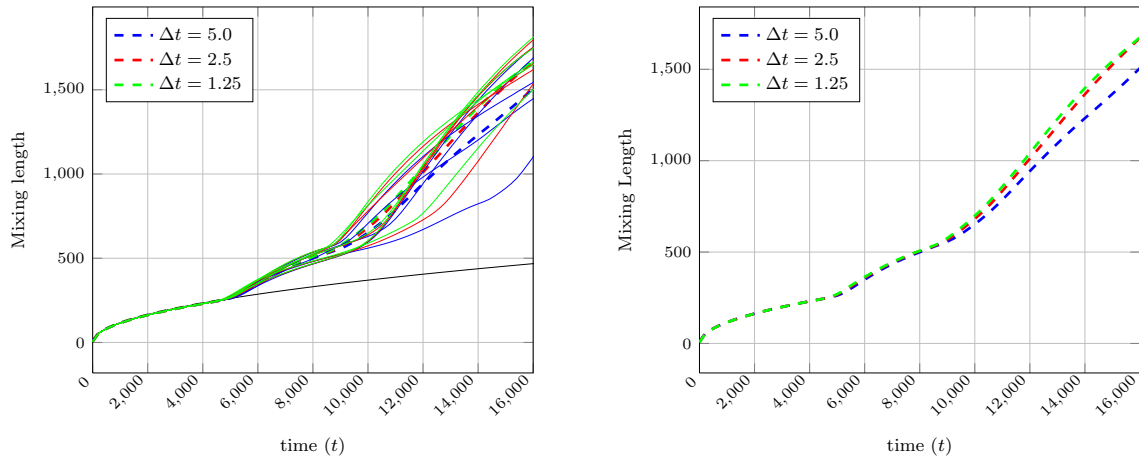


Figure 47: Left: evolution of the mixing length of the fingers. Right: average mixing length of the tests for each Δt .

Tests performed with $\Delta x = 5.0$:

For this series, we adopted a numerical grid with 201×401 points. Table 4 presents the average number of fingers and the associated times, of each group comprising five simulations.

Table 4: Effect of the selected time step Δt and of the time of evolution on the number of fingers in the domain.

Δt	fingers (\approx)	CPU time
5.00	6	30min
2.50	6	50min
1.25	6	1h15min

Figure 48 shows the mixing length for the 15 runs with $\Delta t = 5.0$, 2.5 and 1.25 and random initial conditions. Blue curves refer to tests with $\Delta t = 5.0$, red curves, to $\Delta t = 2.5$, green curves, to $\Delta t = 1.25$. Dashed curves refer to the average of runs performed with each of the above Δt .

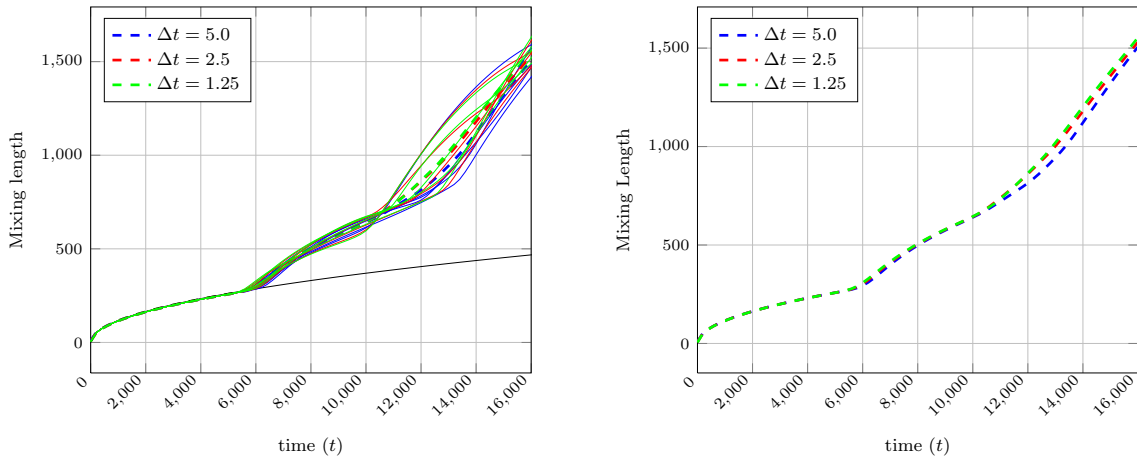


Figure 48: Left: evolution of the mixing length of the fingers. Right: average mixing length of the tests for each Δt .

Tests performed with $\Delta x = 2.5$:

The computational grid: 401×801 points. Table 5 presents the average number of fingers and the associated times, of each group comprising five simulations.

Table 5: Effect of the selected time step Δt and of the time of evolution on the number of fingers in the domain.

Δt	fingers (\approx)	CPU time
2.50	6	6h
1.25	7	9h
0.625	7	16h

Figure 49 shows the mixing length for the 15 runs with $\Delta t = 2.5$, 1.25 and 0.625 and random initial conditions. Blue curves refer to tests with $\Delta t = 2.5$, red curves, to $\Delta t = 1.25$, green curves, to $\Delta t = 0.625$. Dashed curves refer to the average of runs performed with each of the above Δt .

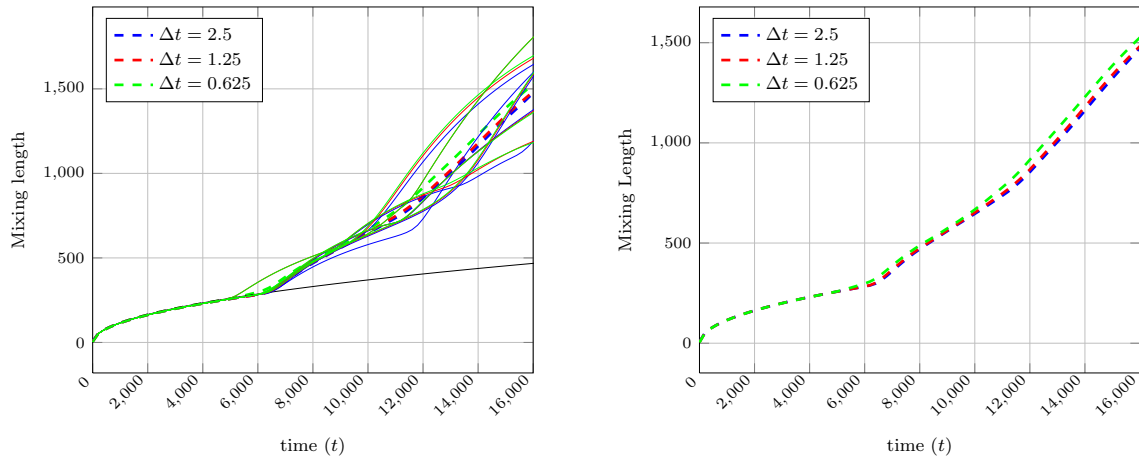


Figure 49: Left: evolution of the mixing length of the fingers. Right: average mixing length of the tests for each Δt .

Figure 50 shows all the average mixing lengths obtained in the 15 tests performed (see Figure 47 to Figure 49).

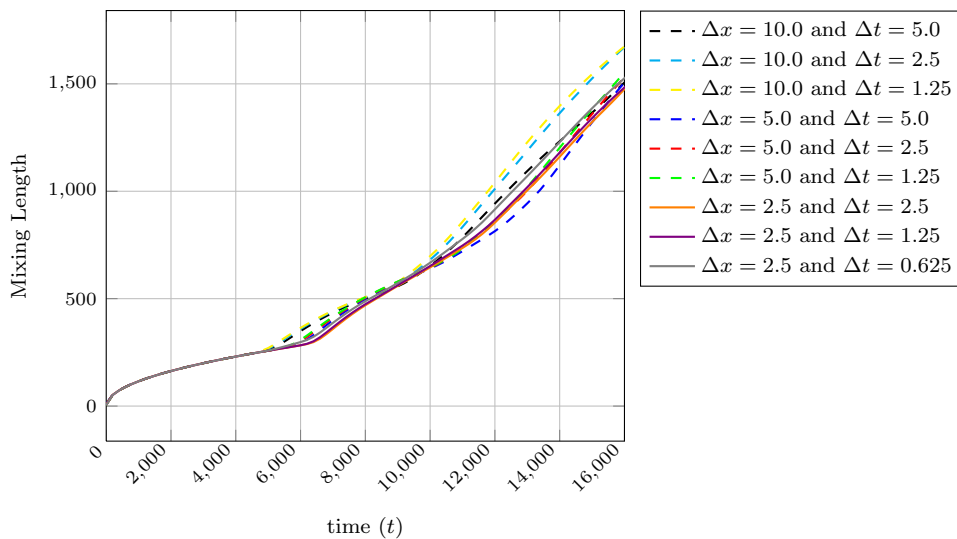


Figure 50: Comparison between average mixing lengths obtained in the tests performed as above, with three values of Δx and Δt .

An inspection of Figure 50, and of Table 3-Table 5 leads to the conclusion that $\Delta x = 5.0$, with time step $\Delta t = 2.5$ are the optimum values for our simulations. In what concerns to the vertical spacing we assumed an exponential growth along the y direction, ranging from $\Delta y = 2.5$ to $\Delta y = 7.5$ at the domain bottom.

5.4 Choosing the integration domain

The choice of a suitable domain of integration is of utmost importance to reproduce existing results and to assure that we obtain qualitatively and quantitatively sound new results, that mimic the behavior of real systems ([8], [27]). Accordingly, we performed tests with flat interface and several domain dimensions L_x e L_y , and present the results of two of them. Sections 5.4.1 and 5.4.2 summarize the results of tests performed with different domains, selected among the conducted ones.

5.4.1 Flat interface

This section presents the results of two of our tests, performed in domains with same horizontal length and different depths.

The results of the first simulation are shown in Figure 51 to Figure 55. These results were obtained in a run where we assumed $L_y = 6000$, and the following parameters:

Domain dimensions: $L_x = 4000$ and $L_y = 6000$.

Numerical grid: 801×1201 grid points.

Initial and final times: $t_0 = 0$ and $t_f = 50000$, respectively.

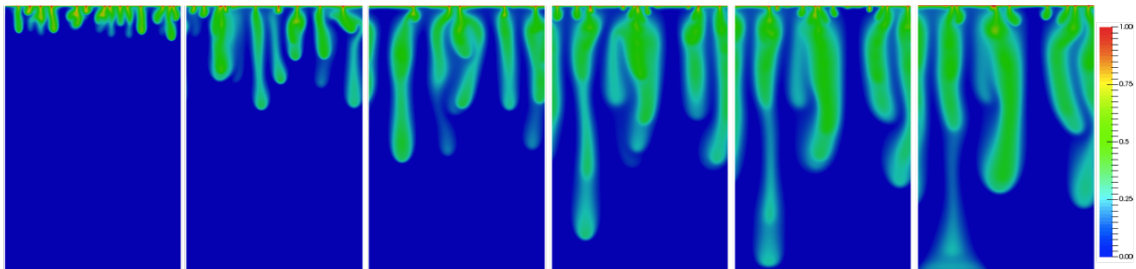


Figure 51: Time evolution frames, at times: $t = 10000, 20000, 30000, 40000, 45000$ and 50000 , from left to right.

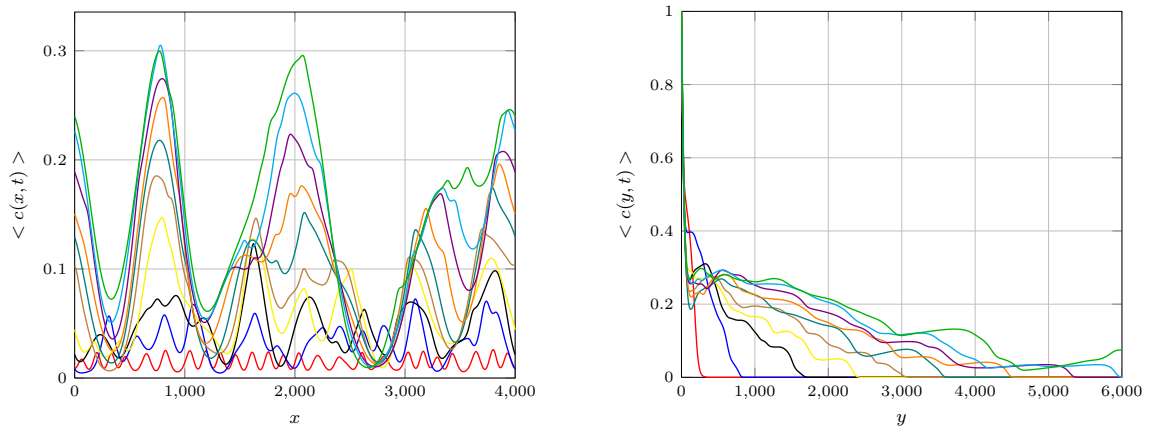


Figure 52: Left: average concentration longitudinal profile: $\langle c(x, t) \rangle$. Right: average concentration transverse profile: $\langle c(y, t) \rangle$. The time interval between two successive curves is $\Delta t' = 5000$, the first curve is in $t = 5000$.

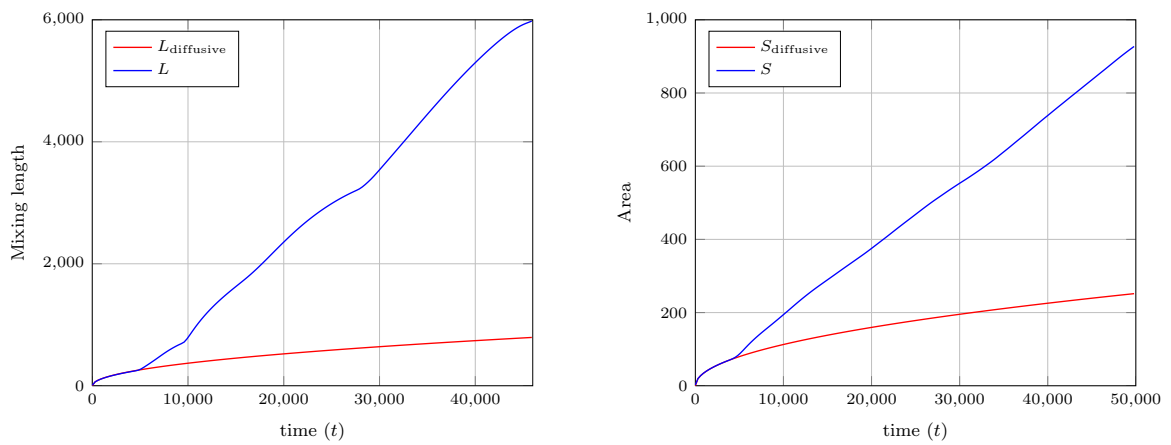


Figure 53: Mixing length (left), and finger area (right).

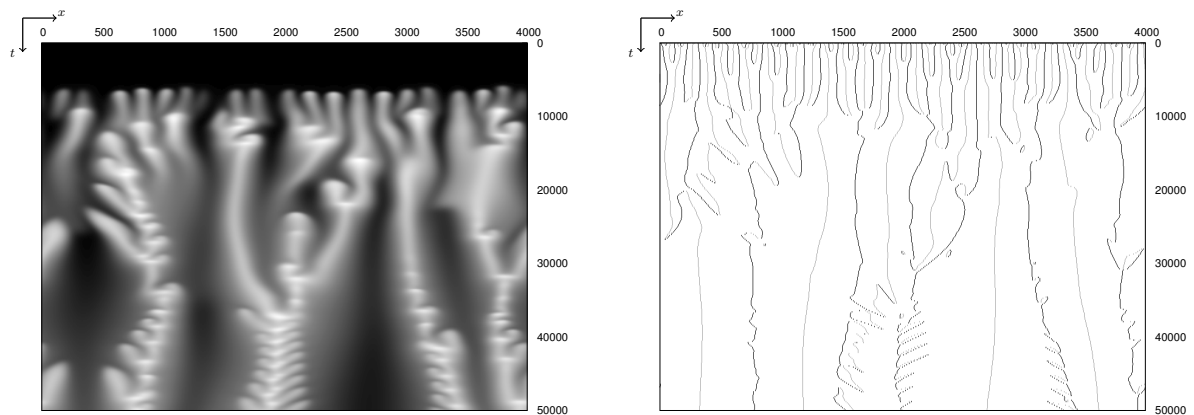


Figure 54: Space-time map with $\Delta y' = 300$ from the top (left), and position of fingers maximum and minimum (right).

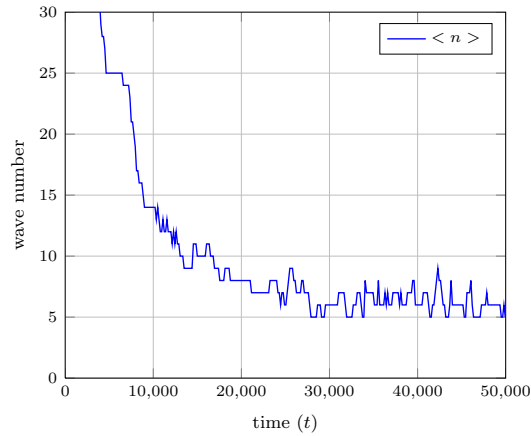


Figure 55: Average wavelength.

The second series of runs was performed in systems with domain depth $L_y = 12000$, and the following parameters:

Domain dimensions: $L_x = 4000$ and $L_y = 12000$.

Numerical grid: 801×2401 grid points.

Initial and final times: $t_0 = 0$ and $t_f = 120000$, respectively.

The results of the second simulation are shown in Figure 56 to Figure 60. We obtained the following results:

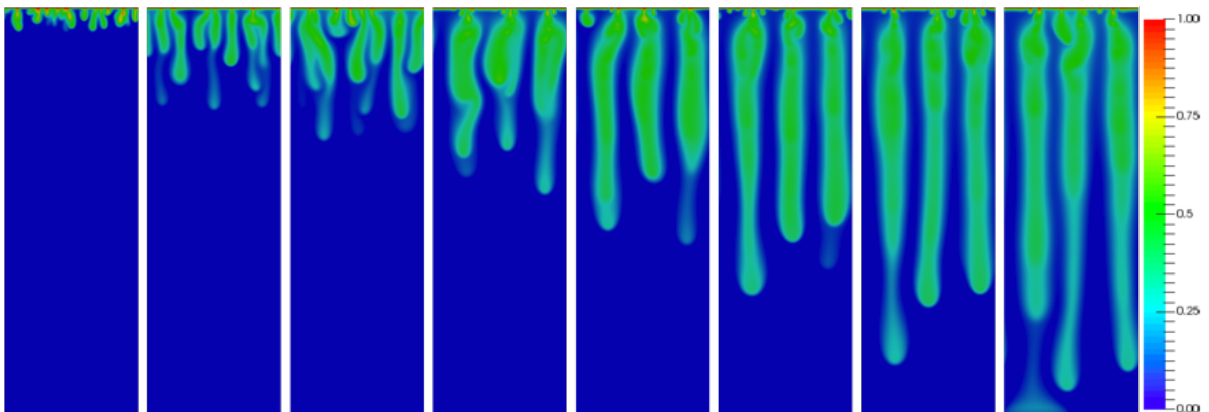


Figure 56: Time evolution frames, at times: $t = 10000, 25000, 40000, 55000, 70000, 85000, 100000$ and 120000 , from left to right.

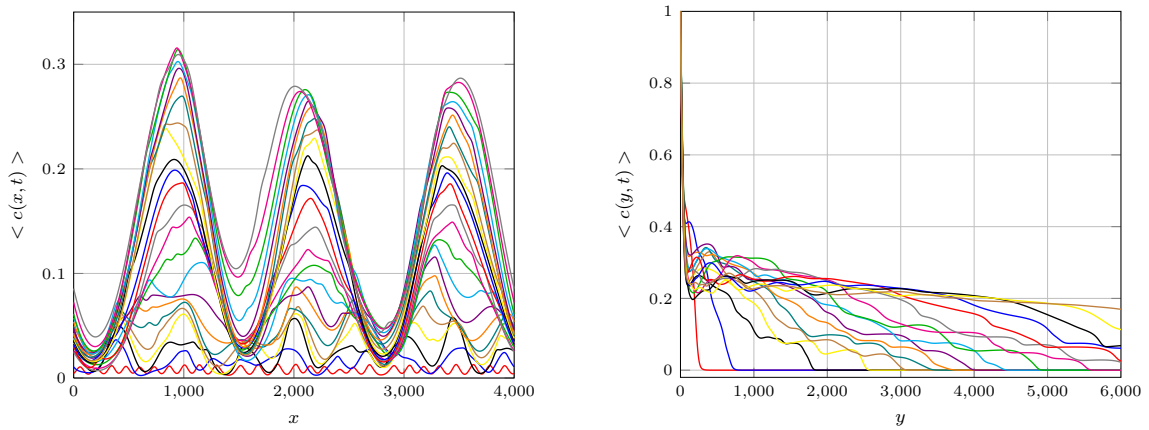


Figure 57: Left: average concentration longitudinal profile: $\langle c(x, t) \rangle$. Right: average concentration transverse profile: $\langle c(y, t) \rangle$. The time interval between two successive curves is $\Delta t' = 5000$, the first curve is in $t = 5000$.

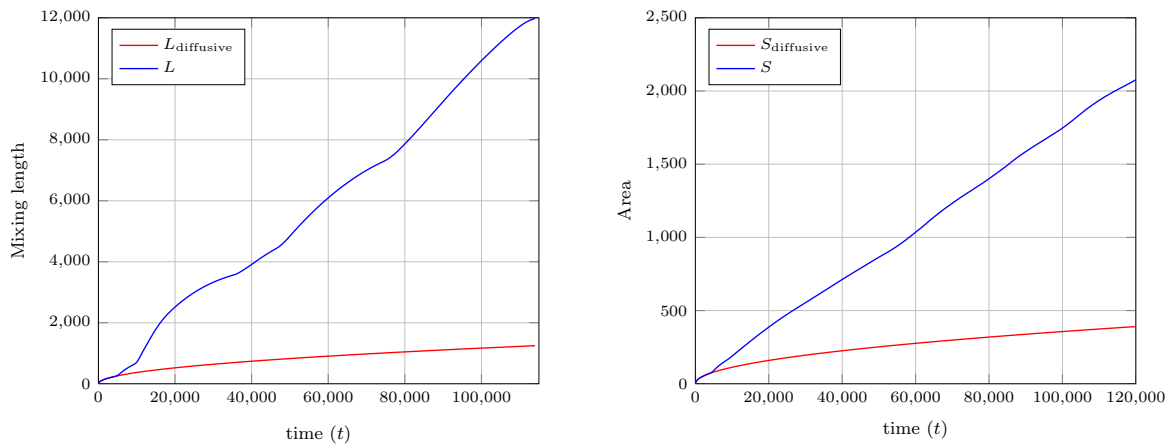


Figure 58: Mixing length (left), and finger area (right).

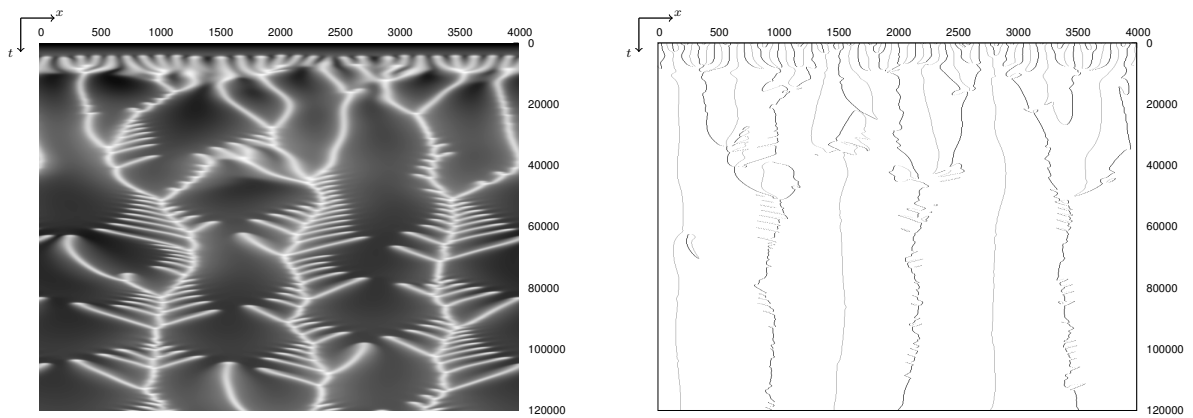


Figure 59: Space-time map with $\Delta y' = 120$ from the top (left), and position of fingers maximum and minimum (right).

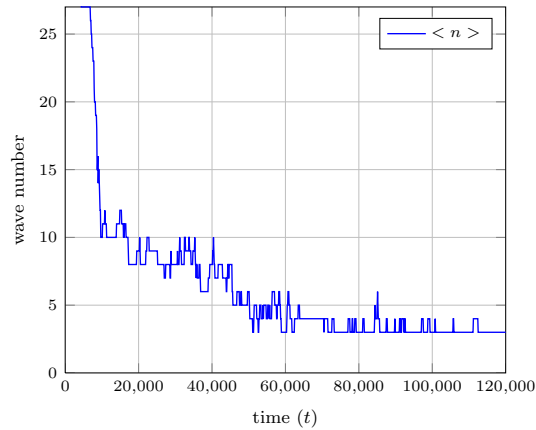


Figure 60: Average number of fingers.

From Figure 51 to Figure 60 we conclude that the domain depth L_y affect the elapsed time between the beginning of the dissolution process and the time in which fingers reach the domain bottom. We also infer that deeper domains favour the development of larger number of fingers close to the boundary layer (see Figure 54 and Figure 59, left).

5.4.2 Deformed interface

Two series of runs were performed with deformed interface, assuming an amplitude of deformation $A = 600$, same domain length in the two cases, and two different depths.

The first series of runs was done assuming $L_y = 6600$ and the following parameters:

Domain dimensions: $L_x = 4000$ and $L_y = 6600$.

Numerical grid: 801×1201 grid points.

Initial and final times: $t_0 = 0$ and $t_f = 45000$, respectively,

Figure 61 and Figure 65 present the results for one initial condition.

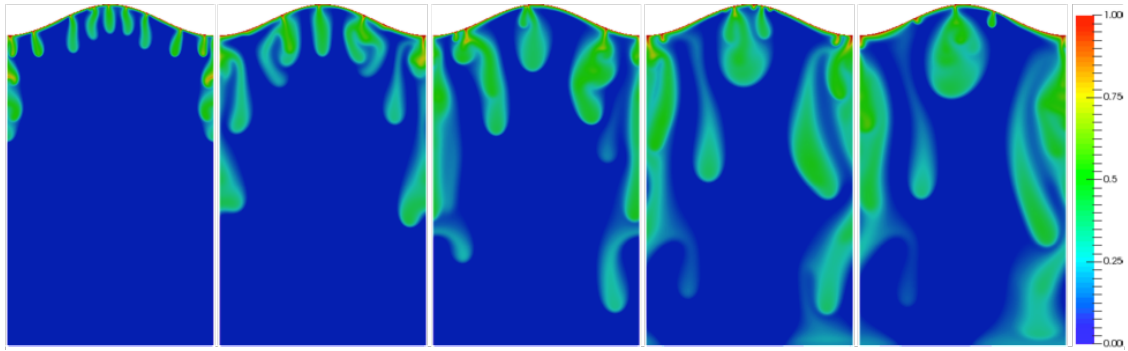


Figure 61: Time evolution frames, at times: $t = 10000, 20000, 30000, 40000$ and 45000 , from left to right.

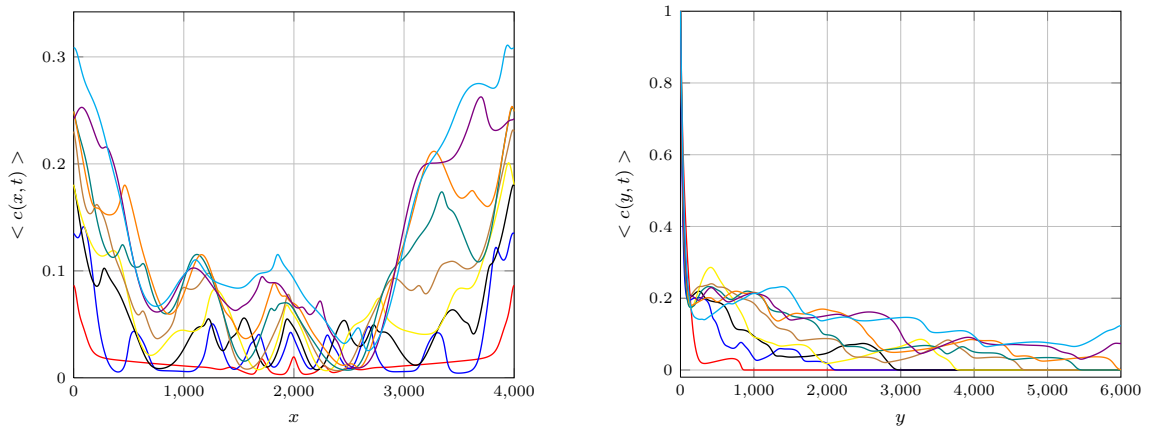


Figure 62: Left: average concentration longitudinal profile, $\langle c(x, t) \rangle$. Right: average concentration transverse profile, $\langle c(y, t) \rangle$. The time interval between two successive curves is $\Delta t' = 5000$, the first curve is in $t = 5000$.

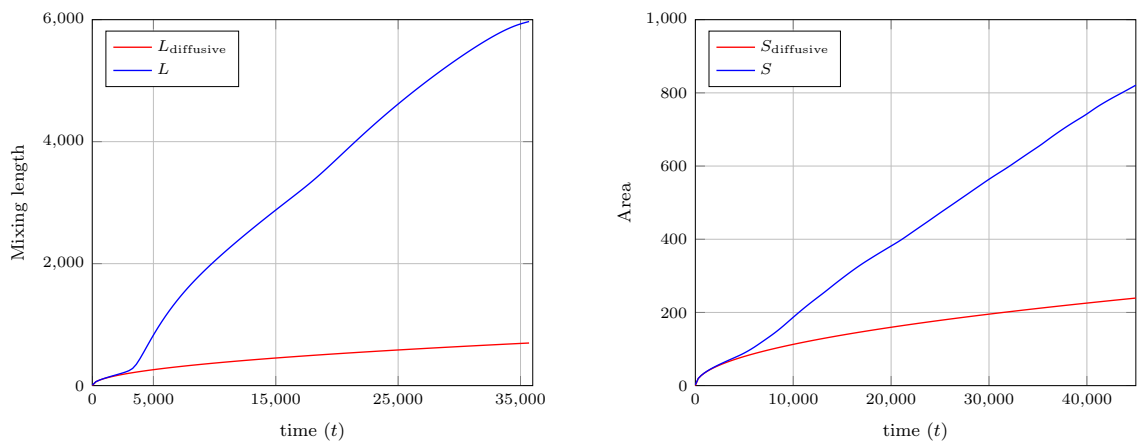


Figure 63: Mixing length (left), and finger area (right).

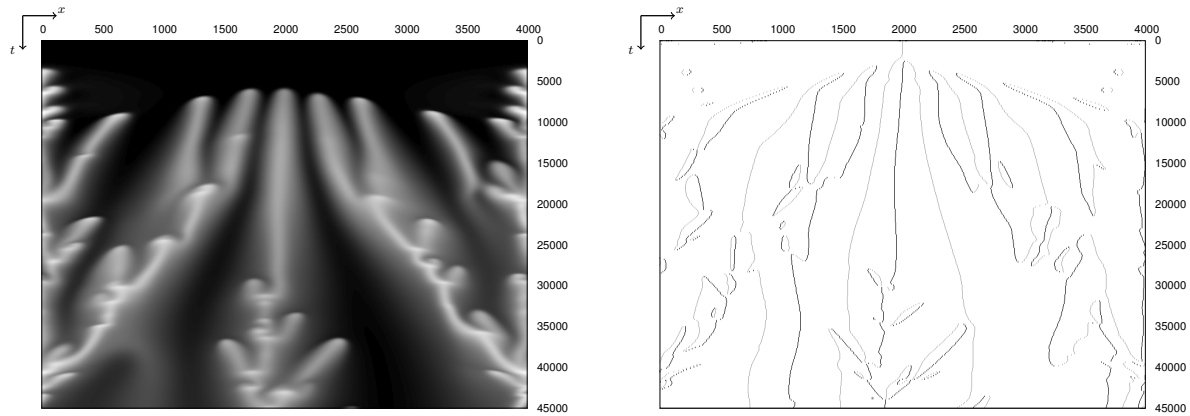


Figure 64: Space-time map with $\Delta y' = 300$ from the top (left), and position of fingers maximum and minimum (right).

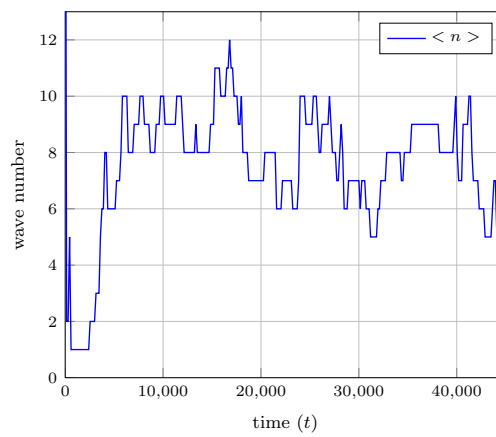


Figure 65: Average number of fingers.

The second series of runs with deformed interface ($A = 600$), was made in a system with domain depth $L_y = 12600$, and the following parameters:

Domain dimensions: $L_x = 4000$ and $L_y = 12600$.

Numerical grid: 801×2401 grid points.

Initial and final times: $t_0 = 0$ and $t_f = 85000$, respectively.

The results are presented in Figure 66 to Figure 70:

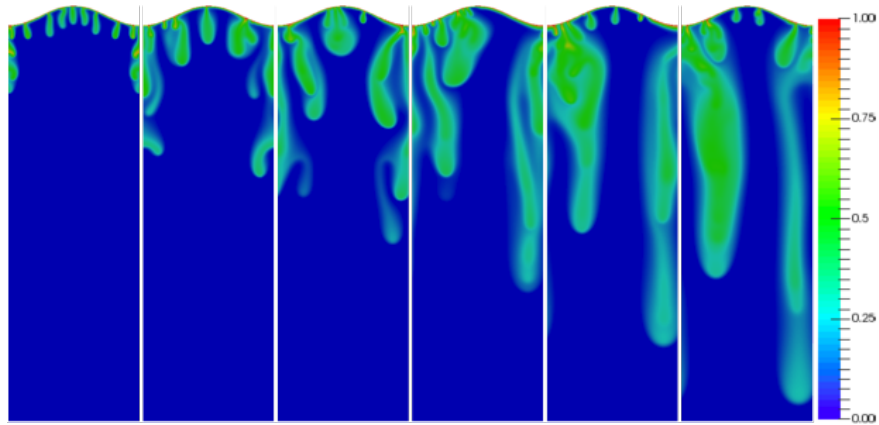


Figure 66: Time evolution frames, at times: $t = 10000, 25000, 40000, 55000, 70000$ and 85000 , from left to right.

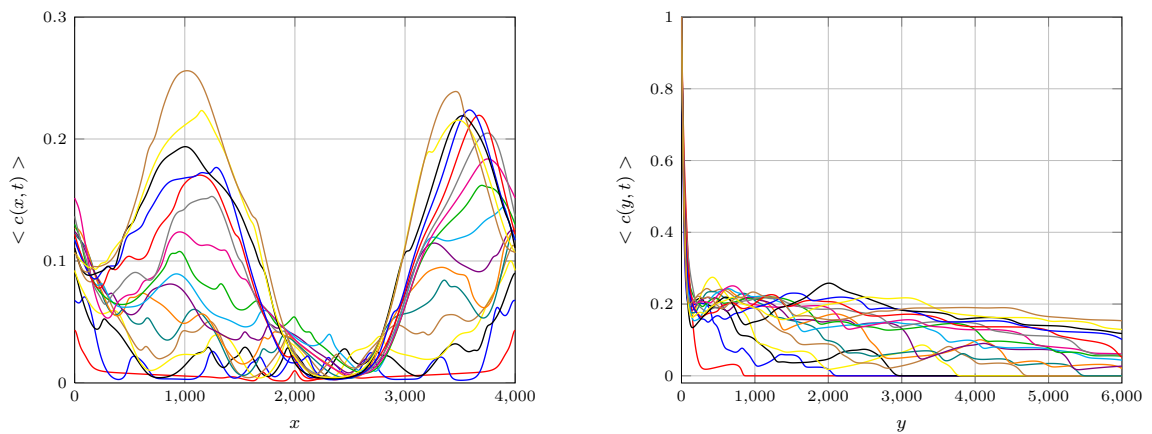


Figure 67: Left: average concentration longitudinal profile: $\langle c(x, t) \rangle$. Right: average concentration transverse profile: $\langle c(y, t) \rangle$. The time interval between two successive curves is $\Delta t' = 5000$, the first curve is in $t = 5000$.

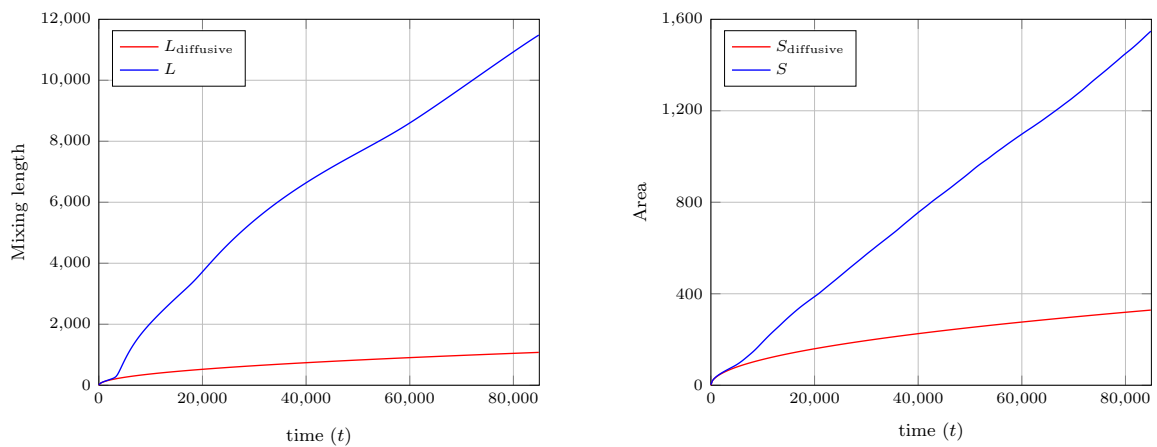


Figure 68: Mixing length (left), and finger area (right).

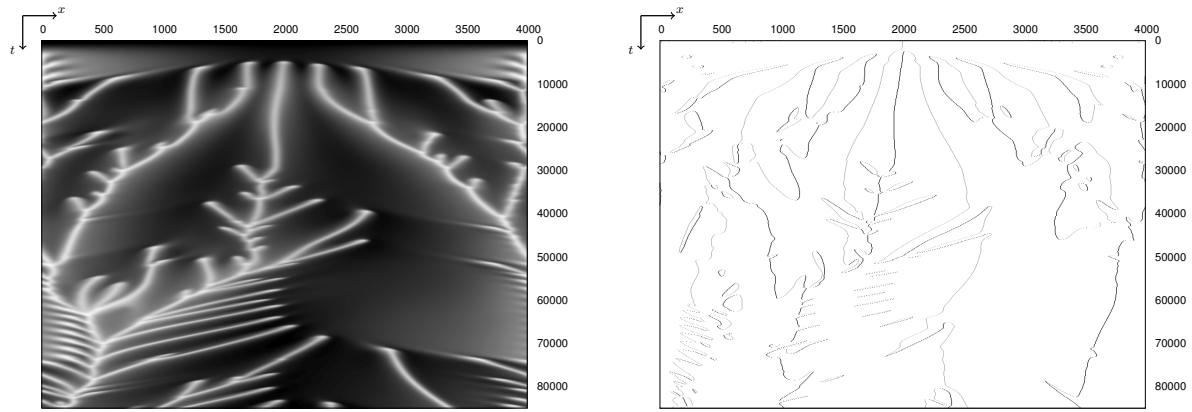


Figure 69: Space-time map with $\Delta y' = 120$ from the top (left), and position of fingers maximum and minimum (right).

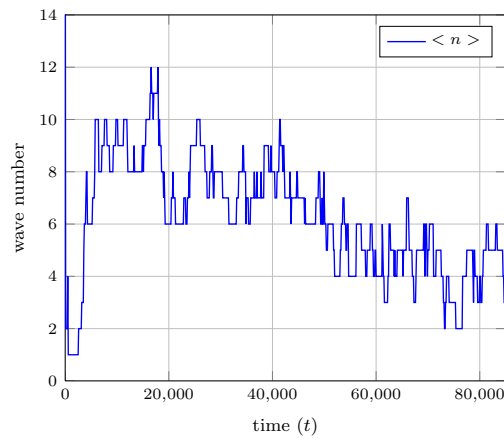


Figure 70: Average number of fingers.

As in the case of flat interfaces, the results obtained with deformed ones show that deeper domains result in more complex structure of patterns. The point becomes clear when we compare Figure 54 and Figure 59 with Figure 64 and Figure 69.

From the above results, we conclude that a suitable domain for integration of the governing equations is the one with the fastest evolution, and featuring effects like the merge an thickening of fingers, and new instabilities. Among the domains and parameters used in the above tests, the set that better matches the above desired characteristics is the one defined by $L_x = 4000$ and $L_y = 12000 + A$, where A is the amplitude of the interface deformation.

6 NUMERICAL RESULTS

This chapter deals with the numerical results obtained with simulations of the problem in configurations with prescribed fixed upper interface deformations. Numerical integration of the governing equations (Eqs. 2.19 and 2.20) were performed over a physical domain defined by: $L_x = 4000 \times 12000 + A$, (A standing for the amplitude of the interface deformation).

A numerical mesh containing $n_{el} = 2(n_x - 1)(n_y - 1) = 3,840,000$ triangular elements was adopted, with $n_x = 801$ and $n_y = 2401$, where n_x and n_y are, respectively, the number of points along the x and y directions. The time step adopted to advance time was $\Delta t = 2.5$. The same time interval was adopted in all simulations, and this time was selected as the one at which a first finger reaches the domain bottom, in simulations with flat interface. Simulations were performed in domains with flat and four deformed interfaces, $A = 0, 300, 600, 900$ and 1200 .

Figure 71 to Figure 75 present an overall picture of the dynamic evolution of the system, as obtained in our simulations. We can see the dynamics of density fingering in different times of the deformed gas/brine interface and the space-time map, respectively. As mentioned in Chapter 2, the simulations were made under periodic boundary conditions, so Figure 72 to Figure 75 show the concave deformation of the interface. The sequence of frames with the time evolution shows a flow towards the lower part of the deformation and the onset of the first finger at that point.

Figure 71 to Figure 75 also contain, at left, the space-time chart associated to the simulation. This chart consists of a plot of the time evolution of the concentration distribution at a prescribed distance of the interface, just below the interface boundary layer. Concentration is plotted along the horizontal axis of the figure, and time, along the vertical one, increasing from $t = t_0 = 0$ at the top, to $t_{\text{end}} = 95000$ at the bottom. The figure shows the successive onset of fingers in the boundary layer, and the merge of developed ones.

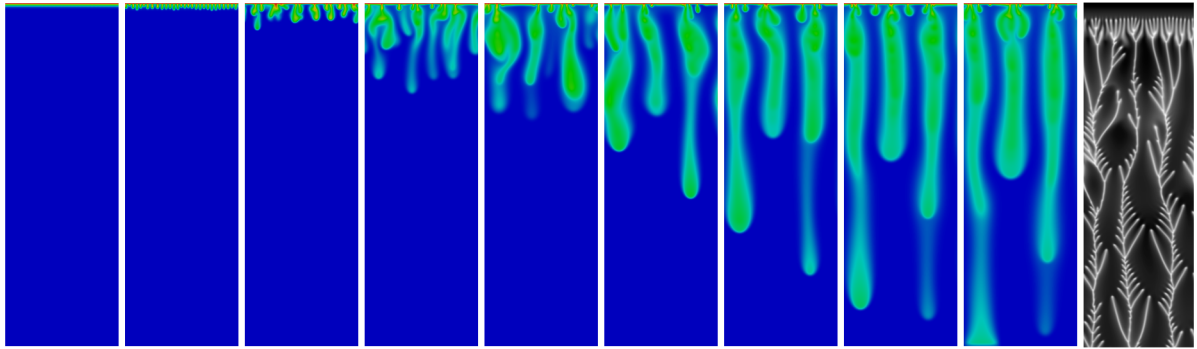


Figure 71: Time evolution of the case with $A = 0$, in times: $t = 3000, 5000, 10000, 25000, 40000, 55000, 70000, 85000$ and 95000 and the associated space-time chart evaluated at a distance $\Delta y' = 120$ of the flat interface.

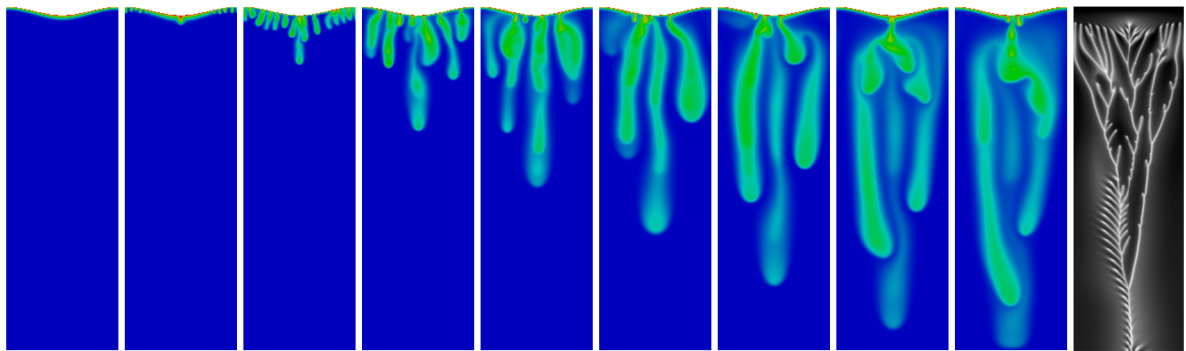


Figure 72: Time evolution of the case with $A = 300$, in times: $t = 3000, 5000, 10000, 25000, 40000, 55000, 70000, 85000$ and 95000 and the associated space-time chart evaluated at a distance $\Delta y' = 120$ of the deformed interface.

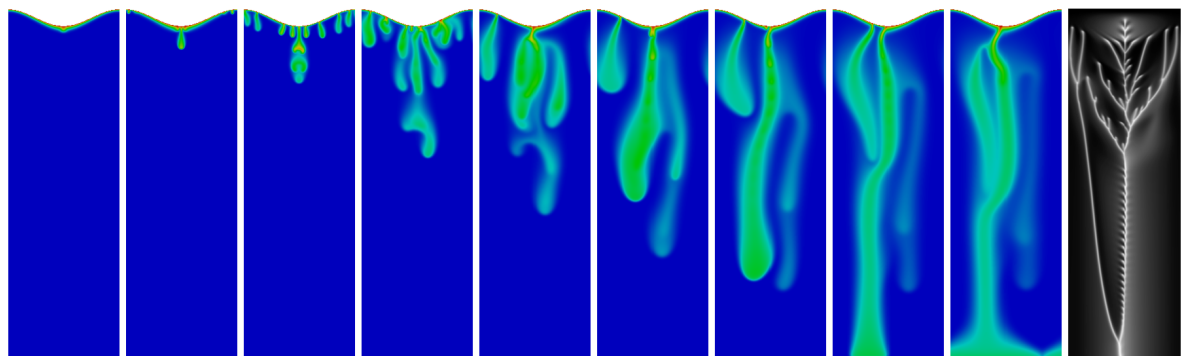


Figure 73: Time evolution of the case with $A = 600$, in times: $t = 3000, 5000, 10000, 25000, 40000, 55000, 70000, 85000$ and 95000 and the associated space-time chart evaluated at a distance $\Delta y' = 120$ of the deformed interface.

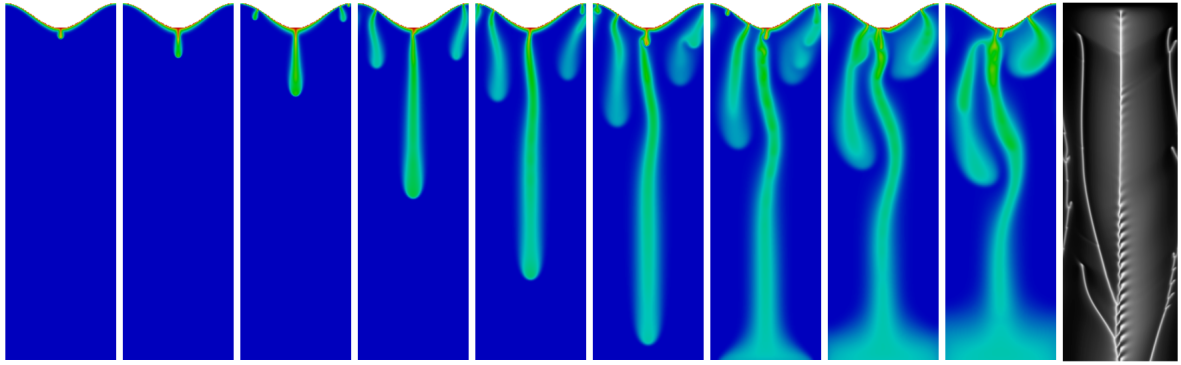


Figure 74: Time evolution of the case with $A = 900$, in times: $t = 3000, 5000, 10000, 25000, 40000, 55000, 70000, 85000$ and 95000 and the associated space-time chart evaluated at a distance $\Delta y' = 120$ of the deformed interface.

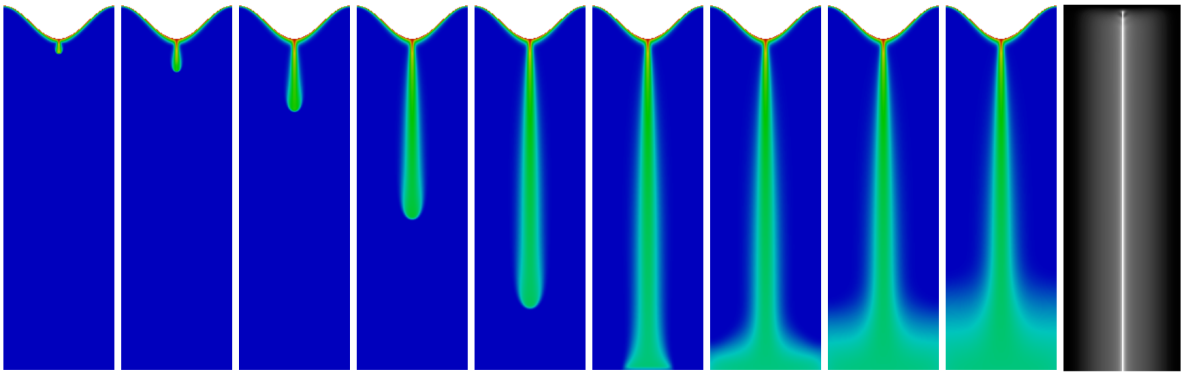


Figure 75: Time evolution of the case with $A = 1200$, in times: $t = 3000, 5000, 10000, 25000, 40000, 55000, 70000, 85000$ e 95000 and the associated space-time chart evaluated at a distance $\Delta y' = 120$ of the deformed interface.

The above figures show an onset of fingers evenly distributed along the flat interface at early times of evolution. However, a progressive thickening of three main fingers, to which new ones merge, is observed after $t = 40000$.

The merging process is enhanced in the deformed interfaces due to the drifting of the fingers caused by the inclination of the interface, as it is shown in Appendix B. This leads to a stronger coalescence process in the case of larger deformations.

In the cases with deformed upper interface $A = 300$ and $A = 600$, we see that the onset of new fingers at initial times decays, as the amplitude of the deformation increases. The evolution proceeds in a qualitative way close to the behavior of domains with flat interface after $t = 40000$, with the new ones merging the sole plume that survives directly below the lower point of the deformation. The configuration with $A = 900$ shows the onset of a single large finger just below the lower point of the deformation and two smaller ones that contribute

to the thickening of largest one. Only one finger develops at the lower point of the domain with the larger amplitude among the cases we addressed ($A = 1200$).

This is consistent with the inhibition of growth of perturbations observed in the case of large interface inclinations, as seen in Appendix B. In fact for $A = 1200$ fingers develop only at the extreme of the interface, which are the regions with smaller inclination, and the formation of fingers is suppressed on the inclined regions.

Figure 76(a) to Figure 80(a) show the average longitudinal $\langle c(x, t) \rangle$ at times $t = 5000, 10000, 25000, 40000, 55000, 70000,$ and 85000 , associated to the results presented in Figure 71 to Figure 75 for deformed interfaces with amplitudes $A = 0, 300, 600, 900$ and 1200 . These profiles show the time evolution of horizontal distribution of the concentration, where we can observe the onset, fusion and collapse of fingers.

Figure 76(b) to Figure 80(b) show the average transverse $\langle c(y, t) \rangle$ at times $t = 5000, 10000, 25000, 40000, 55000, 70000$ and 85000 , associated to the results presented in Figure 71 to Figure 75 for the cases of flat and deformed interfaces. The profiles give us a picture of the concentration along the vertical direction. In the diffusive regime we recover the analytical solution of this phase of the evolution, and the total amount of dissolved CO_2 in a layer located at a distance y , in the convective regime.

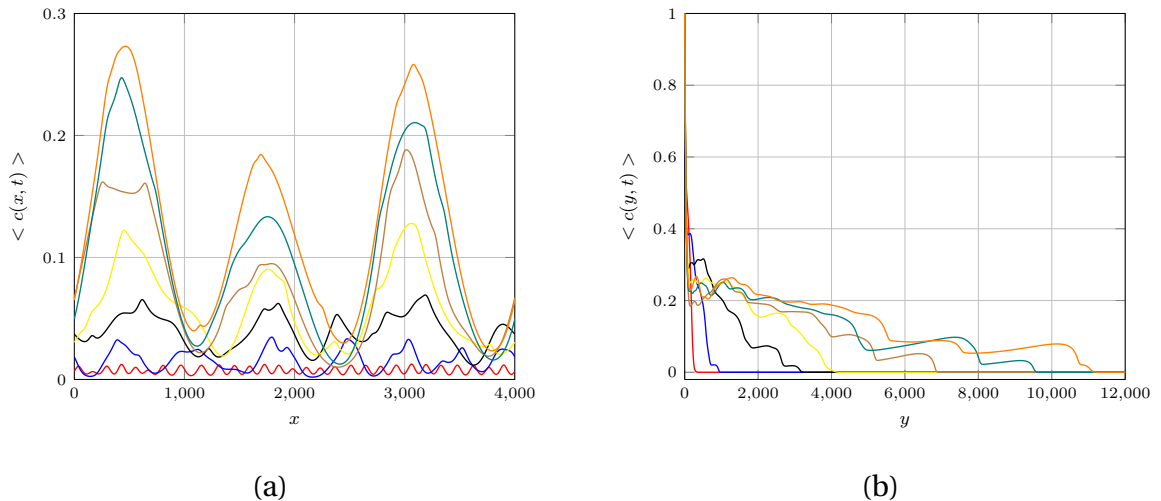


Figure 76: (a) Average concentration longitudinal profile, $\langle c(x, t) \rangle$; (b) average concentration transverse profile, $\langle c(y, t) \rangle$, both for with flat interface ($A = 0$).

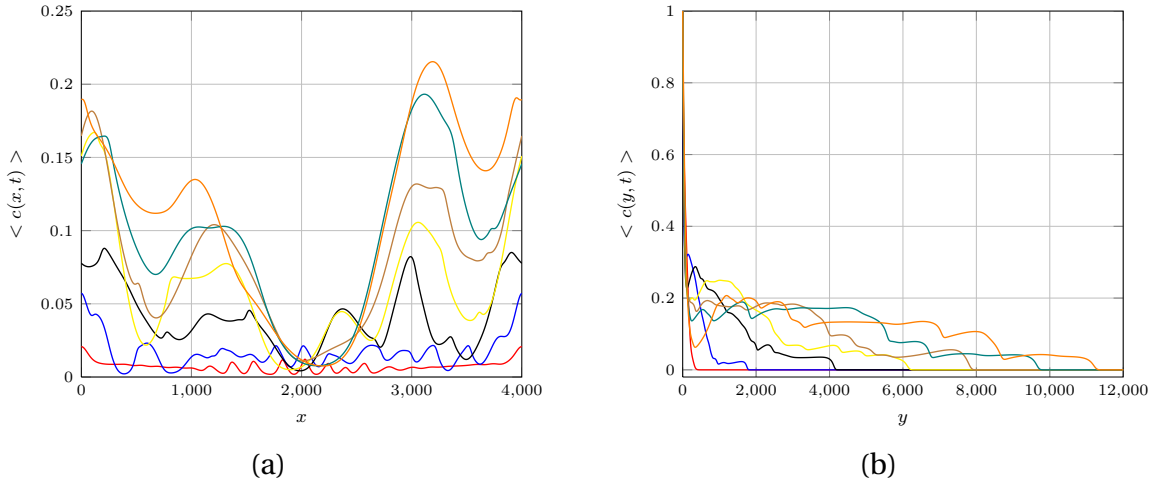


Figure 77: (a) Average concentration longitudinal profile, $\langle c(x, t) \rangle$; (b) average concentration transverse profile, $\langle c(y, t) \rangle$, both for deformed interface with $A = 300$.

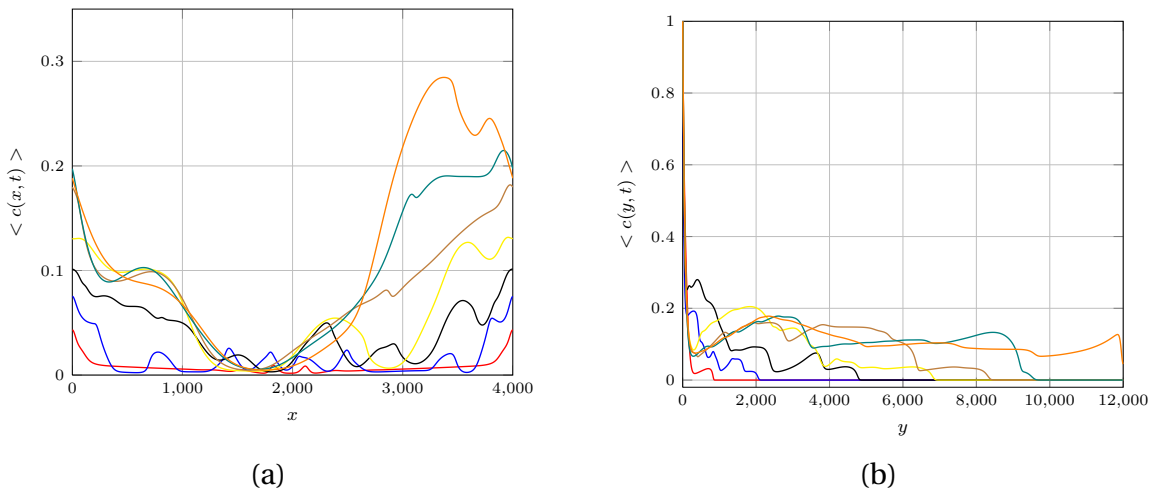


Figure 78: (a) Average concentration longitudinal profile, $\langle c(x, t) \rangle$; (b) average concentration transverse profile, $\langle c(y, t) \rangle$, both for deformed interface with $A = 600$.

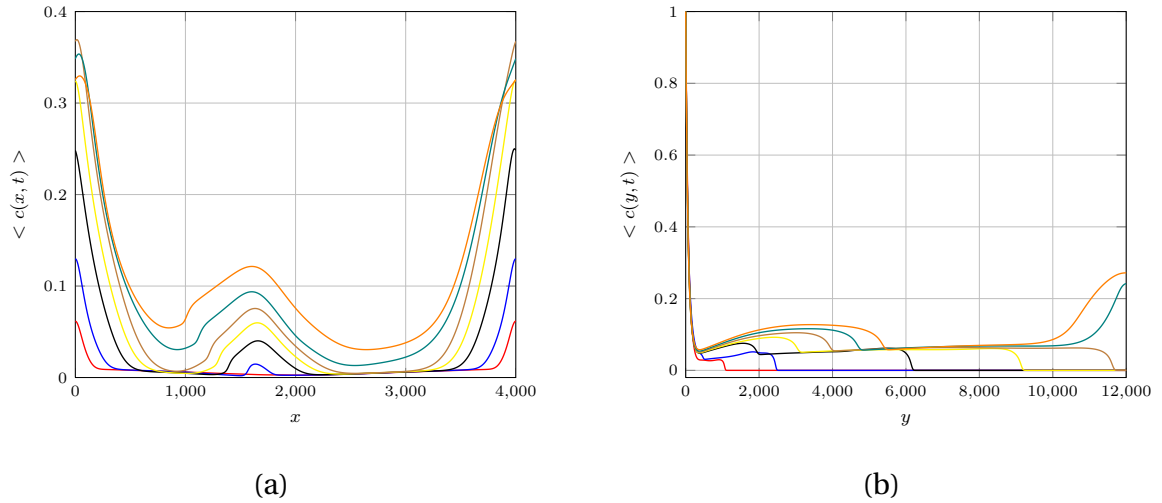


Figure 79: (a) Average concentration longitudinal profile, $\langle c(x, t) \rangle$; (b) average concentration transverse profile, $\langle c(y, t) \rangle$, both for deformed interface with $A = 900$.

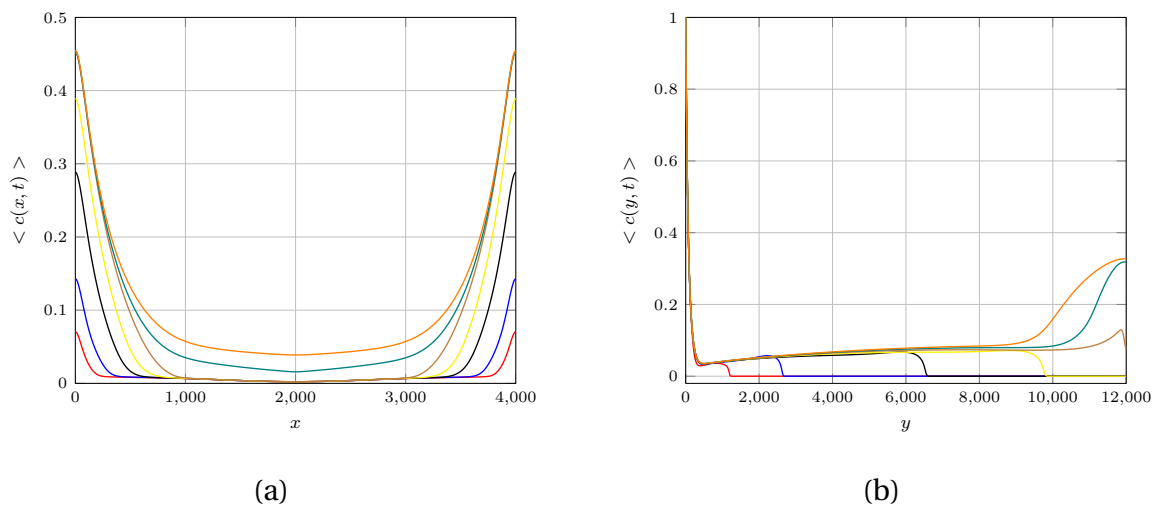


Figure 80: (a) Average concentration longitudinal profile, $\langle c(x, t) \rangle$; (b) average concentration transverse profile, $\langle c(y, t) \rangle$, both for deformed interface with $A = 1200$.

Figure 81 shows the mixing length for one flat and four deformed interfaces. Each curve presents the average mixing length of nine runs, made with different initial conditions. From this figure we conclude that larger interface deformations accelerate dissolution. This figure includes a zoom of the region close to the origin of the axis where we can see that the interface with larger deformation amplitude accelerates dissolution (Figure 82 to Figure 84 better explain the effect).

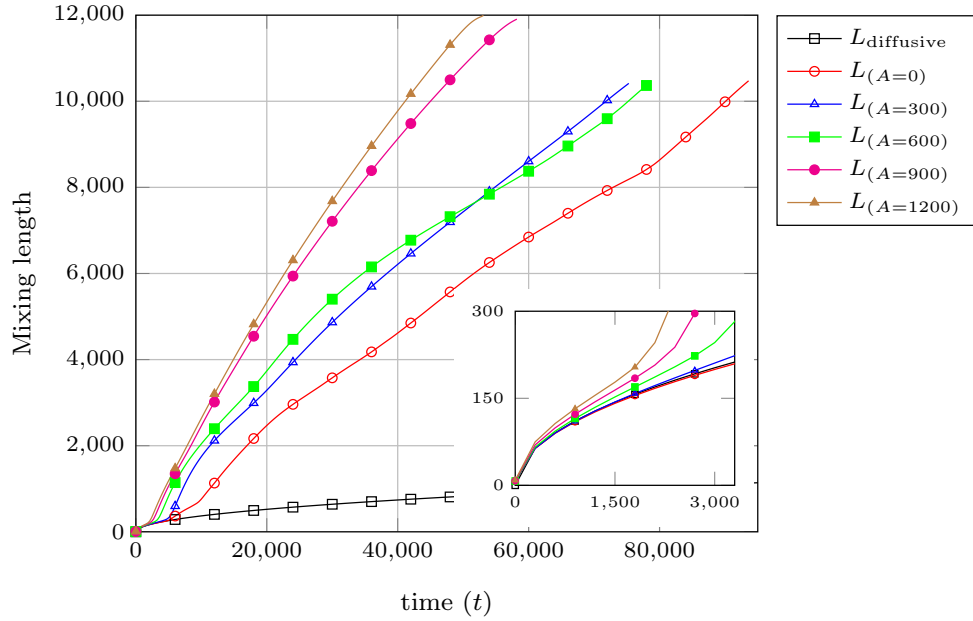
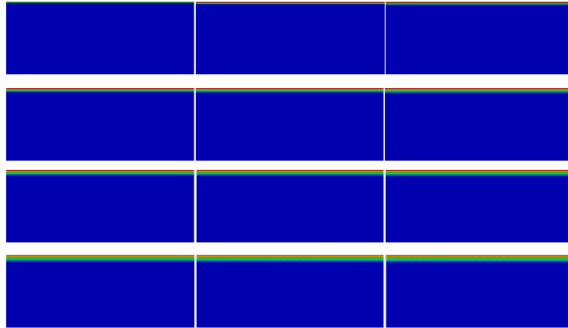
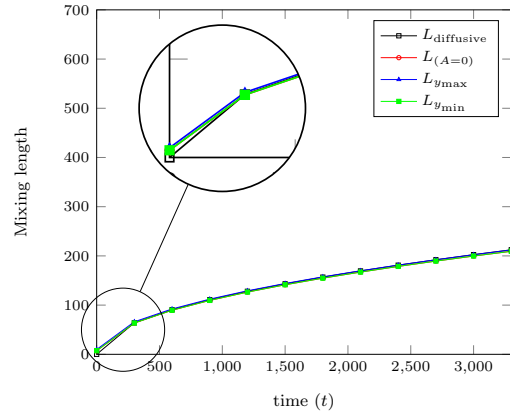


Figure 81: Mixing length as a function of time for plane surface and four values of the deformed interface. Each curve presents the average mixing length of nine runs, made with different initial conditions.

Figure 82 to Figure 84 show the beginning of the evolution in the diffusive regime (Figure 82(a)) to convective regime (Figure 83(a) and Figure 84(a)). Mixing lengths are evaluated at the x coordinate where the interface elevation is minimum and maximum, and concentration attains the value $c = 0.01$. The result is shown in Figure 82(b) to Figure 84(b). Clearly, the interface deformation enhances the convective process. Regarding the deformation, we can see an accumulation of the flow in the minimum point of deformation. Figure 83(b) and Figure 84(b) show that the mixing length tends to the analytic solution ($L_{\text{diffusive}}$ curve) at the minimum point ($L_{y_{\min}}$), moves away from the analytic curve after time $t = 500$ and is higher than mixing length (L) of simulation. In contrast to the flat interface, Figure 82(b), the regime is totally diffusive up to time $t = 3300$, while at the maximum point of deformation the mixing length is smaller than the analytic mixing length, namely, is smaller than the diffusive one.

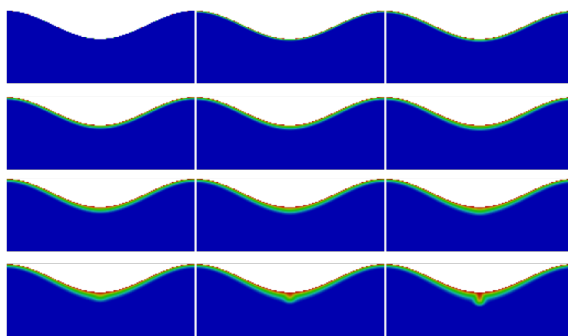


(a) Time evolution frames.

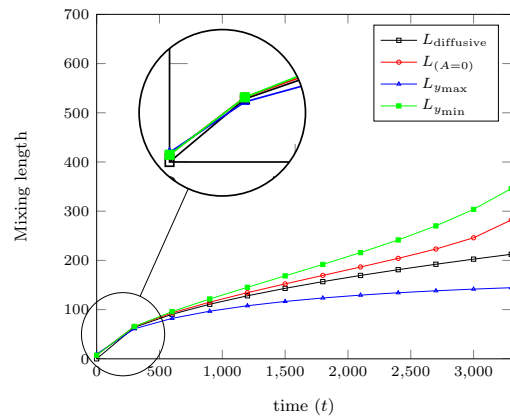


(b) Mixing length.

Figure 82: (a) Diffusive layer panel in the case with flat interface, from $t = 0$ to $t = 3300$ with $\Delta t = 300$. (b) Mixing length as a function of time.



(a) Time evolution frames.



(b) Mixing length.

Figure 83: (a) Diffusive layer panel in the case with deformed upper interface $A = 600$, from $t = 0$ to $t = 3300$ with $\Delta t = 300$. (b) Mixing length as a function of time.

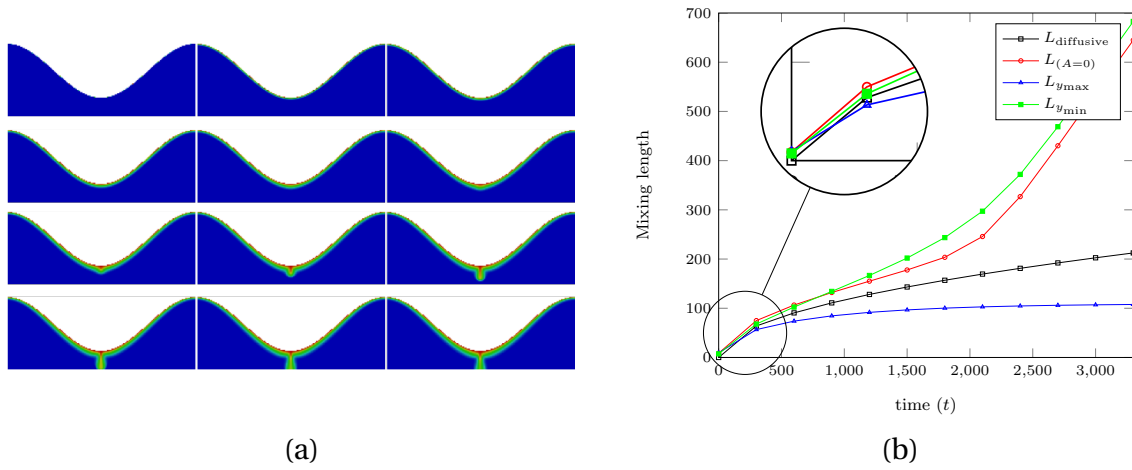


Figure 84: (a) Diffusive layer panel in the case with deformed upper interface $A = 1200$, from $t = 0$ to $t = 3300$ with $\Delta t = 300$. (b) Mixing length as a function of time.

Figure 85 presents a plot of the amount of dissolved CO_2 , as described in Chapter 3.5. The plots show that systems with deformed interface always present larger amounts of dissolved CO_2 , up to $t = 10,000$. However, deformed interfaces become progressively less efficient for larger times. For example, only interfaces with deformations up to $A = 600$ present amounts of dissolution larger than flat ones, for $t < 50,000$.

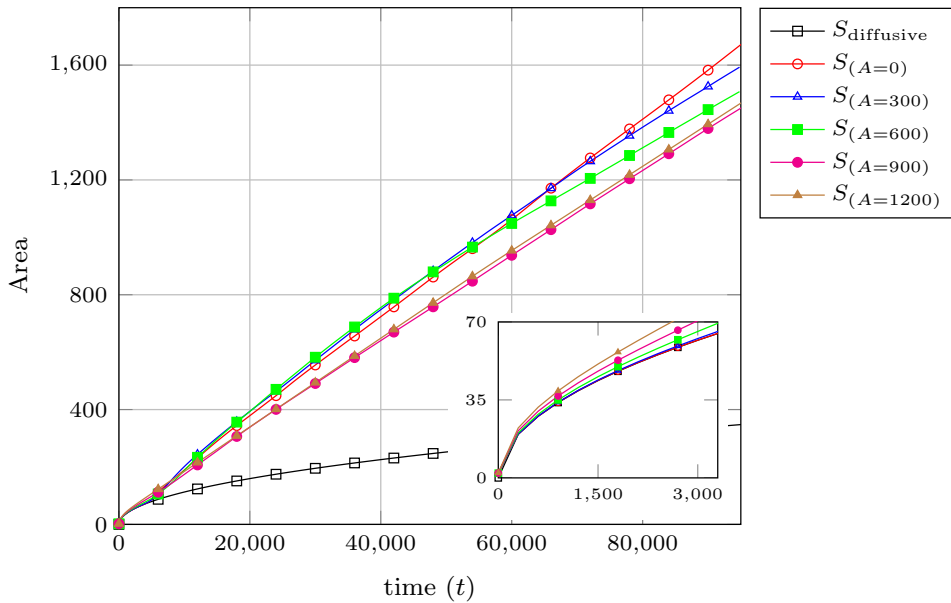


Figure 85: Area of the averaged transverse profile as a function of time for flat and four deformed interfaces. This area represents the total amount of dissolved CO_2 . Each curve presents the average of nine runs, made with different initial conditions.

The evolution dynamics can be evaluated by following the existing number of fingers.

Figure 71 to Figure 75 show that the interface deformation affects the amount of existing fingers. Figure 86 presents the system evolution for five amplitudes of deformation. Figure 86 presents the time evolution of the average number of fingers ($\langle n \rangle$). Initially, the flat interface presents the largest $\langle n \rangle$ up to $t = 40000$. After this time, the average number of fingers closely follows the average number developed in systems with deformed interface, with $A = 300$ and $A = 600$. For configurations with larger amplitudes, we observe that $\langle n \rangle$ decreases and tends to a constant value, as shown in the cases $A = 900$ and $A = 1200$, where $\langle n \rangle$ tends to 3 and 1, respectively. Particularly, in the case where $A = 1200$, the number of fingers is defined by the high forcing represented by the large deformation.

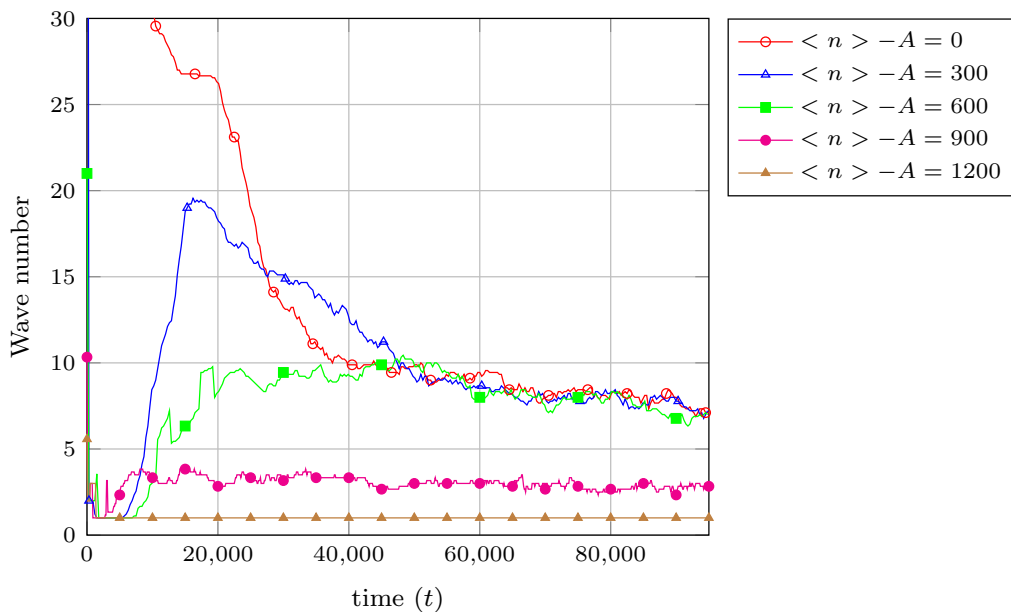


Figure 86: Averaged number of fingers as function of time for configurations with different interface deformations.

Figure 87 shows the relationship between amplitude of deformation and number of fingers at $t_0 = 4400$, where the convective regime already dominates. Though built with data extracted from an initial time of the evolution, this figure already captures the tendency of the system to develop structures with less fingers, as the amplitude of the interface increases, as identified in Figure 86.

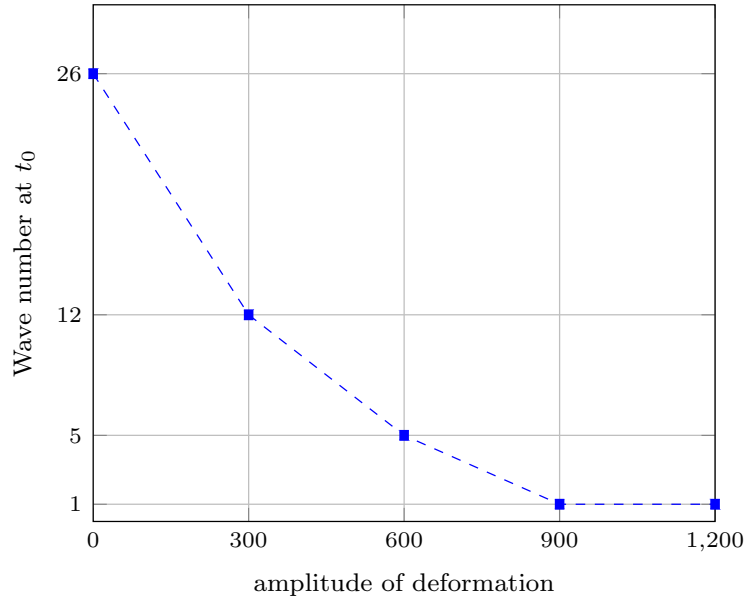


Figure 87: Relationship between average number of fingers and amplitude of deformation, at time $t_0 = 4400$. Each curve presents the average of nine runs, made with different initial conditions.

Figure 88 shows the sensitivity of the system evolution to changes in the initial condition. This figure presents nine space-time maps of the evolution for flat interface ($A = 0$) and four deformed interfaces ($A = 300$, $A = 600$, $A = 900$ and $A = 1200$). The space-time charts were evaluated at a distance $\Delta y'$ sufficiently small from the interface to capture the onset of the structure before interaction between fingers reduce the number of them. The maps present the solute concentration along the x direction, at a prescribed distance of the interface ($\Delta y' = 120$), as a function of time. Each map corresponds to a simulation run starting from a different initial condition, as identified in Figure 88.

Figure 88(a) shows that flat interfaces do not favor the onset of fingers in any particular point, what leads to more homogeneous distributions of fingers at early moments of the evolution. In these simulations we observe that fingers do not interact until the approximately same elapsed time, and start merging beyond this time. The large number of new fingers formed at the interface merge, but the system evolves to a structure with several ones, even for long times.

The case with $A = 600$ (Figure 88(c)) shows that a main finger first appears at the lowest point of the interface. Subsequently, new fingers appear in the neighbourhood of the lowest point of the interface. The new fingers merge with the main finger. The number of fingers surviving for long times is not so large as in the flat interface configuration, but, nevertheless,

more than one finger survives, as shown, for instance in runs # 3 and 7.

Figure 86 shows that larger interface deformations induce the onset of structures with a single finger. Figure 88(e) confirms the fact, and also shows that fingers initially formed along the interface rapidly merge with the main one.

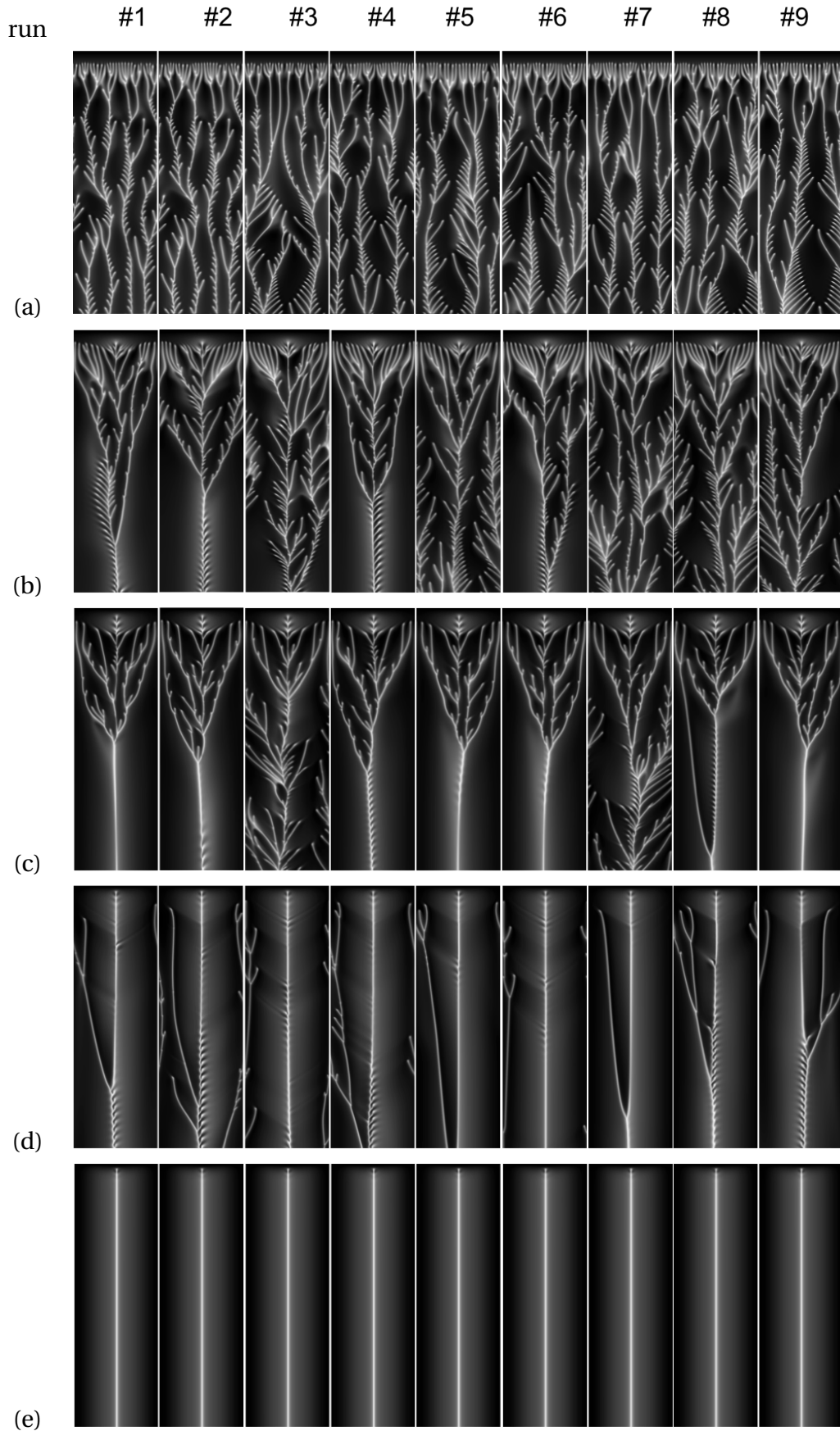


Figure 88: Space-time maps of the evolution for flat interface ($A = 0$) and for four deformed interfaces ($A = 300$, $A = 600$, $A = 900$ and $A = 1200$). The charts present the solute concentration along the x direction, at a prescribed distance of the interface ($\Delta y' = 120$), as a function of time. Each map corresponds to a simulation run starting from a different initial condition.

The dissolution flux, defined as the rate at which solute dissolves through of the upper boundary, provides an additional insight about the effect of the interface deformation on the amount of solute dissolved in the brine. Figure 89 shows the average flux along time, for the flat and deformed interfaces considered. This figure confirms the result given in Figure 85, where we can see that less deformed interfaces lead to larger amounts of solute captured by the brine.

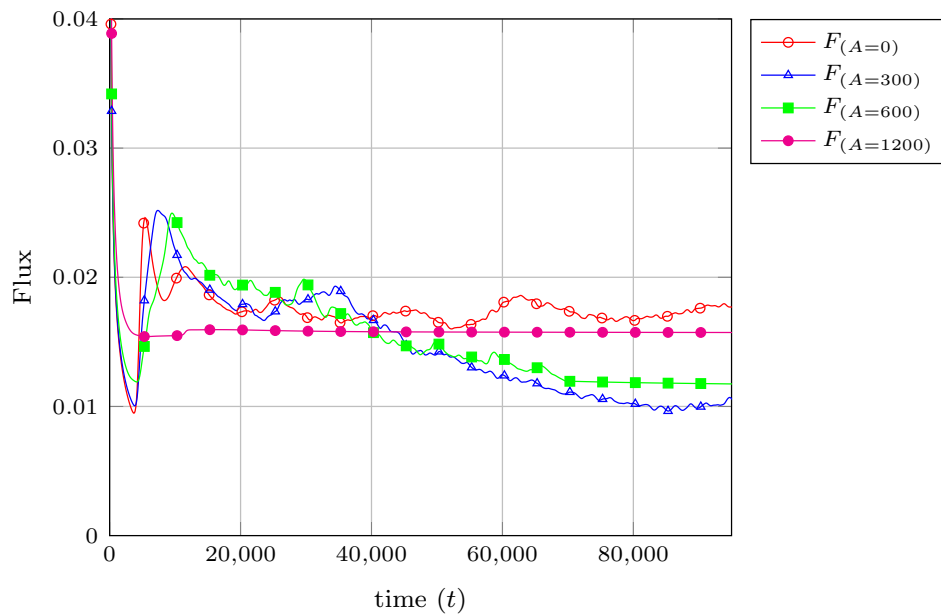


Figure 89: Time evolution of the average flux of CO_2 across the flat and deformed interface cases. Each curve presents the average of nine runs, made with different initial conditions.

CONCLUSIONS AND FUTURE WORKS

This work addresses a transient, two dimensional numerical study of the dissolution of carbon dioxide in the porous media found in saline aquifers. Dissolution of CO_2 in the brine leads to a gravitational instability, with denser layers at the upper part of the aquifer, inducing a convective mixing and the development of a structure of fingers. The system dynamics is assumed to obey Darcy's law, along with the Boussinesq approximation, to account for buoyancy effects introduced by concentration dependent densities.

A sinusoidal deformed interface between CO_2 and brine was assumed, with one wavelength along the domain length. This wavelength is much larger than the one of the fingers structure that emerges at the early moments of the evolution in the case of flat interfaces. Four different levels of deformation were assumed in our simulations. The results were compared with simulations performed in domains with flat interface.

We target the influence of the interface curvature on the rate of dissolution of CO_2 , and on the total amount of gas dissolved in the brine, in a prescribed time interval. The same time interval was adopted in all simulations, and this time was selected as the one at which a first finger reaches the domain bottom, in simulations with flat interface.

Our results show that the interface deformation induces the onset of a structure where the number of fingers decreases as the interface deformation increases. Fingers initially formed at interfaces with larger deformation rapidly merge with the surviving ones, accelerating the dissolution process at the beginning. At later times, the velocity of propagation of the finger tips is increased in case of deformed interface, as can be seen by the increase in the measure of the mixing length. However, since the number of fingers decreases with larger interface deformations, the total amount of gas dissolved in the brine decreases in these cases. For short times, the flux is generally reduced by the interfaces undulation but, for longer times, the difference in flux reduces for large interface deformations.

The velocity field is modeled by a vorticity-stream function formulation. The resulting equations are solved through the finite element method, with the material derivative of the concentration numerically represented by a Crank-Nicolson scheme.

Future works

For future works, we propose:

- Optimization and parallelization of the numerical code in *C* language.
- Investigate effects of the surface deformation and of the size of the periodic domain on the emerging structure of fingers.
- Address the problem of fingering in systems with deformable interfaces.
- Coupling the flow with reaction and dissolution of other chemical species.

REFERENCES

- [1] BACHU, S. CO₂ storage in geological media: Role, means, status and barriers to deployment. *Progress in Energy and Combustion Science*, v. 34, p. 254–273, 2008.
- [2] IPCC (Intergovernmental Panel on Climate Change), 2005. *Special Report on Carbon Dioxide Capture and Storage*. United Kingdom and New York, NY, USA, 2005.
- [3] ADEME. *La capture et le stockage géologique du CO₂*. [S.l.]: ADEME, 2005. (Les enjeux des Géosciences).
- [4] BACHU, S. Screening and ranking of sedimentary basins for sequestration of CO₂ in geological media in response to climate change. *Environmental Geology*, v. 44, p. 277–289, March 2003.
- [5] BRADSHAW, J. et al. CO₂ storage capacity estimation: Issues and development of standards. *International Journal of Greenhouse Gas Control*, p. 62–68, March 2007.
- [6] NEUFELD, J. A. et al. Convective dissolution of carbon dioxide in saline aquifers. *Geophysical Research Letters*, v. 37, n. L22404, November 2010.
- [7] HUPPERT, H. E.; NEUFELD, J. A. The fluid mechanics of carbon dioxide sequestration. *Annu. Rev. Fluid Mech.*, n. 46, p. 255–72, 2014.
- [8] SLIM, A. C. Solutal-convection regimes in a two-dimensional porous medium. *Journal of Fluid Mechanics*, v. 741, p. 461–491, 2014.
- [9] BACHU, S. Review of CO₂ storage efficiency in deep saline aquifers. *International Journal of Greenhouse Gas Control*, v. 40, p. 188–202, 2015.
- [10] EMAMI-MEYBODI, H. et al. Convective dissolution of CO₂ in saline aquifers: Progress in modeling and experiments. *International Journal of Greenhouse Gas Control*, v. 40, p. 238–266, 2015.
- [11] HOMSAY, G. Viscous fingering in porous media. *Annu. Rev. Fluid Mechanics*, v. 19, p. 271–311, 1987.

- [12] BACKHAUS, S.; TURITSYN, K.; ECKE, R. E. Convective instability and mass transport of diffusion layers in a hele-shaw geometry. *Physical Review Letters*, v. 106, 2011.
- [13] MOJTABA, S. et al. Experimental study of density-driven convection effects on CO₂ dissolution rate in formation water for geological storage. *Journal of Natural Gas Science and Engineering*, n. 21, p. 600–607, 2014.
- [14] BUDRONI, M. et al. Chemical control of hydrodynamics instabilities in partially miscible two-layer systems. *Journal Physical Chemistry Letters*, v. 5, p. 875–881, 2014.
- [15] IPCC (Intergovernmental Panel on Climate Change), 2013. *Summary for policymakers*. United Kingdom and New York, NY, USA, 2013.
- [16] IPCC (Intergovernmental Panel on Climate Change), 2001. *Climate Change 2001: The Scientific Basis*. United Kingdom and New York, NY, USA, 2001.
- [17] ORR Jr., F. M. Onshore geologic storage of CO₂. *Science*, v. 325, n. 5948, p. 1656–1658, 2009.
- [18] GHESMAT, K.; HASSANZADEH, H. The impact of geochemistry on convective mixing in a gravitationally unstable diffusive boundary layer in porous media: CO₂ storage in saline aquifers. *Journal of Fluid Mechanics*, v. 673, p. 480–512, 2011.
- [19] RIAZ, A. et al. Onset of convection in a gravitationally unstable diffusive boundary layer in porous media. *Journal of Fluid Mechanics*, v. 548, p. 87–111, 2006.
- [20] ENNIS-KING, J.; PATERSON, L. Coupling of geochemical reactions and convective mixing in the long-term geological storage of carbon dioxide. *International Journal of Greenhouse Gas Control*, v. 1, n. 1, p. 86–93, 2007.
- [21] MACMINN, C.; SZULCZEWSKI, M.; JUANES, R. CO₂ migration in saline aquifers. part 2. capillary trapping under slope and groundwater flow. *Journal of Fluid Mechanics*, v. 688, p. 321–351, 2011.
- [22] CHENG, P.; BESTEHORN, M.; FIROOZABADI, A. Effect of permeability anisotropy on buoyancy-driven flow for CO₂ sequestration in saline aquifers. *Water Resources Research*, v. 48, n. 9, 2012.

- [23] HIDALGO, J. J.; MACMINN, C. W.; JUANES, R. Dynamics of convective dissolution from a migrating current of carbon dioxide. *Advances in Water Resources*, v. 62, p. 511–519, 2013.
- [24] NEUFELD, J. A.; HUPPERT, H. E. Modelling carbon dioxide sequestration in layered strata. *Journal of Fluid Mechanics*, v. 625, p. 353–370, 2009.
- [25] PAU, G. et al. High-resolution simulation and characterization of density-driven flow in CO₂ storage in saline aquifers. *Advances in Water Resources*, v. 33, p. 443–455, 2010.
- [26] MACMINN, C.; SZULCZEWSKI, M.; JUANES, R. CO₂ migration in saline aquifers. part 1. capillary trapping under slope and groundwater flow. *Journal of Fluid Mechanics*, v. 662, p. 329–351, 2010.
- [27] HEWITT, D. R.; NEUFELD, J. A.; LISTER, J. R. Convective shutdown in a porous medium at high rayleigh number. *Journal of Fluid Mechanics*, v. 719, p. 551–586, January 2013.
- [28] TSAI, P. A.; RIESING, K.; STONE, H. A. Density-driven convection enhanced by an inclined boundary: Implications for geological CO₂ storage. *Physical Review E*, v. 87, 2013.
- [29] MACMINN, C. W. et al. Spreading and convective dissolution of carbon dioxide in vertically confined, horizontal aquifers. *Water Resources Research*, v. 48, 2012.
- [30] ENNIS-KING, J.; PRESTON, I.; PATERSON, L. Onset of convection in anisotropic porous media subject to a rapid change in boundary conditions. *Physics of Fluids*, v. 17, p. 084107–(1–15), 2005.
- [31] ENNIS-KING, J.; PATERSON, L. Role of convective mixing in the long-term storage of carbon dioxide in deep saline formations. *Society of Petroleum Engineers*, v. 10, n. 3, p. 8, September 2005.
- [32] XU, X.; CHEN, S.; ZHANG, D. Convective stability analysis of the long-term storage of carbon dioxide in deep saline aquifers. *Advances in Water Resources*, v. 29, p. 397–407, 2006.
- [33] LOODTS, V.; RONGY, L.; De WIT, A. Impact of pressure, salt concentration, and temperature on the convective dissolution of carbon dioxide in aqueous solutions. *Chaos*, v. 24, p. 043120–(1–12), 2014.

- [34] KNEAFSEY, T. J.; PRUESS, K. Laboratory experiments and numerical simulation studies of convectively enhanced carbon dioxide dissolution. *Energy Procedia*, v. 4, p. 5114–5121, 2011.
- [35] SLIM, A. C. et al. Dissolution-driven convection in a hele-shaw cell. *Physics of Fluids*, v. 25, p. 024101–1(1–20), 2013.
- [36] PONTES, J.; MANGIAVACCHI, N. *Fenômenos de transferência com aplicações às ciências físicas e à engenharia*. Rio de Janeiro: SBM, 2016.
- [37] FOX, R. W.; PRITCHARD, P. J.; MCDONALD, A. T. *Introduction to Fluid Mechanics*. 7. ed. [S.l.]: Wiley India Pvt. Limited, 2009.
- [38] ZENG, J.; YORTSOS, Y. C.; SALIN, D. On the brinkman correction in unidirectional hele-shaw flows. *Physics of Fluids*, n. 12, p. 3829–3836, 2003.
- [39] ALMARCHA, C. et al. Chemically driven hydrodynamic instabilities. *Physical Review Letters*, Physical Review Letters, n. 104, January 2010.
- [40] LOODTS, V.; RONGY, L.; WIT, A. D. Impact of pressure, salt concentration, and temperature on the convective dissolution of carbon dioxide in aqueous solutions. *CHAOS*, v. 24, p. 043120(1–12), October 2014.
- [41] ZIENKIEWICZ, O.; TAYLOR, R. *The Finite Element Method: The Basis*. 5th. ed. Oxford: ButterWorth-Heinemann, 2000.
- [42] HUGHES, T. J. R. *The Finite Element Method: Linear Static and Dynamic Finite Element Analysis*. 1. ed. New Jersey: Prentice-Hall, 1987.
- [43] FERZIGER, J. H.; PERIC, M. *Computational Methods for Fluid Dynamics*. 3rd. ed. Berlin and Heidelberg and New York and Barcelona and Hong Kong and London and Milan and Paris and Tokyo: Springer, 2002.
- [44] OFFICE OF ADVANCED SCIENTIFIC COMPUTING RESEARCH. *PETSc Users Manual*. Revision 3.7. [S.l.], April 2016.
- [45] De WIT, A. Miscible density fingering of chemical fronts in porous media: Nonlinear simulations. *Physics of Fluids*, v. 16, n. 1, p. 163–175, January 2004.

APPENDIX A - ANALYTICAL SOLUTIONS

We defined the mixing length and the area under the curve of the transverse concentration profile in Sec. 3.5 of Chapter 3. In purely diffusive regimes, i.e., in absence of any flow in vertical direction, an analytical solution exists. For the mixing length we have:

$$\langle c(y, t) \rangle = 1 - \text{erf}(z),$$

where $z = \frac{y}{2\sqrt{t}}$.

The transverse average concentration profile can be approximate by:

$$\langle c(y, t) \rangle = \frac{e^{-z^2}}{z\sqrt{\pi}},$$

for $z \gg 1$.

Let y_1 be such that $\langle c(y_1, t) \rangle = c_\varepsilon$. We choose $c_\varepsilon = 0.01$. Thus,

$$c_\varepsilon = \frac{e^{-z_1^2}}{z_1\sqrt{\pi}},$$

then

$$z_1 = 1.849 = \frac{y_1}{2\sqrt{t}},$$

so, we arrive to:

$$y_1 = 3.698\sqrt{t}.$$

For $y_0 = 0$ we have $\langle c(y_0, t) \rangle = 1$. The solution of mixing length in the diffusive regime is given by:

$$L = y_0 - y_1 = 3.698\sqrt{t}.$$

The area $S(t)$ under the curve of the transverse profile along the time is defined in

Eq.3.24, so we have:

$$\langle c(y, t) \rangle = 1 - \operatorname{erf}\left(\frac{y}{2\sqrt{t}}\right).$$

Integrating this equation:

$$S(t) = \int_0^{\infty} \left[1 - \operatorname{erf}\left(\frac{y}{2\sqrt{t}}\right) \right] dy,$$

with $z = \frac{y}{2\sqrt{t}}$, thus:

$$S(t) = 2\sqrt{t} \int_0^{\infty} [1 - \operatorname{erf}(z)] dz,$$

so:

$$S(t) = \frac{2}{\sqrt{\pi}} \sqrt{t}.$$

Therefore, the solution of area in the diffusive regime is given by:

$$S(t) = 1.128\sqrt{t}.$$

APPENDIX B - LINEAR STABILITY AND NONLINEAR SIMULATION ON INCLINED INTER-FACES

In this appendix we consider the linear stability of perturbations near an inclined interface, due to gravity effects. This problem can be used to explain the behaviour of instability in regions where the interface is deformed since, as a first approximation when the wavelength of the deformation is very long compared to the wavelength of the perturbation, the fact that the interface is deformed can be taken into account by its inclination with respect to the horizontal.

Posing the problem and governing equations

Similar to the horizontal case, we consider the problem of buoyancy-driven fingering generated in porous media by the dissolution of a fluid layer initially placed over a less dense one in which it is partially miscible. The interface is inclined by an angle θ relative to the vertical direction. The focus is on the lower layer only where the convective dissolution dynamics takes place.

A linear stability is performed, considering the Boussinesq approximation to account for buoyancy effects introduced by a concentration dependent density. The viscosity is assumed as constant. A vorticity-stream function formulation is adopted to solve the hydrodynamic field [39], [14].

We consider the incompressible flow in porous media following Darcy's Law, driven by density differences associated to the non dimensional concentration of a solute c , in a domain as shown in Fig. 1. The driving mechanism of the flow is the body force \mathbf{b} associated to gravity and the density of the fluid that, considering the Boussinesq approximation, is given by $\mathbf{b} = \mathbf{g}c$, where $\mathbf{g} = (-\cos\theta, \sin\theta)$ is the gravity vector (see Figure 90). Hence, the flow velocity $\mathbf{u} = (u, v)$ is given, in non dimensional form, by

$$\mathbf{u} = -\nabla p + \mathbf{g}c.$$

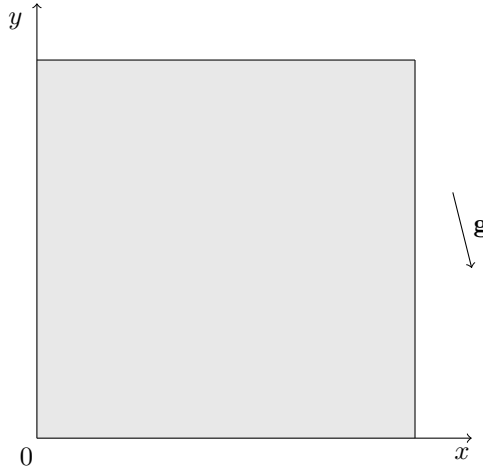


Figure 90: Sketch of domain with inclined surface, note that only gravity is schematically inclined.

Considering a two-dimensional flow, the vorticity $\omega = \nabla \times \mathbf{u}$, in general has nonzero component

$$\omega_z = \frac{\partial v}{\partial x} - \frac{\partial u}{\partial y} = \cos\theta \frac{\partial c}{\partial x} - \sin\theta \frac{\partial c}{\partial y}.$$

The nondimensional equations describing the dynamics in the flow field governing the evolution of the concentration field close to an inclined surface are:

$$\nabla^2 \psi = -\cos\theta \frac{\partial c}{\partial x} + \sin\theta \frac{\partial c}{\partial y} \quad (6.1)$$

$$\frac{Dc}{Dt} = \nabla^2 c, \quad (6.2)$$

where ψ is the stream function ($\mathbf{u} = (u, v) = (\partial\psi/\partial y, -\partial\psi/\partial x)$) and c is the concentration field. Equation 6.1 is the vorticity transport equation with Darcy's Law and Eq. 6.2 is the concentration transport equation.

Boundary conditions are analogous to the case of the flat and horizontal interface.

Base State

The base state of the problem is the time dependent solution of Eq. 6.2 of the concentration field, considering that the base state velocity has no component in the y direction, and

that the base profile is not a function of x , therefore canceling the advection nonlinear terms:

$$\bar{c}(y, t) = 1 - \operatorname{erf}\left(\frac{y}{2\sqrt{t}}\right). \quad (6.3)$$

Analogously, the x velocity component is given by:

$$\bar{u}(y, t) = \sin\theta \left(1 - \operatorname{erf}\left(\frac{y}{2\sqrt{t}}\right)\right). \quad (6.4)$$

Hence

$$\bar{u}(y, t) = \sin\theta \bar{c}(y, t). \quad (6.5)$$

Linear Stability Analysis (LSA) of the Base State

The LSA consists in adding perturbations to the base state solution characterized by the concentration profile (6.3) and

$$\begin{pmatrix} c \\ \psi \end{pmatrix} = \begin{pmatrix} \bar{c}(y, t) \\ \bar{\psi}(y, t) \end{pmatrix} + \begin{pmatrix} \tilde{c}(y) \\ \frac{i}{k}\tilde{\psi}(y) \end{pmatrix} \exp(\sigma t + ikx), \quad (6.6)$$

where $i^2 = -1$, k is the wavenumber of the perturbation and σ is the growth rate. The linearised evolution equations for the disturbances \tilde{c} and $\tilde{\psi}$ are thus:

$$\tilde{\psi}_{yy} - k^2\tilde{\psi} = -\cos\theta k^2\tilde{c} - i\sin\theta k\tilde{c}_y \quad (6.7)$$

$$\sigma\tilde{c} + \tilde{\psi}\tilde{c}_y + i\bar{u}k\tilde{c} = \tilde{c}_{yy} - k^2\tilde{c} \quad (6.8)$$

Boundary conditions for the concentration and stream function perturbations \tilde{c} and $\tilde{\psi}$ are thus:

$$\begin{aligned} y = 0: & \quad \tilde{c} = 0, \quad \tilde{\psi} = 0 \\ y \rightarrow \infty: & \quad \tilde{c} \rightarrow 0, \quad \tilde{\psi} \rightarrow 0. \end{aligned}$$

Upon defining $D^n = d^n/dy^n$, we rewrite Eq. 6.7:

$$(D^2 - k^2)\tilde{\psi} = -\cos\theta k^2\tilde{c} - i\sin\theta kD\tilde{c}, \quad (6.9)$$

and inversely:

$$\tilde{\psi} = -(D^2 - k^2)^{-1} (\cos \theta k^2 + i \sin \theta kD) \tilde{c}. \quad (6.10)$$

Likewise, Eq. 6.8 is rewritten as:

$$(D^2 - k^2) \tilde{c} - \tilde{\psi} D \tilde{c} - i \bar{u} k \tilde{c} = \sigma \tilde{c} \quad (6.11)$$

Upon replacing $\tilde{\psi}$ from Eq. 6.10 in Eq. 6.11 and rearranging terms we arrive at an eigenvalue-eigenfunction equation for the rate of growth σ and associated vertical concentration profile in the form:

$$\left[(D^2 - k^2) + D \tilde{c} (D^2 - k^2)^{-1} (\cos \theta k^2 + i \sin \theta kD) \tilde{c} - i k \bar{u} \right] \tilde{c} = \sigma \tilde{c}, \quad (6.12)$$

or, using Eq. 6.5

$$\left[(D^2 - k^2) + D \tilde{c} (D^2 - k^2)^{-1} (\cos \theta k^2 + i \sin \theta kD) - i \sin \theta k \bar{c} \right] \tilde{c} = \sigma \tilde{c}. \quad (6.13)$$

Equation 6.10 is an eigenvalue-eigenfunction problem to find pairs (σ, \tilde{c}) , for each value of θ , k and a given t , which defines \bar{c} . The most unstable mode correspond to the eigenfunction with the eigenvalue of greatest real part.

On the basis of Eqs. 6.1- 6.2, a LSA can be performed to obtain dispersion curves giving the growth rate of the perturbations as a function of the wavenumber.

Figure 91 and Figure 92 show the dispersion curves of normal mode perturbations of the base state, numerically obtained for several times, in the case of an horizontal interface ($\theta = 0$) compared to one inclined interface case ($\theta = \pi/16$). The real part of σ (Fig. Figure 91) shows the growth ($\sigma > 0$) or decay ($\sigma < 0$) rate of the perturbations. Results for $\theta = 0$ reproduce results found elsewhere. In this case, it can be seen that all perturbations are damped for $t < 55.59$. A first perturbation becomes marginally stable with a wavenumber $k = 0.06$, at $t = 55.59$. For the case of the inclined interface, all curves are displaced to the left and downwards, showing an increase in the stability of the flow, reducing the maximum growth rate and the maximum amplified wavenumber.

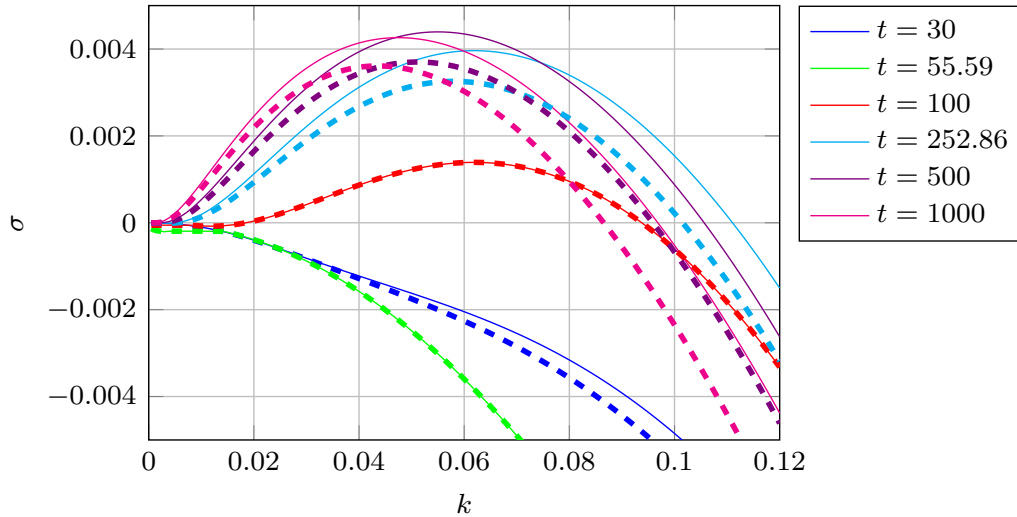


Figure 91: Dispersion curves (real part) of normal mode perturbations of the base state, numerically obtained for several times. Solid lines, $\theta = 0$, dashed lines, $\theta = \pi/16$. For $\theta = 0$, all perturbations are damped for $t < 55.59$, and a bifurcation occurs at $t = 55.59$ when the first perturbation becomes marginally stable with a wavenumber $k = 0.06192$. For $\theta = \pi/16$, all the curves are slightly displaced to the left and downwards.

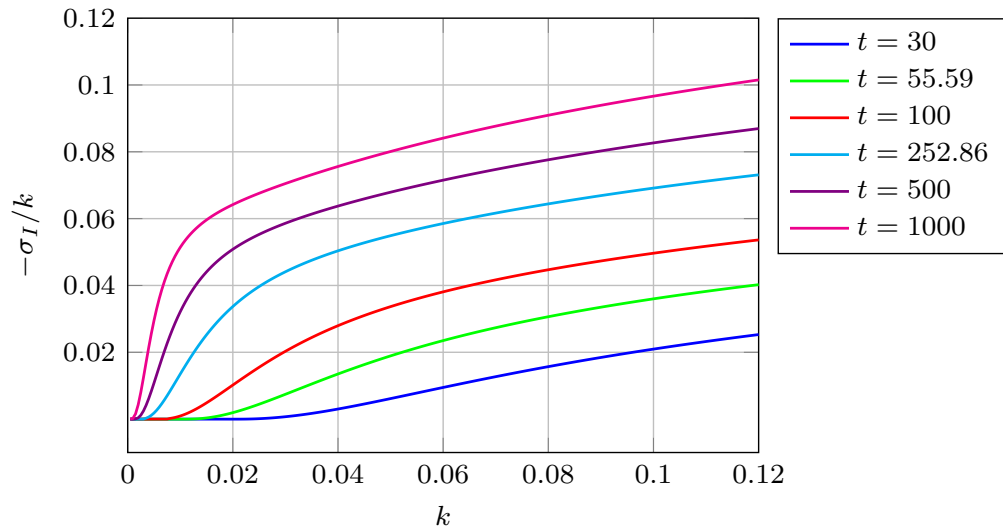


Figure 92: Dispersion curves (imaginary part) of normal mode perturbations of the base state, numerically obtained for several times. Solid lines, $\theta = 0$, dashed lines, $\theta = \pi/16$. All perturbations are stationary for $\theta = 0$. For $\theta = \pi/16$, the perturbation phase velocity increases with wavenumber k and with time t .

The dispersion curves for various angles of inclination and $t = 252.86$ are shown in Figure 93 and Figure 94. The effect of the inclination can be seen to be to gradually decrease the maximum amplification, the wavenumber of maximum amplification and the maximum amplified wavenumber as the inclination angle increases. For $\theta > 5\pi/16$, perturbations of all wavenumbers are attenuated. The main effect of the inclination can be seen on the *imaginary*

part of the eigenvalue, that gives rise to the drift velocity of the perturbations. In fact, for $\theta = 0$ the eigenvalue is real, and therefore there is no drift velocity. However, as θ departs from zero, σ_I and the drift velocity, $-\sigma_I/k$ increases.

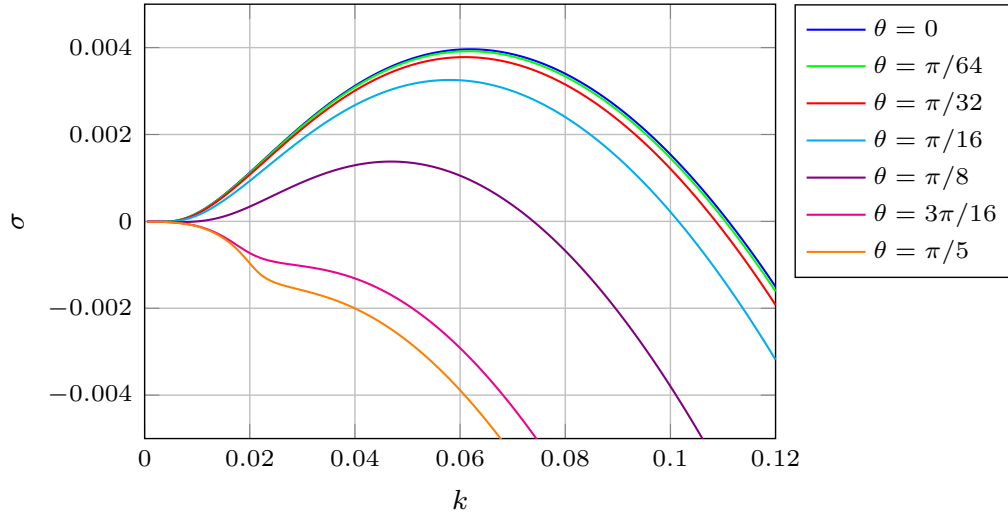


Figure 93: Dispersion curves (real part) of normal mode perturbations of the base state, numerically obtained for several inclination angles θ and $t = 252.86$.

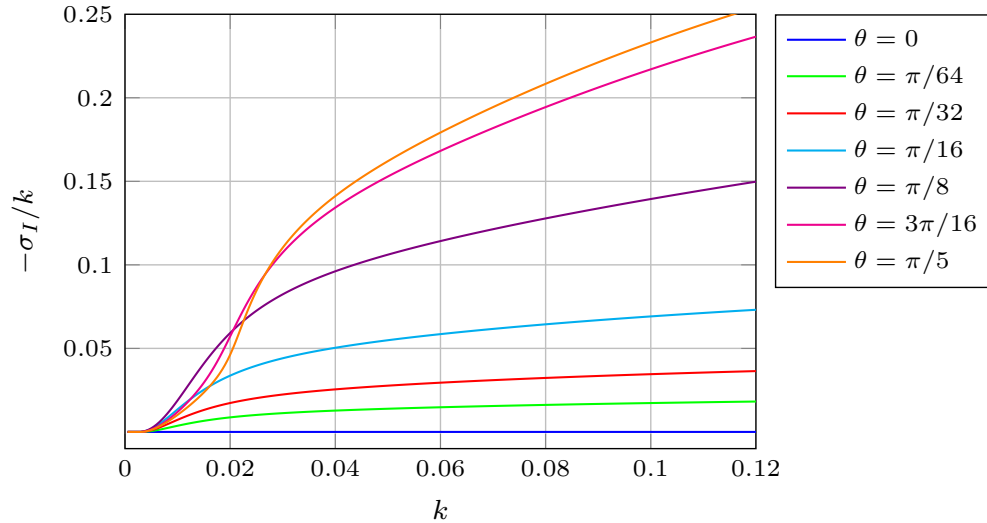


Figure 94: Dispersion curves (imaginary part) of normal mode perturbations of the base state, numerically obtained for several inclination angles θ and $t = 252.86$. The perturbations are stationary for $\theta = 0$. For $\theta > 0$, the perturbation phase velocity increases with wavenumber k and with wavenumber k .

Figure 95 and Figure 96 shows the results for large k . Figure 96 shows that the drift velocity approaches asymptotically the value 1, when divided by $\sin\theta$, with θ associated to each curve.

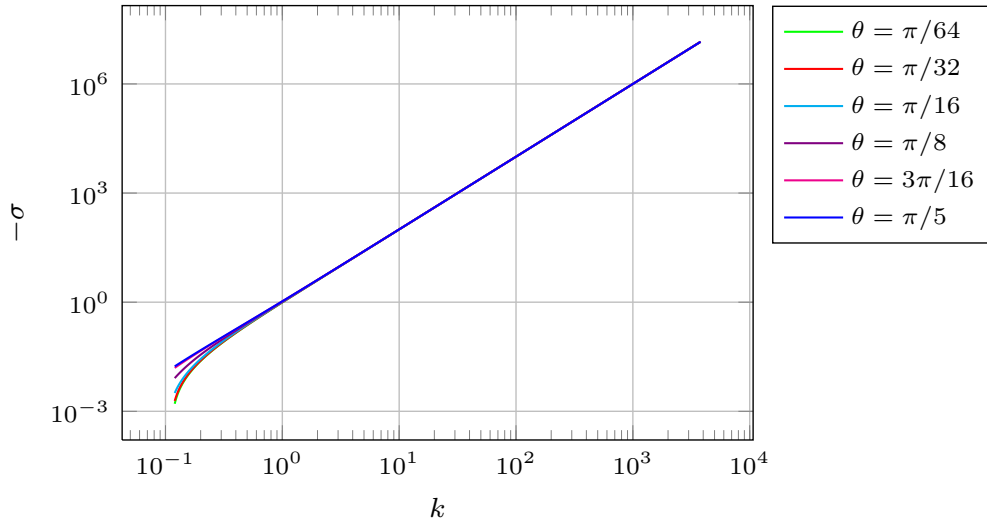


Figure 95: Dispersion curves (real part) of normal mode perturbations of the base state, numerically obtained for several inclination angles θ and $t = 252.86$, for large values of k .

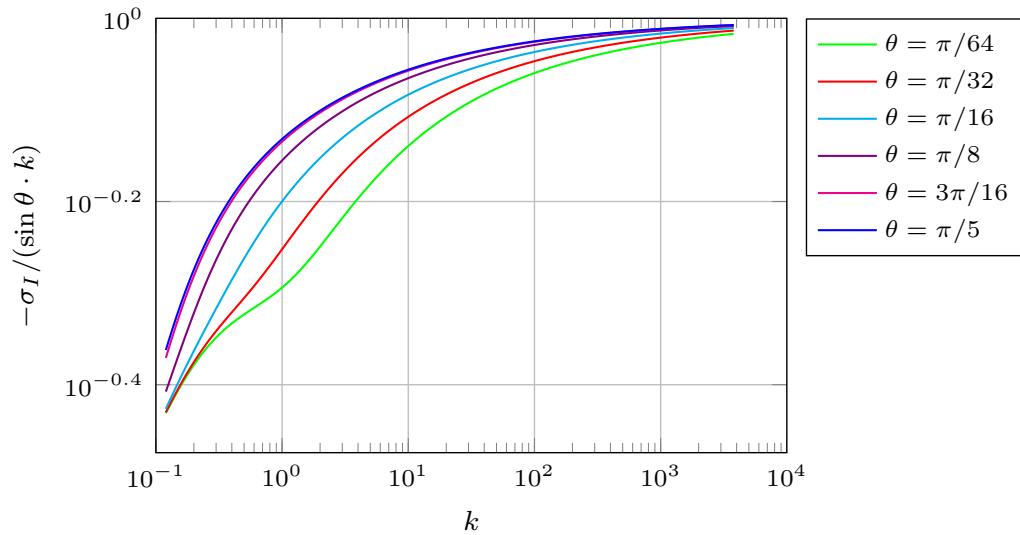


Figure 96: Dispersion curves (imaginary part) of normal mode perturbations of the base state, numerically obtained for several inclination angles θ and $t = 252.86$, for large values of k .

Numerical simulations of the complete non-linear equations show the time evolution of the fingers for larger times (see Figure 97 to Figure 100). Fingers develop similarly to the case with $\theta = 0$ however they tend to drift towards the right, as predicted by the LSA.

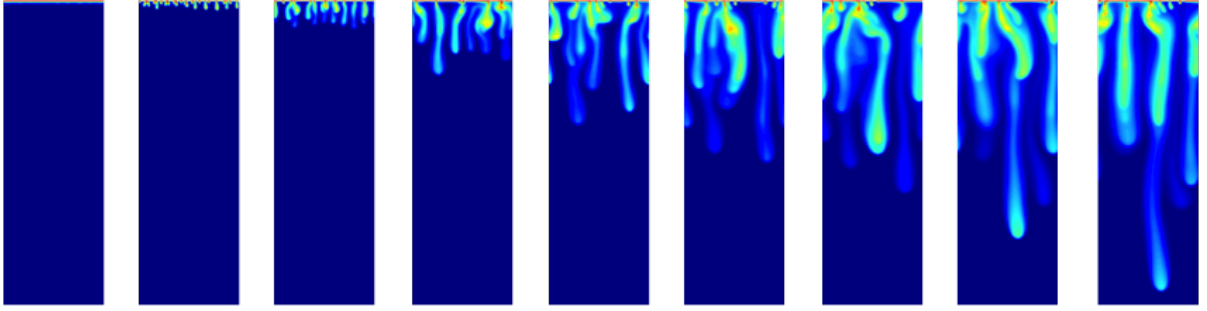


Figure 97: Time evolution of the case with $\theta = \pi/32$, in times: $t = 3000, 5000, 10000, 25000, 40000, 55000, 70000, 85000$ and 95000 .

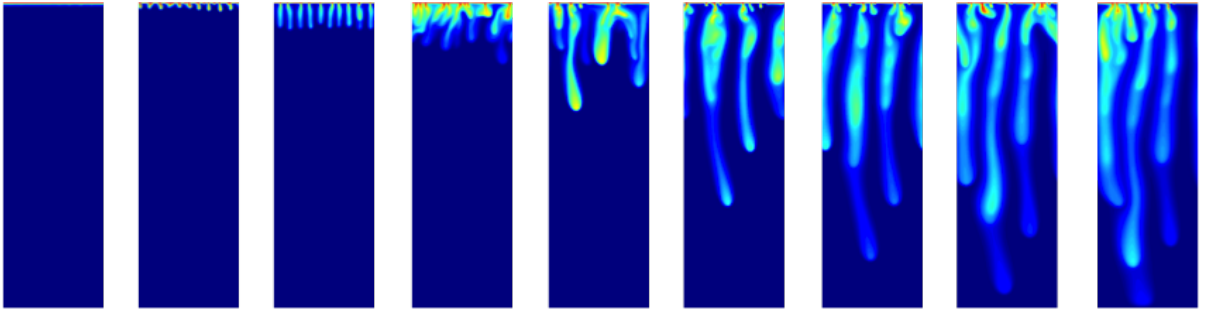


Figure 98: Time evolution of the case with $\theta = \pi/16$, in times: $t = 3000, 5000, 10000, 25000, 40000, 55000, 70000, 85000$ and 95000 .

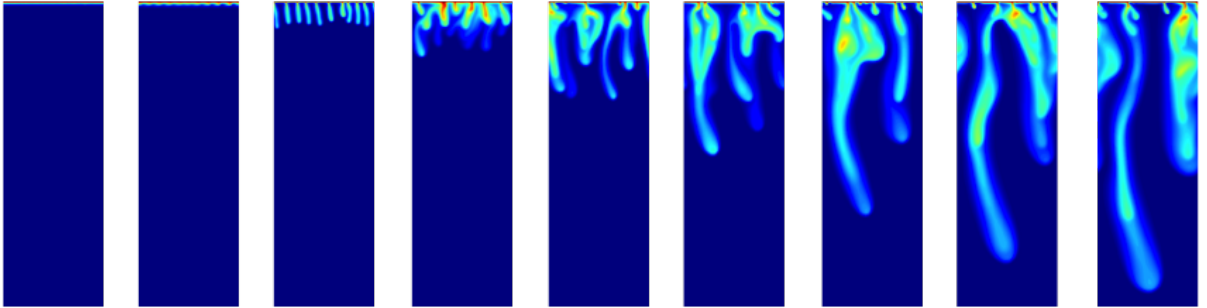


Figure 99: Time evolution of the case with $\theta = \pi/8$, in times: $t = 3000, 5000, 10000, 25000, 40000, 55000, 70000, 85000$ and 95000 .

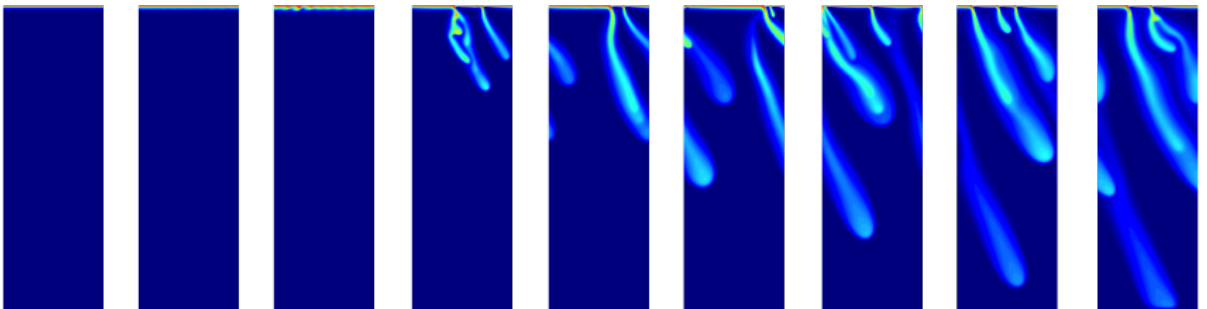


Figure 100: Time evolution of the case with $\theta = \pi/6$, in times: $t = 3000, 5000, 10000, 25000, 40000, 55000, 70000, 85000$ and 95000 .

The space-time maps Figure 101 and Figure 102 show that drift velocity increases as θ is increased, and the number of fingers decreases.

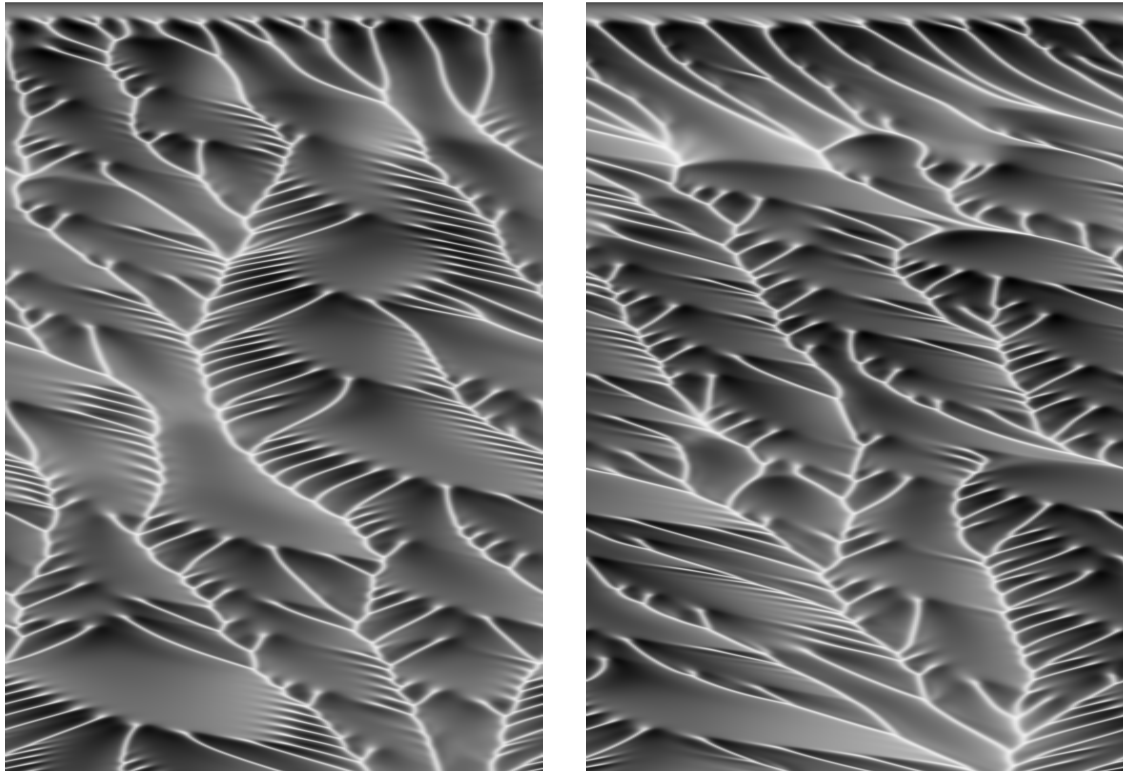


Figure 101: Left: space-time map with $\theta = \pi/32$ and right: space-time map with $\theta = \pi/16$.

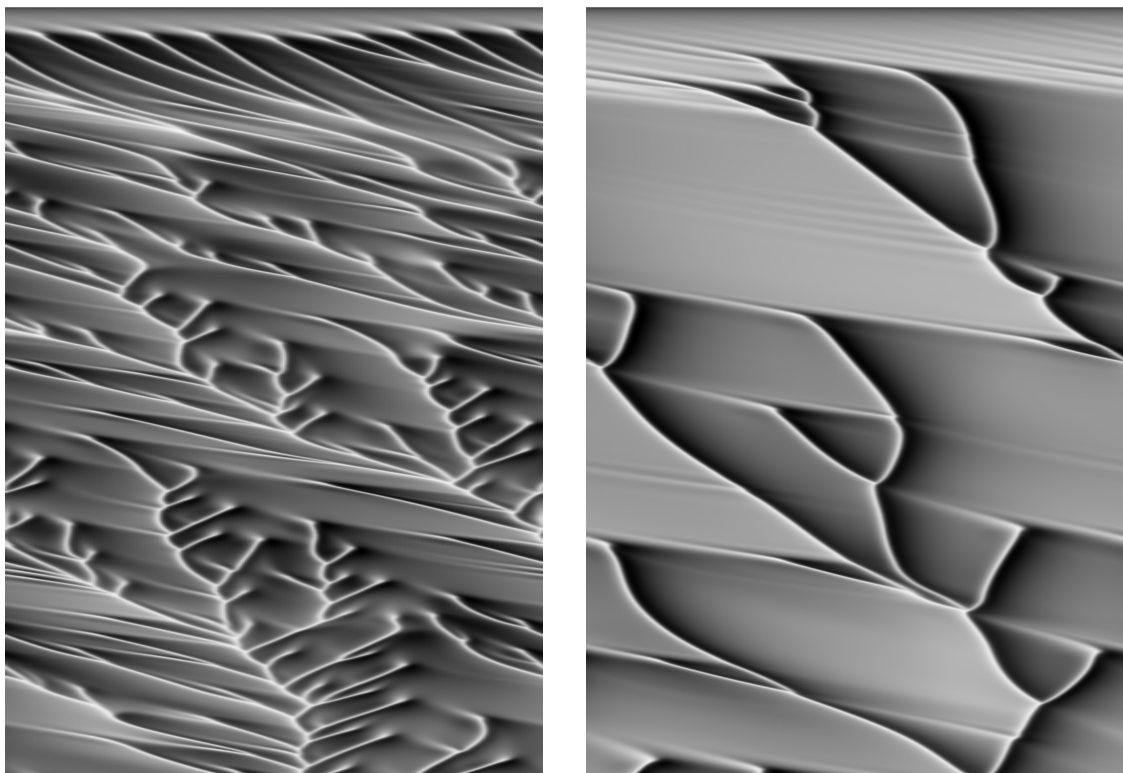


Figure 102: Left: space-time map with $\theta = \pi/8$ and right: space-time map with $\theta = \pi/6$.

APPENDIX C - CCIS 2016

This appendix we show the poster presented at 4th Conference of Computational Interdisciplinary Sciences (CCIS 2016), in this work was presented some results about density fingering. The 4th edition took place in November 2016, in the city of São José dos Campos - SP, Brazil.

Numerical simulations of CO₂ dissolution in a saline aquifers with deformed interface

Rachel Lucena^{1*}, Norberto Mangiacavchi¹, Anne De Wit², José Pontes¹ and Fabian Brau²

¹ State University of Rio de Janeiro

² Université libre de Bruxelles

rachel.lucena@gmail.com*

Abstract

We address the problem of buoyancy-driven fingering generated in porous media by the instability of a partially miscible fluid layer dissolving in a less dense fluid existing underneath. The fingering process induces an uneven distribution of dissolved CO₂ in the upper layers, which affects the surface tension distribution at the interface, and unstabilizes the geometry of the flat surface. We assume an undulated interface to model surface tension effects. The main purpose is to check if the curved surface increases the CO₂ dissolution rate and to evaluate an undulation amplitude that maximizes the gas dissolution. A 2D time dependent numerical simulation is performed, assuming that the flow is governed by Darcy's law, along with the Boussinesq approximation, to account for buoyancy effects introduced by concentration dependent densities. The velocity field is modeled by a vorticity-stream function formulation. The resulting equations are solved through the Taylor-Galerkin Finite Element Method, using a Crank-Nicolson time discretization.

Keywords: Porous Media, CO₂ storage, Fingering, Finite Element Method.

1. Introduction

Carbon dioxide (CO₂) capture and geological storage is an enabling technology proposed to mitigate consequences of the continued use of fossil fuels, well into this century[1]. The main relevance for the geological storage of CO₂ is reducing anthropogenic emissions into the atmosphere. Currently we know that the power and industry sectors combined dominate current global CO₂ emissions, accounting for about 60% of total CO₂ emissions[2][3]. Storage of carbon dioxide into deep saline aquifers has shown to be highly effective[4], [2], [5], [6], [7], [8]. When CO₂ is injected into the brine, the transport of the dissolved gas can occur by diffusion, advection, and convection, depending on the stage of sequestration process and geophysical properties of aquifer[9], [10]. The dissolution process results in a density gradient pointing upwards, that triggers a buoyancy-driven instability which, in turn, leads to a convective motion of the aquifer, and to the onset of a structure of fingers [11]. The present work leads to a better evaluation of the carbon dioxide dissolution rate in the brine and in a classification of the associated phenomena related to the development of a structure of fingers.

The onset of the fingering structure induces an uneven distribution of dissolved CO₂ in the upper layers of the aquifer, which affects the surface tension distribution at the interface, and unstabilizes the geometry of the flat surface. The emerging deformed interface affects the fingering process, and may enhance CO₂ sequestration. Nevertheless, most of the existing studies consider a flat interface, neglecting deformations resulting of the nonuniform distribution of the surface tension. The present study addresses the effect of the curvature of the CO₂/brine interface on the onset and development of a structure of fingers, and how is the rate of gas dissolution affected by the enhanced aquifer motion induced by the interface curvature. The main motivation is to check if the curved surface increases the dissolution rate and evaluate an undulation amplitude that maximizes CO₂ dissolution.

A 2D time dependent numerical simulation is performed, assuming that the flow is governed by Darcy's law, along with the Boussinesq approximation, to account for buoyancy effects introduced by concentration dependent densities. The velocity field is modeled by a vorticity-stream function formulation. The resulting equations are solved through the Taylor-Galerkin Finite Element Method, using a Crank-Nicolson time discretization.

2. Governing Equations

The equations describing the dynamics in the flow field are:

$$\nabla^2 \psi = \frac{\partial c}{\partial x} \quad (1)$$

$$\frac{Dc}{Dt} = \nabla^2 c, \quad (2)$$

where: ψ is the stream function ($u = (\partial\psi/\partial y, -\partial\psi/\partial x)$) and c is the concentration field. Equation 1 is the vorticity transport equation with Darcy's Law and Eq. 2 is the concentration transport equation.

Boundary conditions for the velocity field are prescribed as slip, i.e., zero normal component (v) of velocity at the upper, and lower walls and periodic at the sidewalls. For the dimensionless concentration field, we prescribe boundary conditions no flux at the lower wall, periodic boundary conditions at the sidewalls and at the top we set a constant value equal to 1.

3. Numerical results

Numerical integration of the governing equations (Eqs. 1 and 2) were performed over a domain $L_x = 4000$, $L_y = 12000 + A$, where A is the amplitude of the interface deformation.

A numerical mesh containing $n_{el} = 2(n_x - 1)(n_y - 1) = 3,840,000$ triangular elements was adopted, with $n_x = 801$ and $n_y = 2401$, where n_x and n_y are, respectively, the number of points along the x and y directions. The time step adopted to advance time was $\Delta t = 2.5$. The same time interval was adopted in all simulations, and this time was selected as the one at which a first finger reaches the domain bottom, in simulations with flat interface. Simulations were performed in domains with flat and four deformed interfaces, $A = 0, 300, 600, 900$ and 1200 . Each curve, in Figures 2, 3, 4 and 5, presents the average of nine runs, made with different initial conditions.

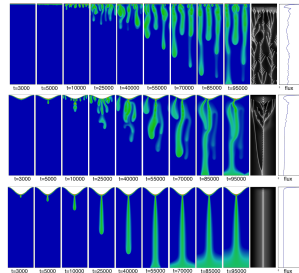


Figure 1: An overview of the simulations, with three different maximum heights A ($A = 0, 600, 1200$, respectively), of the deformed gas/brine interface. Each line presents an evolution of the fingering structure, the associated space-time chart evaluated at a distance $\Delta y = 120$ of the flat interface and the dissolution flux at the interface.

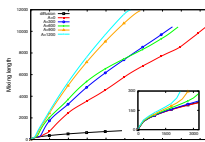


Figure 2: Mixing length as a function of time for plane surface and four values of the deformed interface.

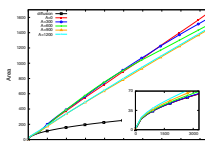


Figure 3: Area of the averaged transverse profile as a function of time for flat and four deformed interfaces. This area represents the total amount of dissolved CO₂.

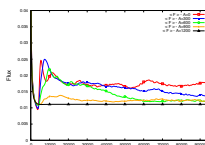


Figure 4: Time evolution of the average flux of CO₂ across the flat and deformed interface cases.

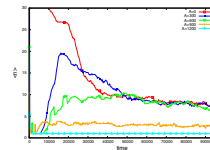


Figure 5: Averaged number of fingers as function of time for configurations with different interface deformations.

4. Conclusions

Our results show that the interface deformation induces the onset of a structure where the number of fingers decreases as the interface deformation increases. Fingers initially formed at interfaces with larger deformation rapidly merge with the surviving ones, accelerating the dissolution process at the beginning. However, since the number of fingers decreases with larger interface deformations, the total amount of gas dissolved in the brine decreases in these cases.

5. Acknowledgments

The authors R.L., N.M. and J.P. acknowledge the financial support from the Brazilian agencies FAPERJ, CAPES and CNPq, A.D. and F.B. acknowledgment financial support from FNRS Forecast programme.

References

- [1] S. Bachu, "Co2 storage in geological media: Role, means, status and barriers to deployment," *Progress in Energy and Combustion Science*, vol. 34, pp. 254–273, 2008.
- [2] IPCC, "Special report on carbon dioxide capture and storage," tech. rep., Prepared by Working Group III of the Intergovernmental Panel on Climate Change, United Kingdom and New York, NY, USA, 2005.
- [3] *La capture et le stockage géologique du CO2. Les enjeux des Géosciences*, ADEME, 2005.
- [4] S. Bachu, "Screening and ranking of sedimentary basins for sequestration of CO₂ in geological media in response to climate change," *Environmental Geology*, vol. 44, pp. 277–289, March 2003.
- [5] J. Bradshaw, S. Bachu, D. Borjesson, R. Burruss, S. Holloway, N. P. Christensen, and O. M. Mathiassen, "CO₂ storage capacity estimation: Issues and development of standards," *International Journal of Greenhouse Gas Control*, pp. 62–68, March 2007.
- [6] J. A. Neufeld, M. A. Hesse, A. Riaz, M. A. Hallworth, H. A. Tchelepi, and H. E. Huppert, "Convective dissolution of carbon dioxide in saline aquifers," *Geophysical Research Letters*, vol. 37, November 2010.
- [7] H. E. Huppert and J. A. Neufeld, "The fluid mechanics of carbon dioxide sequestration," *Annu. Rev. Fluid Mech.*, no. 46, pp. 255–72, 2014.
- [8] A. C. Slim, "Solutal-convection regimes in a two-dimensional porous medium," *J. Fluid Mech.*, vol. 741, pp. 461–491, 2014.
- [9] S. Bachu, "Review of CO₂ storage efficiency in deep saline aquifers," *International Journal of Greenhouse Gas Control*, vol. 40, pp. 188–202, 2015.
- [10] H. Emami-Meybodi, H. Hassanzadeh, C. P. Green, and J. Ennis-King, "Convective dissolution of CO₂ in saline aquifers: Progress in modeling and experiments," *International Journal of Greenhouse Gas Control*, vol. 40, pp. 238–266, 2015.
- [11] G. Homsy, "Viscous fingering in porous media," *Annu. Rev. Fluid Mechanics*, vol. 19, pp. 271–311, 1987.

APPENDIX D - CCIS 2014

In this appendix we show the work presented at 3rd Conference of Computational Interdisciplinary Sciences (CCIS 2014), this work was presented the beginning of the study of linear stability analysis for the flat interface. The 3rd edition took place in October 2014, in the city of Asunción, Paraguay.

Finite Element Simulation of Fingering in Convective Dissolution in Porous Media

Rachel M. Lucena^{a1}, Norberto Mangiavacchi ^a, José Pontes^a,
Anne De Wit ^b, and Gustavo Anjos ^a

^aGroup of Environmental Studies for Water Reservoirs - GESAR, State
University of Rio de Janeiro, Rio de Janeiro, RJ, Brazil

^bNonlinear Physical Chemistry Unit, CP 231, Faculté des Sciences, Université
Libre de Bruxelles (ULB), Brussels, Belgium.

Abstract

We address the problem of buoyancy-driven fingering generated in porous media by the instability of a partially miscible fluid layer dissolving in another denser fluid placed below it. A 2D time dependent numerical simulation is performed, assuming that the flow is governed by Darcy's law, along with the Boussinesq approximation to account for buoyancy effects introduced by concentration dependent densities. The velocity field is modeled by a vorticity-stream function formulation. The resulting equations are solved through the finite element method, with the material derivative of the concentrations numerically represented by a Semi-Lagrangian Scheme.

Keywords: fingering, instability, finite element method.

1. FINITE ELEMENT METHOD

Fingering refers to hydrodynamic instabilities of deforming interfaces into fingers during the displacement of fluids in porous media. These instabilities are closely linked to changes in viscosity or density between the different layers or within a single phase containing a solute invariable concentration that affects the fluid density or viscosity[1].

Fingering occurs in a variety of applications, including CO_2 sequestration techniques, secondary and tertiary crude oil recovery, fixed bed regeneration chemical processing, hydrology, filtration, liquid chromatography, and medical applications, among others. In fact, the phenomena are expected to occur

¹E-mail Corresponding Author: rachel.lucena@uerj.br

in different fields of science and technology, in which flows in porous media are present.

We consider the problem of buoyancy-driven fingering generated in porous media by the dissolution of a fluid layer initially placed over a less dense one in which it is partially miscible. The focus is on the lower layer only where the convective dissolution dynamics takes place.

A 2D time dependent numerical simulation is performed, assuming that the flow is governed by Darcy's law, along with the Boussinesq approximation to account for buoyancy effects introduced by a concentration dependent density. The viscosity is assumed as constant. A vorticity-stream function formulation is adopted to solve the hydrodynamic field [2, 3]. The resulting equations are solved through the finite element method, with the material derivative of the concentrations numerically represented by a semi-lagrangian scheme[4].

Boundary conditions for the velocity field are prescribed as no slip at the upper and lower walls and periodic at the sidewalls. For the dimensionless concentration field, we prescribe as boundary conditions no flux at the lower wall, periodic boundary conditions at the sidewalls and at the top we set a constant value equal to 1. The upper boundary is assumed as flat and horizontal. The onset of fingering is induced by the numerical grid.

Darcy's law and the advective-diffusion equation of the transport of the relevant chemical species are solved in the weak form (also called variational form). The variational form of the governing equations are obtained by properly weighting the equations with weighting functions. The global system, with discrete representation of the derivatives and written in matrix form reads:

$$\begin{aligned} \mathbf{K}\psi + \mathbf{M}\omega &= 0 \\ \mathbf{M}\omega &= R\mathbf{D}_x c \\ (\mathbf{M} + \Delta t\mathbf{K}) c^{n+1} - \mathbf{M}c_d^n &= 0. \end{aligned} \tag{1}$$

where Eq. 1 are the stream function, vorticity equation (Darcy's Law) and concentration transport equation, respectively, \mathbf{K} is the stiffness matrix, \mathbf{M} is the mass matrix, \mathbf{D}_x is the gradient matrix, c_d is the concentration at the departure points of the lagrangian trajectories.

The system of equations is solved in two steps. In the first one we obtain the stream function and vorticity. Velocity components are then obtained and introduced in the transport equation of c , which is subsequently solved.

An incomplete LU pre-conditioner is applied to the matrices and the linear systems are then solved with the use of GMRES (Generalized Minimal Residual) solver. Preconditioned conjugate gradients methods were also used to obtain the velocity field from the stream function solutions.

2. NUMERICAL RESULTS

Figure 1(a) shows average concentration profiles c for different times, where the dashed curves refer to the analytical solution related to the numerical profile shown by the continuous curve of the same color. We can observe that for $t = 4000$ a sharp distortion due to the perturbation growth, can be observed in the nonlinear evolution regime of c (see Fig. 1(e)). Fig. 1(b) shows the amplitude of perturbation modes of concentration and stream function obtained from the solution of the governing equations using Fourier analysis, at $t = 3000$.

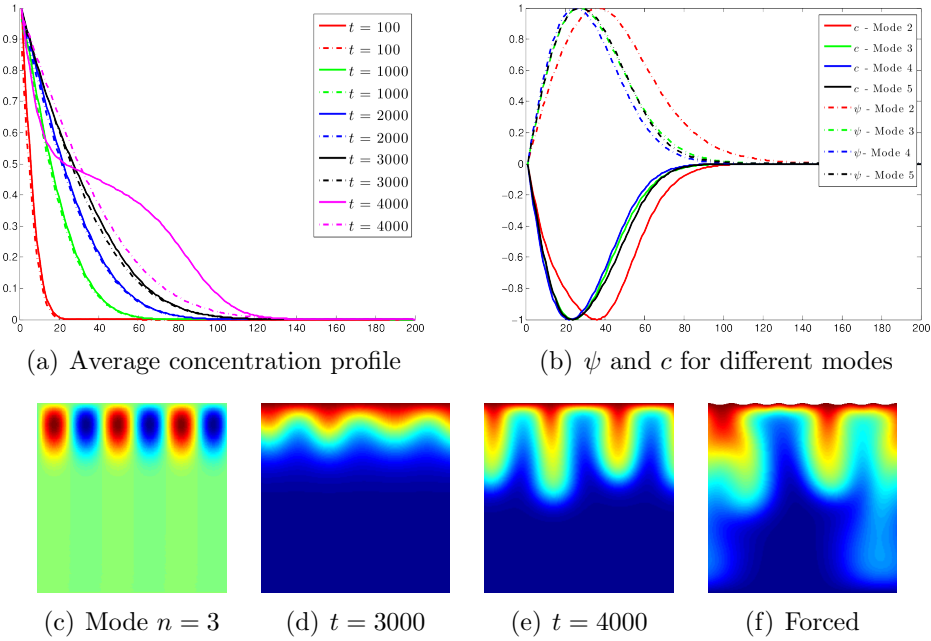


Figure 1 - Numerical results.

3. CONCLUSIONS

Solutions obtained up to now are in accordance with those found in the literature [5]. The evolution strongly depends on the initial condition. We are currently investigating the nonlinear evolution of instabilities developed with either a flat upper surface or forced by a deformed upper surface (Figs. 1(e) and 1(f)).

ACKNOWLEDGMENTS: The authors R.L., N.M., J.P. and G.A. acknowledge financial support from the Brazilian agencies FAPERJ, CAPES and CNPq. A.D. acknowledges financial support from FNRS Forecast programme.

References

- [1] HOMSY, GM, 1987. Viscous fingering in porous media, *Annu. Rev. Fluid Mech.* 19: 271-311.
- [2] ALMARCHA, C, TREVELYAN, PMJ, GROSFILS, P, DE WIT, A, 2010. Chemically driven hydrodynamics instabilities, *Physical Review Letters*, 104: 044501-(1-4).
- [3] BUDRONI, MA, RIOLFO, LA, LEMAIGRE, L, ROSSI, F, RUSTICI, M, DE WIT, A, 2014. Chemical control of hydrodynamic instabilities in partially miscible two-layer systems. *Journal Physical Chemistry Letters* 5: 875-881.
- [4] ANJOS, G, MANGIACACCHI, N, CARVALHO, LM, PONTES, J, SOARES, CBP, 2007. Aproximaç o Semi-lagrangeana para as Equa es de Navier-Stokes acopladas ao transporte de esp cie qu mica, *XXX CN-MAC*, 672.
- [5] LOODTS, V, RONGY, L, DE WIT, A, 2014. Convective dissolution of carbon dioxide in salted water: linear stability analysis and effect of control parameters, *Chaos*, in press.